LBL-38281
UC-411

Center for Advanced Materials

CAM

Thin Films of Metal Oxides on Metal Single Crystals: Structure and Growth by Scanning Tunneling Microscopy

H.C. Galloway
(Ph.D. Thesis)

December 1995

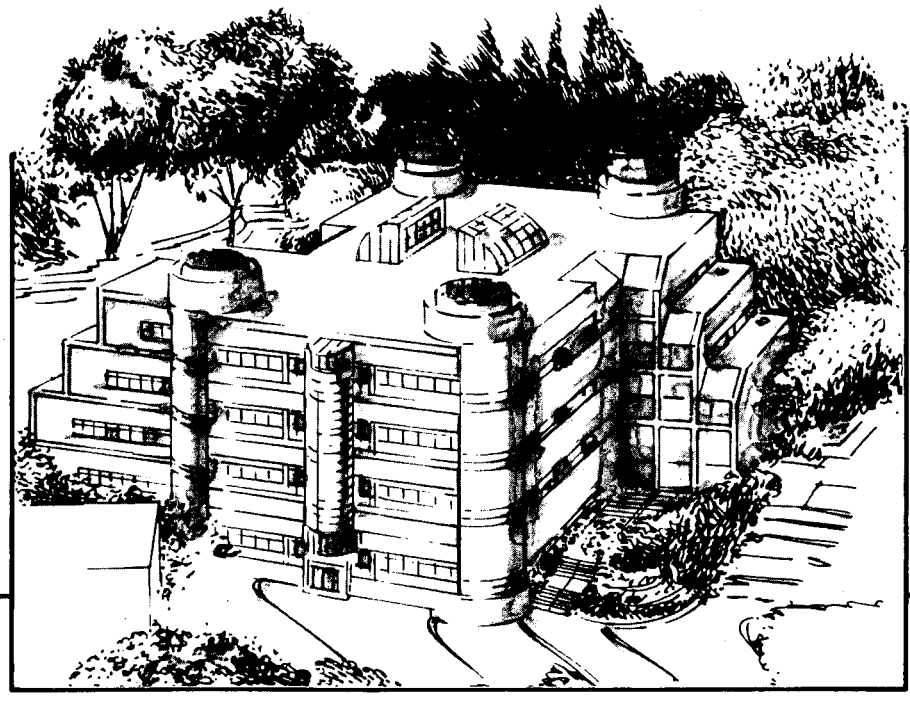

Materials and Chemical Sciences Division

Lawrence Berkeley Laboratory • University of California

ONE CYCLOTRON ROAD, BERKELEY, CA 94720 • (415) 486-4755

Prepared for the U.S. Department of Energy under Contract DE-AC03-76SF00098

DISCLAIMER

LBL-38281
UC 411

Thin Films of Metal Oxides on Metal Single Crystals: Structure and Growth by Scanning Tunneling Microscopy

Heather Claire Galloway
Ph.D. Thesis

Department of Physics
University of California

and

Materials Sciences Division
Lawrence Berkeley National Laboratory
University of California
Berkeley, California 94720

December 1995

This work was supported by the Director, Office of Energy Research, Office of Basic Energy Sciences, Materials Science Division, of the U.S. Department of Energy under Contract No. DE-AC03-76SF00098.

Thin Films of Metal Oxides on Metal Single Crystals: Structure and Growth by Scanning Tunneling Microscopy

by

Heather Claire Galloway

B.S. (University of Texas at Austin) 1988
M.A. (University of California at Berkeley) 1990

A dissertation submitted in partial satisfaction of the
requirements for the degree of
Doctor of Philosophy

in

Physics

in the

GRADUATE DIVISION

of the

UNIVERSITY of CALIFORNIA at BERKELEY

Committee in charge:

Professor Yuen-Ron Shen, Chair
Dr. Miquel Salmeron, Co-chair
Professor Roya Maboudian
Professor Zi Qiang Qiu

1995

Thin Films of Metal Oxides on Metal Single Crystals: Structure and Growth by Scanning Tunneling Microscopy

by

Heather Claire Galloway

Abstract

Thin Films of Metal Oxides on Metal Single Crystals:
Structure and Growth by Scanning Tunneling Microscopy

by

Heather Claire Galloway

Doctor of Philosophy in Physics

University of California at Berkeley

Professor Yuen-Ron Shen, Chair
Dr. Miquel B. Salmeron, Co-chair

Detailed studies of the growth and structure of thin films of metal oxides grown on metal single crystal surfaces using Scanning Tunneling Microscopy (STM) are presented. The oxide overlayer systems studied are iron oxide and titanium oxide on the Pt(111) surface. The complexity of the metal oxides and large lattice mismatches often lead to surface structures with large unit cells. These are particularly suited to a local real space technique such as scanning tunneling microscopy. In particular, the symmetry that is directly observed with the STM elucidates the relationship of the oxide overlayers to the substrate as well as distinguishing the structures of different oxides.

For the iron oxide system the first monolayer grows as FeO(111) with a lateral lattice constant of 3.09 ± 0.02 Å as compared to the bulk value of 3.04 Å. The surface is oxygen terminated with a strongly contracted FeO bond distance of 1.90 Å as compared to the bulk value of 2.15 Å. At higher coverages $Fe_3O_4(111)$ and α-$Fe_2O_3(0001)$ structures can be identified by their symmetry with respect to the FeO monolayer. The $Fe_3O_4(111)$ has a simple 2x2 unit cell and the α-$Fe_2O_3(0001)$ is $\sqrt{3}x\sqrt{3}R30°$. The FeO(111) exhibits a large three fold symmetric unit cell (26 Å) due to the lattice mismatch with the Pt(111) surface and the α-$Fe_2O_3(0001)$ has an even larger unit cell (43 Å) due to the lattice mismatch with the FeO monolayer. The large unit cells are imaged as Moiré

patterns (modulations in the average current and atomic corrugation) in the STM images. For titanium oxide the first monolayer grows as $Ti_2O_3(0001)$ under reducing conditions and $TiO_2(111)$ structures are formed at higher oxygen pressures and higher coverages. Both ordered structures also exhibit Moiré pattern images in the STM experiments.

A second goal of these studies is to advance the understanding of the tunneling process in metal oxides and to better determine the relationship between the experimental STM results and the surface atomic positions. For this purpose Electron Scattering Quantum Chemistry (ESQC) calculations have been applied to the case of an FeO monolayer on Pt(111) to simulate the experimental images. The correspondence between surface structure and STM image features has been determined. In particular, the maxima observed in the experimental images spaced by 3.1 Å are due to the positions of the oxygen atoms. The atomic corrugation has a simple relationship with the tip-surface distance and therefore with the surface buckling. Namely, the atomic corrugation increases with decreasing tip-surface distance. However, there is no simple relationship between the average tunneling current and topography. This is the first calculation of an STM image for a metal oxide surface as well as the first STM modeling of a Moiré structure.

Other studies include an investigation of the coadsorption of oxygen and sulfur on the Ni(110) surface. The results of the coadsorption experiments will be included in the last chapter. Further STM calculations using the ESQC method to compare the chemisorbed oxygen system to the metal oxide structures would enhance the understanding of tunneling in metal-oxygen systems.

Dedicated to

my husband

Rick Haas

and our children

Haley Claire Galloway
Austin Lamar Haas

born

November 12, 1994

Table of Contents

List of Figures

List of Tables

Chapter 1 Introduction

The primary goal of this work is to characterize the growth of thin films of metal oxides on metal single crystal surfaces to advance the status of metal oxide surface science and to investigate metal oxide/metal interfaces at the atomic scale. Thus, the focus is on the first few layers of growth where the interaction between the substrate and overlayer is the most prevalent.

1.1 Metal oxide surface science

While the vast majority of atoms that make up a macroscopic solid are not located at the surface, it is only at a surface or interface that one material can interact with another. Many properties of materials are examined theoretically and experimentally from the point of view of infinite solids, but the bulk defect of a surface is an essential reality in a finite world. Many important properties of materials that are encountered in practical problems involve surfaces, and as miniature devices are increasing in popularity and decreasing in size this trend promises to continue. This practical interest as well as the drive to understand the most significant bulk defect has led to the field of modern surface science where the goal is to understand surfaces and interfaces.

Surface science experiments on metals and semiconductors have been conducted for many years, yet the study of oxide surfaces has received less attention for a variety of reasons [1]. These include the difficulty in obtaining well ordered samples and the problem that these surfaces are difficult to clean using standard surface science techniques. Heating in vacuum may cause an oxygen deficiency and sputtering may also preferentially remove oxygen leading to non-stoichiometric surfaces and a general lack of ability to control the surface stoichiometry. Even cleaving in ultrahigh vacuum releases large amounts of energy and only some cleavage planes are available. In addition, metal oxides are often not conductive making electron spectroscopy techniques difficult due to charging effects.

These experimental difficulties mean that very few complete surface structure determinations exist for metal oxides. Out of almost 600 surface structures in the Atlas of Surface Structures [2], only fourteen are for oxide surfaces. Finally, and perhaps most importantly, any multi-component system has an added degree of complexity and the wide array of structures and stoichiometry that are possible for a single metal oxide system makes these surfaces challenging to understand. The number of atoms in a typical metal oxide unit cell is considerably larger than that of a metal or even the compound semiconductors. For example, rutile TiO_2 has six atoms in its basic unit cell and α-Fe_2O_3 has ten atoms. When stoichiometry variations and ordered arrays of defects are included the number of possible structures becomes enormous. This leads not only to ambiguity in interpreting experimental results, but theoretical models are also computationally difficult.

Not only are the ideal metal oxide surfaces not well characterized, but many studies indicate that defects play an enormous role in controlling both the chemical and physical properties of the surface [3]. For these reasons, scanning tunneling microscopy is an ideal tool to use for these systems as it can provide real space structural information. While other techniques are still clearly necessary, especially to provide chemically specific information as well as an indication of the average structure of the surface, STM is unique in its ability to probe the local atomic structure of metal oxides. In addition, the focus here is on thin films of metal oxides grown on metal single crystals for reasons which will be discussed in 1.1.2.

1.1.1 Applications

In spite of the paucity of basic research, metal oxide surfaces are very widely used in applications [1]. Many catalysts consist of metal particles dispersed on oxide supports. In some cases the oxide is simply an inert substrate but when the oxide is reducible, there is a strong interaction between the support and the metal particles that alters the catalytic

behavior, e.g. Pt on titania for CO hydrogenation [4]. Metal oxides are also used as catalysts by themselves or in mixtures of metal oxides. Oxide surfaces such as ZnO and SnO_2 are used as gas sensors because the adsorption of certain gases changes the surface conductivity. Small additions of metals often improve the reactivity or selectivity of the sensor. Magnetic oxides are used for high frequency transformer applications where their insulating properties are desirable. Also, most metal surfaces in air are terminated by oxide layers so any problem involving ambient conditions affecting metallic surfaces depends on the properties of an oxide surface. In particular the end product of environmental corrosion of a metal is an oxide surface. The discovery of high temperature superconducting oxides has also led to renewed interest in oxide properties.

1.1.2 Growth and epitaxy

The understanding of surfaces is in general only the first step for many technological problems where an interface is formed. As is seen in the list of applications, a metal/metal oxide interface is often involved in the technologically relevant system. This provides part of the motivation for concentrating this work on the growth of thin films of metal oxides on metals. Also from a basic research viewpoint, the understanding of epitaxy and growth for a variety of systems is one of the biggest challenges and focuses of investigations in surface science. In recent years the ability to study growth has been improved by the advances of scanning probe microscopies. Using Scanning Tunneling Microscopy (STM) the initial stages of growth which control the interface between the metal and metal oxide overlayer can be accessed. Even in systems such as metals on metals which were thought to be relatively simple, the advent of STM has revealed a dazzling variety of possibilities [5]. While the technique must be combined with other methods to gain a full understanding, STM is the primary technique used for these studies.

1.2 Metal oxide overlayers

The approach of growing ultrathin films has some advantages and disadvantages over the studies of bulk metal oxide surfaces. These films can be grown on a clean metal surface using simple vacuum techniques and by varying the pressure of oxygen and temperature, some degree of control over stoichiometry is obtained. Much is known about cleaning metal substrates and producing thin metal films with only very small amounts of contaminants. In addition, the major contaminant is carbonaceous species which are often removed by the oxidation process.

For films of only a few atomic layers thick, charging effects for electron spectroscopies are negligible and the films are conductive such that atomic scale features can be resolved by STM. Since these films are strongly influenced by the substrate, it is sometimes possible to stabilize surfaces or stoichiometries which are not observed for metal oxide single crystals [6]. This can be a disadvantage if the goal is simply to duplicate a bulk surface for chemical investigations [7]. However, it provides an opportunity to study novel materials which may eventually be important for applications.

Finally, for many surface science studies and especially for STM, an ordered surface is necessary to aid in understanding. While disordered surfaces are definitely important technologically they are not as well suited to the state of many surface science techniques at this time. This limits the systems that can be studied by this approach although the number of ordered metal oxide/metal systems that have been found to show ordering is increasing rapidly. A partial list is given in the following table.

Table 1.1 Ordered oxide overlayers

Overlayer	Substrate	Reference
Al_2O_3	NiAl(110)	[8, 9]
Al_2O_3	Ta(110)	[10]
FeO	Pt(100)	[11]
FeO	Pt(111)	[6, 12]
Fe_3O_4, α-Fe_2O_3	Pt(111)	[13-15]
MgO	$Cr_{0.7}Mo_{0.3}$(001)	[16]
MgO	Mo(100)	[7, 17, 18]
MgO/NiO	Mo(100)	[19]
MnO	Cu(001)	[20]
Na_2O	Pd(100)	[21]
NdOx	Cu(111)	[22]
NiO	Ag(100)	[23]
NiO	Au(111)	[23, 24]
NiO	Mo(100)	[25]
ZrO_2	Pt(111)	[26]

In principle, the growth of thin films can be understood as simply minimizing

$$\gamma_{over} + \gamma_{sub} + \gamma_{int} \quad (1)$$

where γ_{over} and γ_{sub} are the surface free energies per area of the overlayer and substrate and γ_{int} is the interfacial energy. However this framework only provides limited insight for a metal/metal oxide system because the energies for oxides and oxide interfaces are generally not well known. However, typical values of surface free energies of metal oxides are usually lower than those of metals. (MgO 1100-1200 ergs/cm^2 and Al_2O_3 900

ergs/cm^2 compared to Pt 2340 ergs/cm^2 and W 2900 ergs/cm^2 [27, 28]) This implies that the first layer of oxide on a metal will be driven to cover the surface of the metal.

Thin films of metal oxides are produced by evaporating a metal onto the single crystal surface and then heating in a pressure of oxygen. The temperature limits for the metal oxide overlayer systems are usually set by a lower bound where the overlayer does not oxidize or does not order, and an upper bound where the oxide layer desorbs or decomposes. At higher temperatures the metal used to form the overlayer oxide may even be soluble in the substrate. Using noble metal substrates has the advantage that the oxide layers can be formed at temperatures and oxygen pressures where the substrate does not form a bulk oxide layer.

1.3 Summary

The systems presented here include iron oxide and titanium oxide on Pt(111). The original focus for these systems was an interest in the catalytic properties, but they were chosen for this research primarily because they exhibit ordered structures. As the emphasis in this work is on the structural properties the majority of experimental results are from scanning tunneling microscopy. While this technique has become well established as an experimental tool, extracting information from STM images is still not a standard procedure. Methods of extracting structural information based on symmetry and the relationship of the overlayer to the substrate will be presented here. It is also common to observe tip and gap dependent images and results for these phenomena will be shown and discussed for these systems.

In an attempt to advance the understanding of the STM images of metal oxides, theoretical calculations by the Electron Scattering Quantum Chemistry method [29] are performed for the bilayer of FeO on Pt(111). While the STM images provide information about the surface atomic structure, the information is limited by the fact that the tunneling process does not have a simple correspondence with topography. These calculations

answer questions about how the components on the surface are contributing to the tunneling current and what the relationship is between the observed image and the actual surface topography. As this system involves a 10% lattice mismatch between substrate and overlayer, it can also be determined how this type of structure and the resulting surface buckling is affecting the images. In spite of the growing number of metal oxide scanning tunneling microscopy results, the modeling of the tunneling process at the atomic scale has been limited for these systems.

Other studies have been conducted on oxygen and sulfur coadsorption on Ni(110). The imaging mechanisms of S have been more thoroughly studied than those of oxygen [30, 31]. Thus, future calculations of the coadsorption results may also yield insights into tunneling in systems involving metal-oxygen bonds. Results of the chemisorption of S and O are also obtained as a result of this interest and are therefore included.

Chapter 1 References

[1] V.E. Henrich and P.A. Cox, Introduction in *The Surface Science of Metal Oxides* (Cambridge University Press, Cambridge, 1994)

[2] P. Watson, M.A. Van Hove and K. Hermann, *Atlas of Surface Structures: Volume 1A* , (American Chemical Society and American Insititue of Physics for the National Institute of Standards and Technology, New York, 1994).

[3] V.E. Henrich, Rep. Prog. Phys. **48,** 11 (1985) 1481.

[4] H.H. Kung, Reduction of Oxides in *Transition Metal Oxides: Surface Chemistry and Catalysis* (Elsevier, Amsterdam, 1989) 1.

[5] R.Q. Hwang, C. Gunther, J. Schroder and S. Gunther, J. Vac. Sci. Technol. A **10,** 4 (1992) 1970.

[6] H.C. Galloway, J.J. Benítez and M. Salmeron, Surf. Sci. **298,** 1 (1993) 127.

[7] M.-C. Wu, J.S. Corneille, C.A. Estrada, J.-W. He and D.W. Goodman, Chem. Phys. Lett. **182,** 5 (1991) 472.

[8] J. Libuda, F. Winkelmann, M. Baumer, H.-J. Freund, T. Bertrams, H. Neddermeyer and K. Müller, Surf. Sci. **318,** 1-2 (1994) 61.

[9] R.M. Jaeger, H. Kuhlenbeck, H.-J. Freund and M. Wuttig, Surf. Sci. **259,** 3 (1991) 235.

[10] P.J. Chen and D.W. Goodman, Surf. Sci. **312,** 3 (1994) L767.

[11] G.H. Vurens, V. Maurice, M. Salmeron and G.A. Somorjai, Surf. Sci. **268,** 1-3 (1992) 170.

[12] G.H. Vurens, M. Salmeron and G.A. Somorjai, Surf. Sci. **201,** (1988) 129.

[13] H.C. Galloway, J.J. Benítez and M. Salmeron, J. Vac. Sci. Technol. A **12,** 4 (1994) 1.

[14] W. Weiss and G.A. Somorjai, J. Vac. Sci. Technol. A **11,** 4 (1993) 2138.

[15] W. Weiss, A. Barbieri, M.A. Van Hove and G.A. Somorjai, Phys. Rev. Lett. **71,** (1993) 1884.

[16] S.A. Chambers, Y. Gao and Y. Liang, Surf. Sci. **339,** 3 (1995) 297.

[17] J.S. Corneille, J.-W. He and D.W. Goodman, Surf. Sci. **306,** 3 (1994) 269.

[18] M.-C. Wu, C.M. Truong and D.W. Goodman, Phys. Rev. B **46,** 19 (1992) 12688.

[19] M.L. Burke and D.W. Goodman, Surf. Sci. **311,** 1-2 (1994) 17.

[20] D. Tian, H. Li, S.C. Wu, J. Quinn, Y.S. Li and F. Jona, Phys. Rev. B **46,** 11 (1992) 7216.

[21] H. Onishi, T. Aruga and Y. Iwasawa, Surf. Sci. **310,** 1-3 (1994) 135.

[22] E.A. Shaw, R.M. Ormerod and R.M. Lambert, Surf. Sci. **275,** (1992) 157.

[23] K. Marre and H. Neddermeyer, Surf. Sci. **287-288,** (1992) 995.

[24] C.A. Ventrice, T. Bertrams, H. Hannemann and A. Brodde, Phys. Rev. B **49,** 8 (1994) 5773.

[25] C.M. Truong, M.-C. Wu and D.W. Goodman, J. of Chem. Phys. **97,** 12 (1992) 9447.

[26] V. Maurice, M. Salmeron and G.A. Somorjai, Surf. Sci. **237,** (1990) 116.

[27] G.A. Somorjai, Introduction in *Chemistry in Two Dimensions: Surfaces* (Cornell University Press, Ithaca, 1981) 31.

[28] S.J. Gregg, The Solid-Solid Interface in *The Surface Chemistry of Solids* (Reinhold Publishing Corporation, New York, 1961) 137.

[29] P. Sautet and C. Joachim, Phys. Rev. B **38,** 17 (1988) 12238.

[30] J.C. Dunphy, P. Sautet, D.F. Ogletree and M.B. Salmeron, J. Vac. Sci. Technol. A **11,** 4 (1993) 1975.

[31] P. Sautet, J.C. Dunphy, D.F. Ogletree, C. Joachim and M.B. Salmeron, Surf. Sci. **315,** 1-2 (1994) 127.

Chapter 2 Experimental Methods

2.1 Sample preparation

The samples used as substrates for these studies are all metal single crystals. They are first oriented by Laue X-ray diffraction to the desired low index plane surface, cut, and polished [1]. The crystal is mounted flush in a cylinder of resin for easier handling while polishing. For polishing platinum, the next steps consist of using finer and finer grades of SiC sand paper with an oil lubricant. Scratches are made in orthogonal directions so it is clear when all the scratches from the previous grade have been removed. Then the crystal is polished on a wheel using diamond paste of 6 μm and then 1 μm particle size. A final polishing using the finest grade alumina powder (.25 μm particle size) in a water based slurry produces a mirror like finish. The crystals are then removed from the resin and mounted onto sample holders by spot welding thin strips of tantalum across them. The rest of the sample preparation is done *in situ* in an ultra high vacuum chamber.

2.1.1 Ultrahigh vacuum chamber

Studies carried out for this dissertation were primarily conducted in the standard ultrahigh vacuum chamber schematically depicted in Fig. 2.1 (modified PHI 590 Scanning Auger system). The single crystal samples were mounted onto a sample holder that can be rotated to face the various preparation and analysis facilities in the chamber. As is shown in the figure, these include a cylindrical mirror analyzer with integral electron gun, a quadrupole mass spectrometer for residual gas analysis, an ion sputtering gun, metal evaporation sources (only one of the two available is depicted) and a scanning tunneling microscope. The entire chamber is mounted on laminar air flow vibration isolation legs (air legs).

Crystal heating is by electron bombardment when the sample is mounted on the manipulator. A voltage of up to 5 keV is applied between the hot W filament and the sample to accelerate thermally emitted electrons into the back of the sample. Due to the close proximity of the sample and filament this produces minimal heating of the sample holder. For STM, the holder is simply set onto the outer tube of the microscope (see Fig. 2.4) and the manipulator is lowered slightly and retracted.

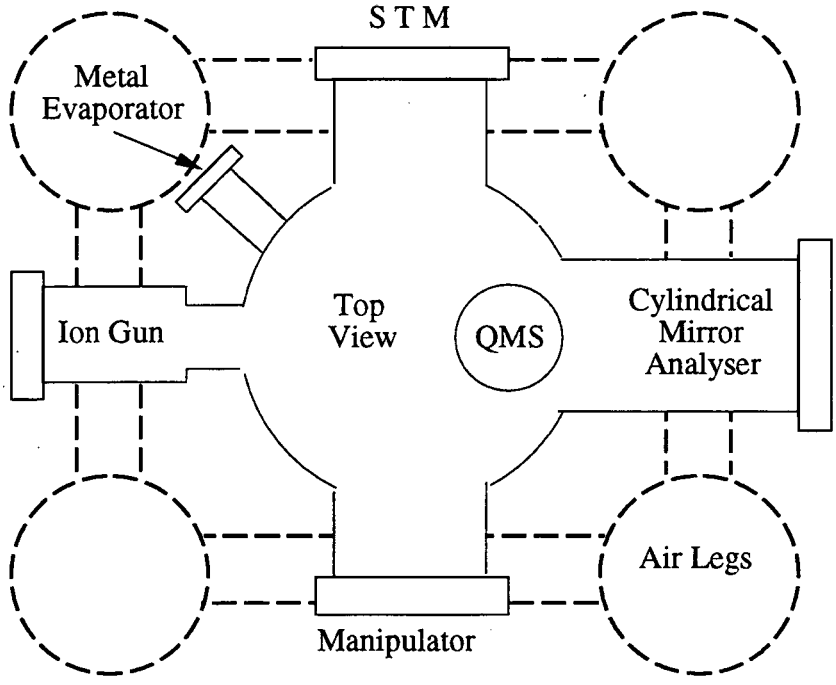

Figure 2.1 Schematic top view of the ultrahigh vacuum chamber The air legs and support frame are the dashed lines and the solid lines are the outlines of the UHV system.

Rough pumping is provided by a turbomechanical pumping station which is turned off once the chamber is under high vacuum. Only an ion pump and intermittent use of a Ti sublimation source are used to maintain vacuum when performing STM measurements to minimize vibrational noise. Typical base pressures when running

experiments range from 5 x 10^{-10} torr to 3 x 10^{-9} torr and the background pressure is composed primarily of CO and H_2.

2.1.2 Sample cleaning

The basic method for cleaning the surfaces of a single crystal is to perform repeated cycles of annealing, ion sputtering and heating in a reactive gas such as oxygen. For the Pt(111) and Rh(111) surfaces the cycle consisted of removing a layer of contaminants by sputtering with 700-1000 eV Ar^+ using the ion gun depicted above. The crystal is then heated to approximately 500-600 C in a pressure of oxygen and then finally annealed to 800-1000 C in vacuum. Sample temperatures can be measured to ±50-100 C by optical pyrometer or by pushing the corner of the sample into a thermocouple mounted in the chamber. In general, for approximate temperatures like those used for cleaning the sample temperature is approximated by visual inspection. For the Ni(110) surface the cycle is essentially the same with lower annealing and oxidation temperatures.

For these metals, most common contaminants are easily identified using Auger Electron Spectroscopy (AES). However, Si is very difficult to detect on Pt and Rh. The major Auger transition occurs at 92 eV [2] which overlaps with low energy Auger transitions for Pt and Rh. Si also surface segregates meaning that even for very small amounts a substantial surface coverage can be achieved [3, 4]. The kinetics of this system have been studied in detail. By AES the best way to measure the Si on these metals is to form the oxide by heating in a pressure of oxygen and then cooling after closing the oxygen valve and removing the oxygen gas from the chamber. Especially on Pt, oxygen desorbs just above room temperature so any oxygen still left on the crystal must be as a result of other contaminants. Oxygen detected by AES using this procedure is most often an indication of the presence of Si. It has also been shown that impurities can pin steps on metal surfaces leading to an increased step density and eventually to a rough surface [5]. Removal of Si contamination is virtually impossible and due to the

surface segregation it often becomes worse with time. While Si contamination led to the destruction of a Rh(111) crystal at the beginning of this work, the Pt crystals have not shown measurable Si contamination.

2.1.3 Metal oxide overlayer deposition

After the sample is free of contaminants, a metal oxide overlayer is formed by evaporating the metal from a tungsten filament assembly. This consists of a .030" diameter W wire wrapped with a .010-.020" diameter wire of the metal to be evaporated. The whole assembly is cleaned in a solution of dilute hydrochloric acid and then rinsed in methanol or acetone. A current of between 20-30 A is passed through the filament and the usual rate of deposition is ~1 ML/min as determined by calibration using Auger Electron Spectroscopy in combination with the STM. This method of evaporation works well for metals such as Ti and Fe which do not easily alloy with W and have a much lower melting point than the W filament itself [6]. The oxide is then formed by heating the entire crystal in a pressure of oxygen. For these studies, the oxygen pressures used range from $1x10^{-4}$ - $5x10^{-7}$ torr at temperatures ranging from 300-800 C. The relative amounts of surface contaminants and the amount of overlayer deposited are determined using AES.

2.1.4 Auger Electron Spectroscopy

Auger Electron Spectroscopy provides a method of determining what chemical species are present in the first few atomic layers. An electron beam with an energy of 2-3 keV is directed onto the sample and then the electrons ejected from the sample are collected and energy analyzed. An Auger electron is one that is ejected as is depicted in Fig. 2.2. An electron in an inner shell is ejected by the electron beam and an electron from the outer shell drops down to take its place. This process proceeds by the emission of a photon or in the Auger process the energy is transferred to an electron in the outer shell which is then ejected [7]. The energy of the ejected electron is given by

$$\Delta E = E_K - E_{L1} - E_{L3} \quad (1)$$

where the subscripts refer to the levels depicted in Fig. 2.2.

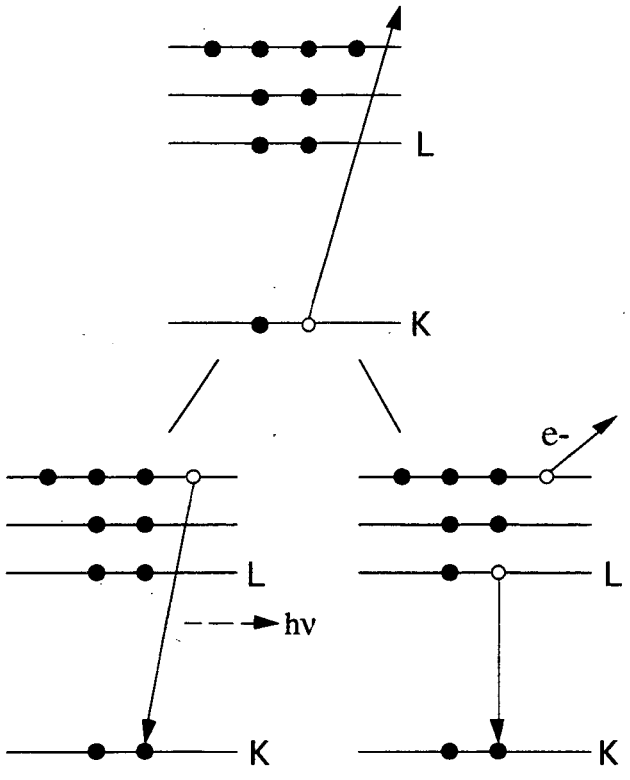

Figure 2.2 Auger electron process

First the K level electron is removed by an incident electron or photon. Then another electron can drop down a level by emission of a photon as is depicted in the lower left. Or as in the Auger process depicted on the lower right, an electron drops to fill the lower level and the excess energy is transferred to an electron which is ejected from the solid and enters the analyzer.

As this energy is specific to the element, chemical species present on the surface can be determined. The method is surface specific because only the Auger electrons ejected from the first few layers below the surface escape the sample to be analyzed. The most popular method of measuring a spectra is to modulate the voltage of the cylindrical

mirror analyzer, which measures the number of electrons emitted at a given energy, with a small AC voltage (2-4 volts). A lock-in amplifier is used to detect the signal and a differential spectra, dN(E)/dE, is recorded, where N(E) is the number of electrons emitted with an energy E. These spectra can be easily compared to reference spectra [2] to determine the elements present on the surface.

Qualitative information for AES is valuable but what is really needed is a quantitative measure of what is on the surface and this can only be accomplished by making some sort of calibration series or by comparison with another technique. The metal oxide overlayers are distinguishable from the substrate in the 0-1 ML regime by STM. This provides an experimental method of determining a calibration point for completion of the first monolayer. Systematic error is introduced if the structure of the overlayer changes for successive layers as is often the case for metal oxides. This means that coverages > 1 ML are prone to larger error in the coverage determination. However, the conclusions reached in this work are not dependent on precise knowledge of the coverage.

2.2 Scanning Tunneling Microscopy

The first scanning tunneling microscope was demonstrated by Binnig and Rohrer in 1982 [8-10] who were subsequently awarded the Nobel Prize in Physics. The methods of scanning probe microscopies have since become routine for characterization of surfaces and there are several reference works available [11-17]. Only some of the more salient points will be summarized here.

2.2.1 Theory

The basic idea of scanning tunneling microscopy is that when a conducting tip and sample are brought close to each other (few Å distance) and a voltage is applied between them, electrons can tunnel from one to another. This is predicted by quantum mechanics. At a finite barrier the electron wave functions do not go to zero but decay exponentially

outside the barrier. A schematic of the energy levels and wave function is shown in Fig. 2.3. For a positive sample bias, the states of the sample are shifted down in energy relative to the tip and electrons from the tip can tunnel into empty states of the sample. For negative sample bias, tunneling is from filled states on the sample to empty states on the tip.

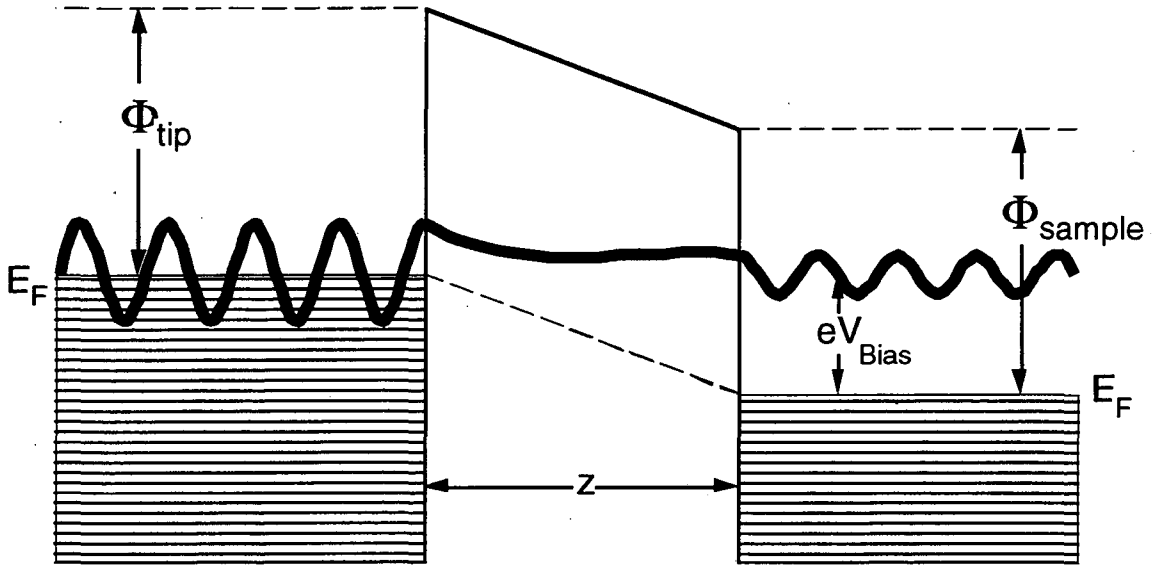

Figure 2.3 Simplified energy levels in tunneling conditions
The Fermi levels of the tip and sample are shifted by the energy eV_{Bias} allowing electrons to tunnel from filled states on the tip to empty states on the sample through a trapezoidal barrier. The heavy line schematically represents the wave function amplitude.

The basic one-dimensional tunneling theory for a trapezoidal barrier is given approximately by

$$I \propto V \exp(-A\sqrt{\Phi}z) \tag{2}$$

for

$$\Phi = \frac{\left(\Phi_1 + \Phi_2 - e|V_{Bias}|\right)}{2}, \tag{3}$$

where I and V_{Bias} are the tunneling current and voltage, A is a constant, Φ_1 and Φ_2 are the work functions of the tip and sample, and z is the distance between them. The exponential dependence in z is what provides the sensitivity to surface structure. For typical tunneling parameters, a 1 Å change in z corresponds to an order of magnitude change in the current.

Many refinements to the tunneling theory have been proposed and tested and one (ESQC) will be discussed in this work. The most useful general picture of STM is probably that from the work of Tersoff and Hamann [18]. Their calculations show that for a tip modeled only by a point source *the tunneling current is proportional to the local electronic density of states at the Fermi level measured at the position of the tip*. It is important to remember that the electronic density of states is not always a maximum at atomic positions. Limitations of this model are that the influence of tip structure (both geometric and electronic) are neglected and contributions from states farther away from the Fermi level are also neglected. For small tip sample distances it may also be necessary to include the perturbation of the sample by the tip. In addition since tunneling is quantum mechanical the possibility of interfering amplitudes from electrons that tunnel through different paths must also be considered.

2.2.2 STM design

The STM used in these studies is 'homemade' and consists of two concentric piezoelectric cylinders (similar to that in Ref. [19]). The outer piezo with an OD of .875" is used for approaching the sample to the tip and for x, y, and z offsets. It is soldered at one end to a mounting ring and to an anodized aluminum tube on the other end which holds the sample. The inner piezo is not visible in Fig. 2.4 but holds the tunneling tip and provides the feedback response for maintaining a constant tunneling current and also scans to acquire images. The inner piezo has an OD of 0.125".

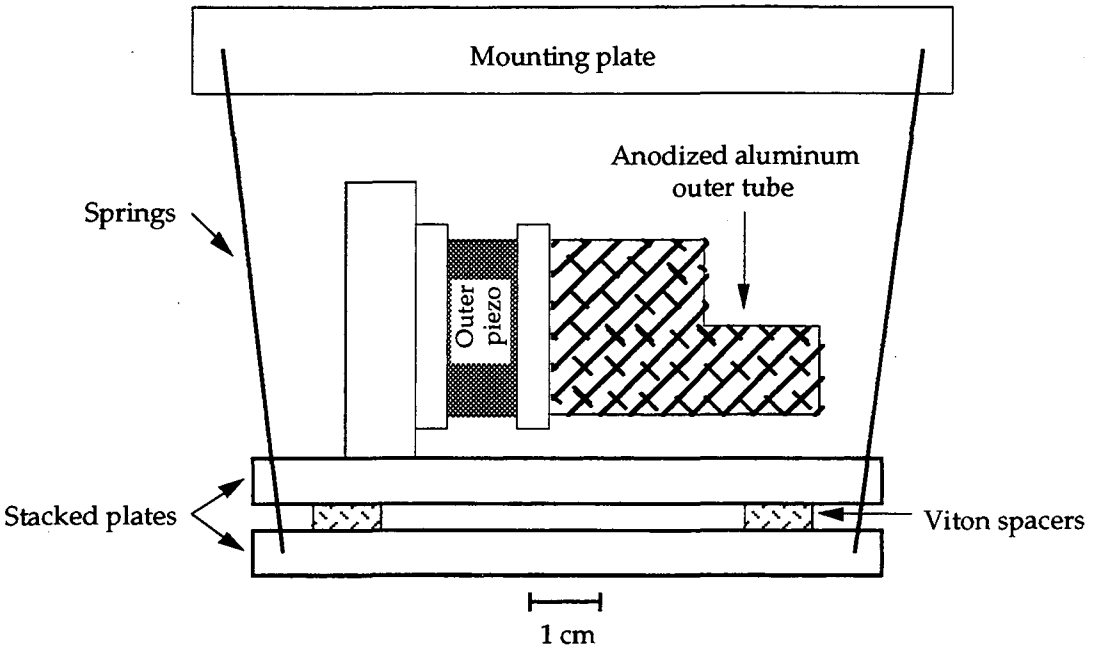

Figure 2.4 STM schematic

The STM is shown in side view. The outer piezo and outer tube are cylinders. The springs, stacked plates and viton spacers are to reduce vibrational noise. (In practice, the "viton" is actually a silicone compound that is more UHV compatible.)

The tip used is a .010" diameter wire that is bent to make a simple spring and inserted into a No. 20 syringe needle mounted in a small piece of Macor. A UHV compatible epoxy (Appendix I) is used for assembling the tip holder and attaching it to the piezo. Other joints are held mechanically rigid with standard screws except for the piezo mounting. By using nickel plated aluminum for the piezo mounting rings, the nickel coating of the piezo can be soldered directly onto the mountings. This method has been found to be durable and rigid as well as allowing the piece to be reheated and the piezos removed for replacement unlike permanent epoxies. (Appendix I contains a list of

supplies and procedures pertinent to the specialized materials used for building this ultrahigh vacuum scanning tunneling microscope.)

STM studies are performed by positioning the sample onto the outer tube of the microscope in the vacuum chamber. The course and fine approach are accomplished by an inertial mechanism. An asymmetric wave form is applied to the outer piezo which moves the sample and tube slowly in, and then quickly the tube is moved out so that the sample slips inwards with respect to the tube. Steps as small as a few hundred Å are possible. Directions are simply reversed to move the sample out.

2.2.3 Tunneling tip

Tips are usually Pt/Rh wire which is chosen for its hardness and lack of an oxidation layer in ambient conditions (or in the pressures of oxygen used to grow oxides). It is generally desirable to be able to clean the tip by heating or to replace tips in situ. The current design of the STM does not allow this so tips are etched to a sharp point (Appendix I) and checked with an optical microscope and then tried on HOPG (highly oriented pyrolytic graphite) in air. Only when atomic resolution is achieved in air is the microscope put into vacuum.

In situ it is possible to apply voltage pulses to the tip. Small voltage pulses, ~1-10 V, sometimes result in a tip change (although not always an improvement). By disconnecting the STM electronics and connecting a simple circuit, a method of field emission can be tried to more drastically alter the tip. As is seen in Fig. 2.5, a high voltage is applied between tip and sample and the current is monitored by watching the voltage drop across a resistor (R2) on an oscilloscope. The resistor (R1) in the circuit is simply a fuse to prevent a high current from flowing in case of a short. For tip sample distances of ~1-2 μm (several 'steps' back using the inertial approach), voltages of 400-600 V produce a current of 1 μA. Generally a current of 1 μA for approximately one minute is tried. This procedure is sometimes effective in improving tip stability.

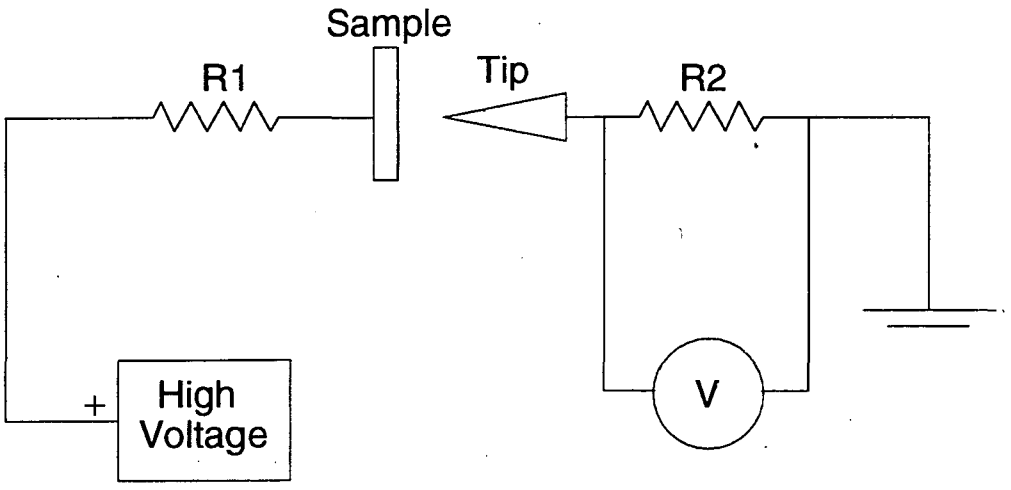

Figure 2.5 Field emission circuit diagram

The circuit used for attempting to improve tip stability by field emission is shown. The voltage labeled V is usually displayed on an oscilloscope so the time dependence of the current is visible as well as the magnitude because the current does not stabilize immediately.

2.2.4 Piezoelectrics

The availability of piezoelectric transducers is what makes scanning probe microscopes relatively simple to construct. However, they also limit the technique so it is important to understand how they operate. The basic operating principle is depicted in Fig. 2.6. When an electric field is applied parallel to the direction of polarization the piezo expands in that direction and contracts perpendicular to it. Since the volume is conserved there will also be a contraction of the piezo in the direction perpendicular to the applied field. Reversing the field reverses the direction of motion.

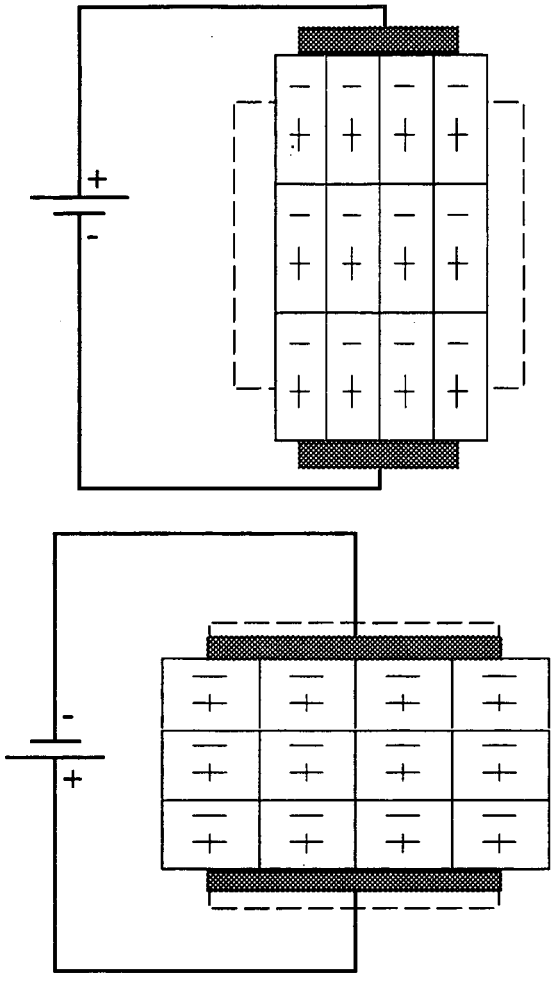

Figure 2.6 Principle of piezoelectric operation

In the top half of the figure, the field is applied in the direction of polarization (both up) and the piezo expands in that direction. In the lower half the field is reversed by changing the sign of the applied voltage. The dotted line represents the size of the piezo when no field is applied.

The microscopic view of piezos is similar to that of ferromagnets in that they are not single crystals and are instead composed of domains mostly aligned in one direction. The piezos can be depolarized by heating above the Curie point, which is 190 C for

Stavely EBL 3 PZT material (lead zirconate titanate) and repolarized by heating to a substantial percentage of the Curie temperature (50-100 C) and cooling in a strong field (~1000 V/mm).

The geometry used for this STM consists of cylinders with the outer electrode divided into four sectors. The piezo is polarized in the radial direction. (The default direction for polarization for tubes supplied by Stavely Sensors, EBL Division is radially outward or with the outer electrode at a higher potential than the inner one.) A field applied between the outer and inner electrodes causes the piezos to expand in the radial direction for a field parallel to the polarization. The piezos will also contract along the cylinder length and this is used to provide z motion perpendicular to the surface. A voltage applied between two opposing outer sectors causes one side of the piezo to shorten while the other expands. This causes a bend in the cylinder and provides x-y motion. The x-y deflection is given by

$$\Delta x,y = \frac{\sqrt{2}d_{31}(\Delta V)L^2}{\pi D h} \tag{4}$$

and the z motion by

$$\Delta z = \frac{d_{31}(\Delta V)L}{h} \tag{5}$$

where ΔV is the voltage difference between the two electrodes, L is the length of the cylinder, h is the wall thickness, D is the diameter of the cylinder, and d_{31} is the piezoelectric coupling coefficient inherent to the material [20]. Typical piezos have a length of 0.5-1.0", diameters of 0.125-1.00" and wall thicknesses of 0.01-0.02". The values of d_{31} for different materials range from 1-1.7 Å/V. The relative motion of x and y compared to z should only depend on geometrical factors.

$$\frac{\Delta z}{\Delta x,y} = \frac{\pi D}{\sqrt{2}L} \tag{6}$$

This is easy to check by comparing x, y, and z calibration values.

The limitations imposed by the piezos are that they have thermal drift and even small variations in temperature cause large motions compared to the atomic scale. Symmetric arrangements of piezos are chosen to provide compensation for this effect. Furthermore, as with ferromagnetics, piezoelectrics inherently exhibit creep and hysteresis which can cause severe problems for scanning probe microscopies. Hysteresis refers to the fact that the same field does not always result in the same net displacement depending on whether the field is increasing or decreasing. Creep refers to the fact that the piezo only approaches its final length logarithmically so the amount of displacement depends on how fast the voltage is changing [21]. These problems are clearly apparent in atomic scale imaging.

As these problems are inherent in all piezoelectric materials to some degree, STM is not the best technique for measuring lattice constants to high precision. In the cases when a known and unknown structure are both imaged simultaneously, the known structure may be used as a template for calibration. Otherwise, even with careful pre-calibration of the instrument, it is difficult to reduce accuracies in distance measurements to a level below 10%.

2.2.5 Noise

In practice, the z resolution of most STM experiments is limited by noise. To understand the sources and solutions of various problems it is instructive to consider them by frequency range. In the several to tens of Hz range, building vibrations are the biggest source of mechanical noise. Mounting the UHV chamber on air damped legs like those used for optical tables can help reduce noise in this regime. Acoustical vibrations in the few hundred to few kHz regime are somewhat blocked by mounting the microscope to the UHV chamber with a damping mechanism. For this system, springs and stacked plates separated by viton spacers are used as shown in Fig. 2.4. The relative effects of

various systems can be tested using an accelerometer to compare vibrations at different locations.

The best method of avoiding mechanical noise is to build a microscope head that is small, lightweight, and rigid. This means that the frequecy of the lowest will be higher (> several kHz would be better) and so lower frequency vibrations will have little effect. A method of measuring microscope resonance frequencies is summarized in Appendix II.

Electrical noise sources can also be classified by frequency and can be distinguished from mechanical problems by using a low noise resistor (~100 MΩ) in place of the STM. Possible sources include 60 Hz line noise from ground loops, kHz range noise from digital displays on the electronics, 10^4 Hz range from a computer monitor and MHz frequencies from the computer itself. Although the bandwidth of the STM measurement is only of the order of 10^4 Hz, and the feedback has an even smaller bandwidth, large high frequency noise can still affect the measurements if the noise gets into the A/D conversion before going to the computer or by aliasing to lower frequency. Ground loops are an especially common problem and are discussed in Ref [22] as are most major issues relating to the current measurement noise in a typical STM experiment.

The major tool used in this laboratory to improve noise performance is to take FFT (Fast Fourier Transforms) of the tunneling current, feedback response, and other voltage outputs to identify the frequency behavior and consequently the source of the problem. This can also be aided by using a low noise resistor in place of the tunneling gap to separate electrical and mechanical components.

2.2.6 Resolution limits

The tunneling measurement is essentially measuring a small current. Two fundamental limits on this process are the Johnson noise of resistive elements and the shot noise of the tunneling current. Johnson noise is due to thermal fluctuations of electrons. For a resistor of value R, the rms current noise in amps is given by

$$I_{rms} = \left(\frac{4kTB}{R}\right)^{1/2} \tag{7}$$

where T is the temperature in degrees Kelvin, B is the bandwidth in Hz and R is the value of the resistor in ohms. At room temperature and for a bandwidth of 10 kHz, a 10 MΩ resistor, has an rms noise current of $I_{rms} = 4.1$ pA. For a typical tunneling gap with an average barrier $\Phi = 5$ eV the 1-D approximation in 2.2.1 predicts a z noise of .18 pm. The shot noise for a dc current due to statistical noise associated with the electrons is given by a similar expression

$$I_{rms} = (2qI_{dc}B)^{1/2} \tag{8}$$

For a typical current of 1 nA and a bandwidth of 10 kHz, $I_{rms} = 1.8$ pA, again the associated noise in z is 0.08 pm. These noise sources can be reduced somewhat by lowering the temperature to reduce Johnson noise and reducing bandwidth to limit both sources but they are already quite small for most experiments. A typical value of the best resolution achieved for these experiments is 0.1 Å or 10 pm. The lateral resolution is basically limited to features the size of the atomic dimensions due to the deBroglie wavelength of the electrons (on the order of an angstrom for electrons at an energy near the Fermi level).

In addition there is 1/f noise associated with real electronic devices and this dominates the noise spectra at low frequencies. The limitation in resolution of the STM design presented here is not from these sources, but is due to mechanical vibrations. Particularly under real tunneling conditions, contributions to the tunneling current can easily be seen at the microscope resonance frequencies (the microscope resonance frequencies can be easily measured by the method detailed in Appendix II). The typical noise level for this instrument is closer to 0.1-0.3 Å depending on the particular gap conditions. Atomic scale corrugations vary widely from several Å reported on HOPG which is easily measurable to close-packed metal surfaces where the atomic corrugation is only a few hundredths of angstroms and not detectable with this instrument.

2.2.7 Image modes and processing

Two primary methods of acquiring STM images are used and are depicted in Fig. 2.7. One usually called topographic, is where the tip is moved up and down to keep the current at some set point as the tip is scanned in x and y. The data plotted is in units of Å relative to the surface although the absolute distance to the surface is not known. A second mode of imaging is called current imaging (sometimes constant height imaging). In this method the tip is not moved up and down but scanned at a "constant" height across the surface and the current as a function of x and y is recorded. The data is then in units of current (typically nA). In practice, the feedback is still functioning but the time constant is increased so that the tip does not follow the small variations in current across the surface. This method only works where the topographic changes in the surface are small (so the tip does not run into the sample) and the primary advantage is that images can be acquired at faster rates.

The software used to control the STM electronics runs on a PC (386 or newer) and is now called SPiMage, by D.F. Ogletree [23]. This program has had several reincarnations and improved dramatically during the course of this thesis project. The program now allows the recording of more signals simultaneously as well as more complicated imaging modes including taking spectroscopic data concurrently with imaging.

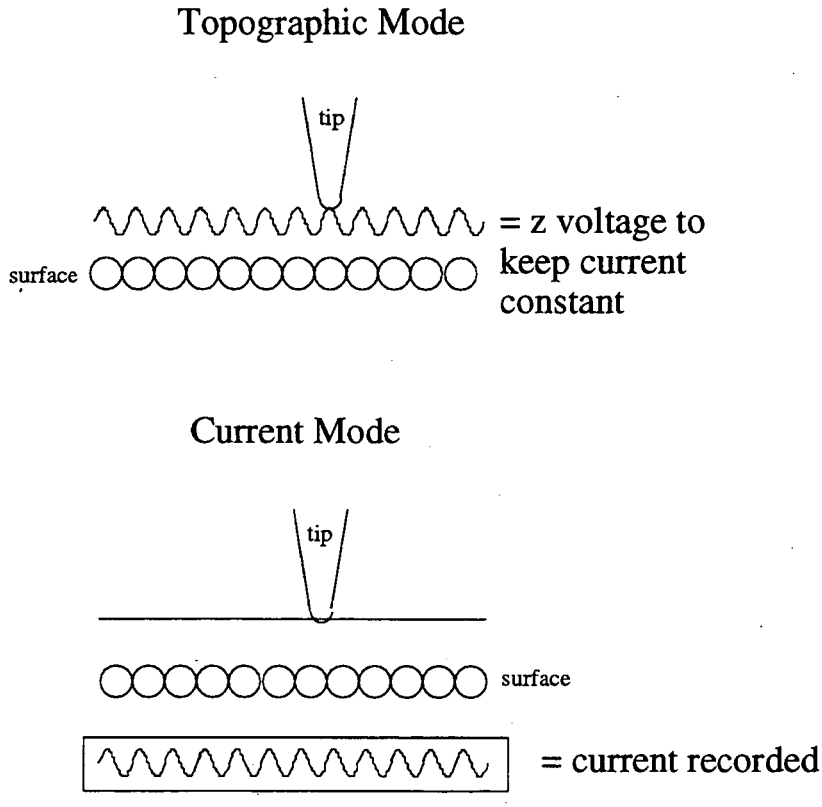

Figure 2.7 Imaging modes

The two most commonly used imaging modes, topographic and current are schematically shown along with the signal that is acquired for each from a hypothetical surface.

Several image processing routines are commonly used to analyze data. These include the following:

1) Plane subtraction - An (x, y) plane is subtracted from the image. This can either be fit to the entire image or the user can pick areas on a single terrace to preserve step heights. This does not alter the physical meaning of the data as it simply corrects for the fact that the tip is not actually scanned parallel to the sample surface.

2) Parabola subtraction - This is the same as plane subtraction except that a second order polynomial is fit instead. This removes some of the effects of thermal drift and piezo nonlinearities and can actually alter some values such as the height of steps. However, on a single crystal metal surface where it can be safely assumed that the terraces are flat, it is an appropriate technique.

3) X,Y offset subtraction - This finds the average z value for each scan line and sets them to the same value. This has the effect of removing very low frequency noise and reducing large changes in z when a tip change occurs. Because this method can remove important information (like where a tip change occurred) it should not be performed before saving the data.

4) Fourier filtering - This takes a 2D fast Fourier transform and applies a filter in Fourier space before transforming the data back to the real space image. This is extremely effective in removing high frequency noise due to resonances of the microscope. While it is reasonable to assume that on a surface with a 3 Å spacing that a 0.5 Å spatial frequency is not due to the surface and only to noise, applying a filter can introduce other frequencies (especially for a square cut off) and this method can definitely be abused. Images that have been 'over filtered' when the cut off of the filter is set too close to the real space frequencies of the image appear 'out of focus'.

5) Lattice correction - image calibration and skew - This is used for an atomically resolved image where lattice vectors can be drawn across the image. In this case the image calibration can be adjusted as well as the skew or angle between the x and y axes. This is only valid for cases in which the lattice vectors of the surface are known and is useful for comparison of two structures in the same image. (Due to imperfections in the piezos and in construction of the microscope the x and y axes are not exactly perpendicular.)

These will not be specified for the images reproduced herein unless they alter the analysis, but only plane subtraction is performed before raw data is saved. While it is often necessary to use some kind of filtering for clear reproduction the criteria listed above have been used to guide the process. In some cases editing the color table is used to emphasize a particular feature or to see the atomic contrast in adjacent terraces and this is noted in the figure captions.

Chapter 2 References

[1] W. Heppler, *Crystal Preparation at LBL 1976 to 1986*, Lawrence Berkeley Laboratory, PUB-3078, (1989).

[2] L.E. Davis. *Handbook of Auger Electron Spectroscopy* . (Physical Electronics Division, Perkin-Elmer Corp., Minnesota, 1978).

[3] H. Niehus and G. Comsa, Surf. Sci. **102,** (1981) L14.

[4] M. Salmeron and G.A. Somorjai, Journal of Vacuum Science and Technology **19,** (1981) 722.

[5] J.F. Wolf, B. Vicenzi and H. Ibach, Surf. Sci. **249,** 1-3 (1991) 233.

[6] C.V. Deshpandey and R.F. Bunshah. Evaporation Processes in *Thin Film Processes II* (Academic Press, Inc., San Diego, 1991) 79.

[7] H.E. Bishop. Auger electron spectroscopy in *Methods of surface analysis* (Cambridge University Press, Cambridge, 1990) 87.

[8] G. Binnig, H. Rohrer, C. Gerber and E. Weibel, Phys. Rev. Lett. **50,** (1983) 120.

[9] G. Binnig, H. Rohrer, C. Gerber and E. Weibel, Phys. Rev. Lett. **49,** (1982) 57.

[10] G. Binnig, H. Rohrer, C. Gerber and E. Weibel, Phys. Rev. Lett. **40,** (1982) 178.

[11] R. Wiesendanger and H.-J. Guntherodt. *Scanning tunneling microscopy III: theory of STM and related scanning probe methods* . (Springer-Verlag, Berlin, New York, 1993).

[12] R. Wiesendanger and H.-J. Guntherodt. *Scanning tunneling microscopy II: further applications and related scanning techniques* . (Springer-Verlag, Berlin, New York, 1992).

[13] J.A. Stroscio and W.J. Kaiser. *Scanning Tunneling Microscopy* . (Academic Press, Boston, 1993).

[14] H. Neddermeyer. *Scanning tunneling microscopy* . (Kluwer Academic Publishers, Dordrecht, 1993).

[15] H.-J. Guntherodt and R. Wiesendanger. *Scanning tunneling microscopy I: general principles and applications to clean and adsorbate-covered surfaces* . (Springer-Verlag, Berlin, New York, 1992).

[16] C.J. Chen. *Introduction to scanning tunneling microscopy* . (Oxford University Press, New York, 1993).

[17] R.J. Behm, N. Garcia and H. Rohrer. *Scanning tunneling microscopy and related methods* . (Kluwer Academic Publishers, Dordrecht, 1990).

[18] J. Tersoff and D.R. Hamann, Phys. Rev. B **31,** 2 (1985) 805.

[19] D.M. Zeglinski, D.F. Ogletree, T.P. Beebe and R.Q. Hwang, Rev. Sci. Instr. **61,** 12 (1990) 3769.

[20] C.J. Chen, Appl. Phys. Lett. **60,** 1 (1992) 132.

[21] S.M. Hues, C.F. Draper, K.P. Lee and R.J. Colton, Review of Scientific Instruments **65,** 5 (1994) 1561.

[22] P. Horowitz and W. Hill. Precision Circuits and Low-Noise Techniques in *The Art of Electronics* (Cambridge University Press, Cambridge, 1989) 391.

[23] SpiMage v. 3.2, by D.F. Ogletree (RHK Technology, Rochester Hills, Michigan, 1985-1995).

Chapter 3 FeO on Pt(111)

3.1 Introduction

Iron oxide is used for catalytic applications like many other metal oxides. In addition, the iron oxides have magnetic properties that have been of interest to researchers, including some attempts to observe magnetic contrast with STM by using single domain magnetic tips [1, 2]. However, in these studies only structural information will be presented. As is typical for most transition metal oxides, there are several structures and stoichiometries that are observed to be stable. These also have a wide variety of properties and include the ferrimagnetic conductor, Fe_3O_4, and the antiferromagnetic insulator α-Fe_2O_3. In addition, FeO which is antiferromagnetic and has a band gap of 2.4 eV [3] is not an equilibrium structure at room temperature and is always observed to be substoichiometric in bulk form. The magnetic properties and the availability of single crystals have encouraged several surface structural studies, such as on the $Fe_3O_4(001)$ [4] and doped α-$Fe_2O_3(0001)$ [5-9] surfaces. These studies have shown that there is a tendency for complex surface reconstructions that may include stoichiometry changes in the surface layers.

Ordered structures of iron oxide on Pt(111) were first reported by Vurens, et al, [10] using low energy electron diffraction (LEED). At coverages of ~1 ML as determined by ion scattering spectroscopy and Auger uptake curves, a structure with a large unit cell was observed. At higher coverages, different ordered structures occur that will be discussed in Chapter 4. Furthermore the stoichiometry of the monolayer structure was determined to be FeO using X-ray photoelectron spectroscopy [11]. Although FeO is not a common form of bulk iron oxide, it has been observed to form at the surface of an iron single crystal or at other interfaces in UHV conditions [12-17]. FeO has the simple rocksalt structure (like NaCl) and based on the LEED data, an overlayer composed of a bilayer of iron and oxygen in a FeO(111) plane was proposed.

The lattice constant of bulk FeO is 3.05 Å compared to the lattice constant of 2.77 Å for the Pt(111) surface so there is a 10% misfit if the bulk value is preserved leading to a non-coincidence structure with a large unit cell. Although no other evidence was available and LEED calculations were not attempted, it was proposed that the surface is oxygen terminated. This assumption is reasonable since iron has a valence of +2 in FeO and can have a valence of either +2 or +3, it still has an electron available for bonding to the Pt while O in the -2 configuration has already satisfied its bonding requirements by being on the outside layer. As will be shown here, this basic model has been confirmed by experiments using STM and X-ray Photoelectron Diffraction. Moreover, some additional details of the structures are revealed in the STM images and a quantitative determination of the FeO lattice constant can be performed. XPD measurements have measured the FeO bond angle with respect to the surface and confirmed the oxygen termination. A brief summary of those results will be given here. Although theoretical modeling of LEED intensity vs. energy curves is by far the most widely used quantitative surface structural technique [18], large unit cells are still difficult for any computational technique including LEED calculations, making this system particularly suited to STM studies.

3.2 Experimental

As described in Chapter 2, the Fe is thermally evaporated onto the substrate and then the entire crystal is heated in oxygen at a temperature of 750 C in a pressure of oxygen between 5 x 10^{-7}-5 x 10^{-4} torr for ~ 30 sec. The monolayer forms for a wider range of oxygen pressures than is observed for the multilayer iron oxide structures and is very stable once formed. The FeO layer is completely inert to CO and does not change in vacuum remaining ordered and clean for days even at pressures of 1 x 10^{-9} torr. The monolayer has a distinctive structure making it easy to determine how much Fe as seen by AES corresponds to the completion of the first monolayer. Attempts were also made to

study the structure of the oxide at submonolayer coverages and these are included here. The submonolayer regime is much more difficult because the exposed iron oxide/Pt interface is a reactive surface and becomes contaminated much more easily than the fully oxidized surface. Also in this chapter, the growth above the monolayer in low pressures of oxygen, 5 x 10^{-6} torr, will also be discussed.

3.3 Results

3.3.1 Monolayer - STM

For a surface as prepared above, the STM images reveal a strikingly beautiful result (Fig. 3.1). In the 115 x 95 Å image, two periodicities are evident on the surface. The short and large periods are ~3 Å and ~26 Å respectively. The large periodicity consists of a change in the average amplitude as well as a change in the magnitude of the atomic corrugation as well. It is immediately evident from the data that the surface is three-fold symmetric and that the large periodicity is approximately eight to nine times the lattice constant of the small unit cell. This agrees well with the FeO(111) overlayer that was proposed in earlier work [10, 11].

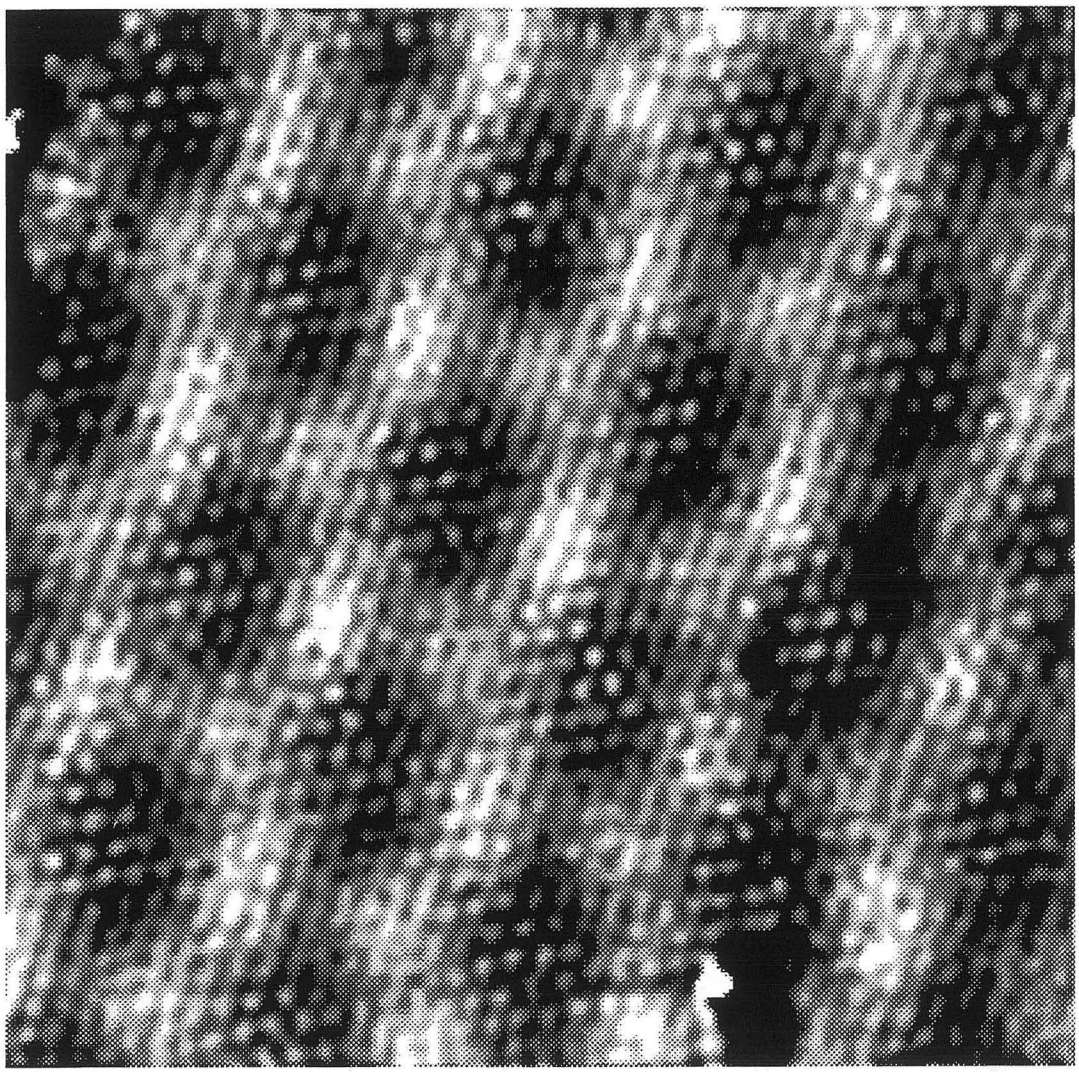

Figure 3.1 Monolayer FeO/Pt(111)

Moiré pattern structure observed for a monolayer of FeO/Pt(111). Image size is 115 x 95 Å. The short periodicity is ~3 Å and the long periodicity is ~26 Å. (I = 1.16 nA, Bias = 18 mV).

3.3.1.1 Rotational mismatch

The STM measurements have qualitatively confirmed the basic model of the surface as FeO(111)/Pt(111) with approximately parallel atomic directions. However, it is possible to make a more accurate determination of the lattice constant and of the

orientation of the overlayer with respect to the substrate. In Fig. 3.2, an image is shown with a line drawn along the atomic lattice direction. Circles drawn around the brightest maxima in consecutive unit cells do not lie along the same line. The line in Fig. 3.2 and an imaginary line through the circles are separated by an angle of 5°. This observation leads to the simple conclusion that the lattice vectors of the large and small unit cells are not aligned.

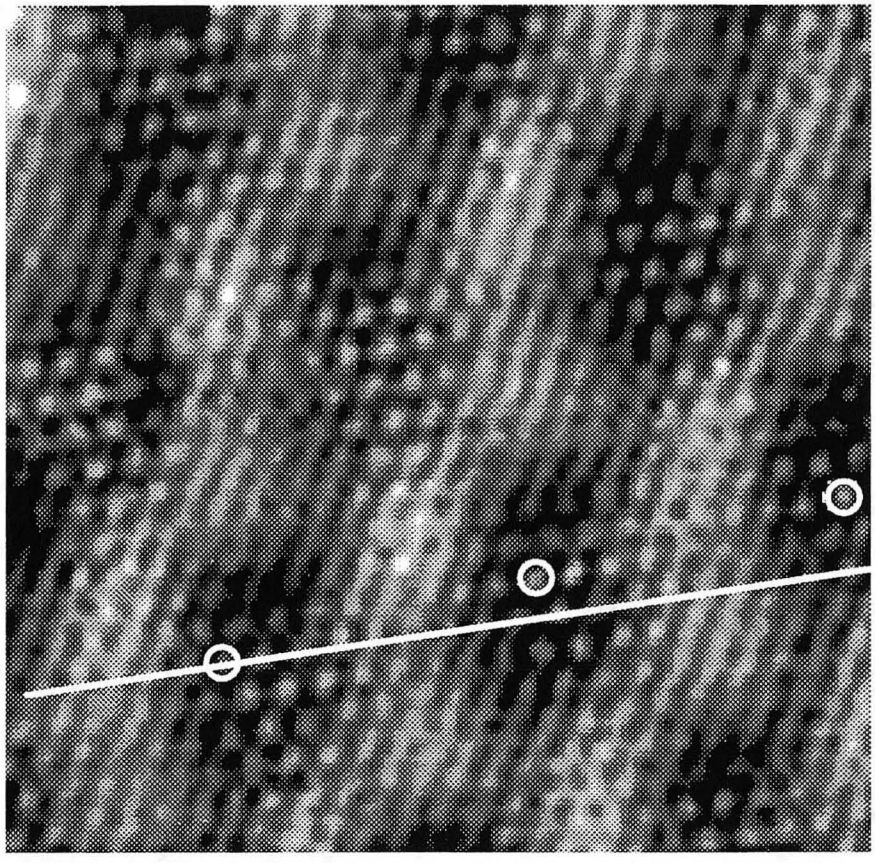

Figure 3.2 Atomic and large unit cell rotational mismatch
Circles are drawn around a prominent feature in three adjacent unit cells. The line is drawn along the atomic lattice direction. Note that the two features are not in alignment. (70 x 65 Å, I = 1.18 nA, Bias = 17 mV).

This conclusion is emphasized by filtering out the atomic periodicity. In Fig. 3.3 the image on the right has been Fourier filtered to remove the atomic lattice variations. Cursor lines drawn along the small and large unit cell directions have a 5°-6° angle between them.

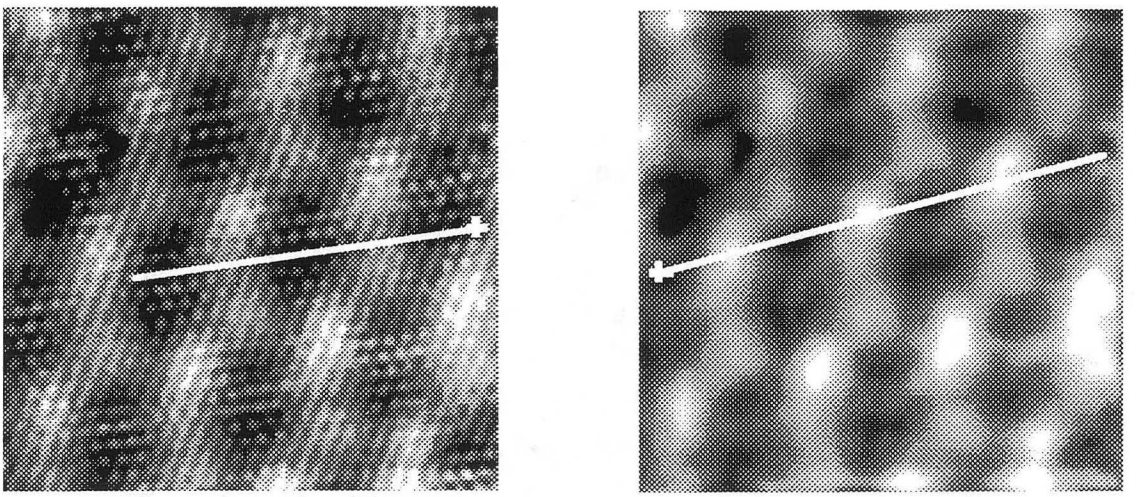

$\Theta = 7.9°$ $\Theta = 14.2°$

Figure 3.3 Atomic and large unit cell directions

For a similar image to Figure 3.2, the image on the left has a line again drawn along the atomic direction forming an angle of 7.9° with respect to horizontal. The image on the right has the short periodicity removed by filtering in Fourier space. The line drawn across the large unit cell has an angle of 14.2° with respect to the horizontal, thus giving a 6.3° rotation between the two lattices.

This effect seems subtle but large scale images such as the one in Fig. 3.4 show clearly that there is a rotational mismatch. In this image only the large periodicity is visible due to the size of the image. On adjacent terraces, two lines labeled A and B are drawn along the large unit cell directions. The lines are clearly rotated from each other by an angle of ~10°. The angle between the small and large unit cells as measured in Fig. 3.2 and 3.3 is ~5° while the angle in Fig. 3.4 is twice the angle of the large unit cell

rotation with respect to the underlying Pt, or ~10°. Since the two measured angles differ by roughly a factor of two, the FeO close packed atomic direction must be close to the Pt surface, in agreement with the LEED experiments.

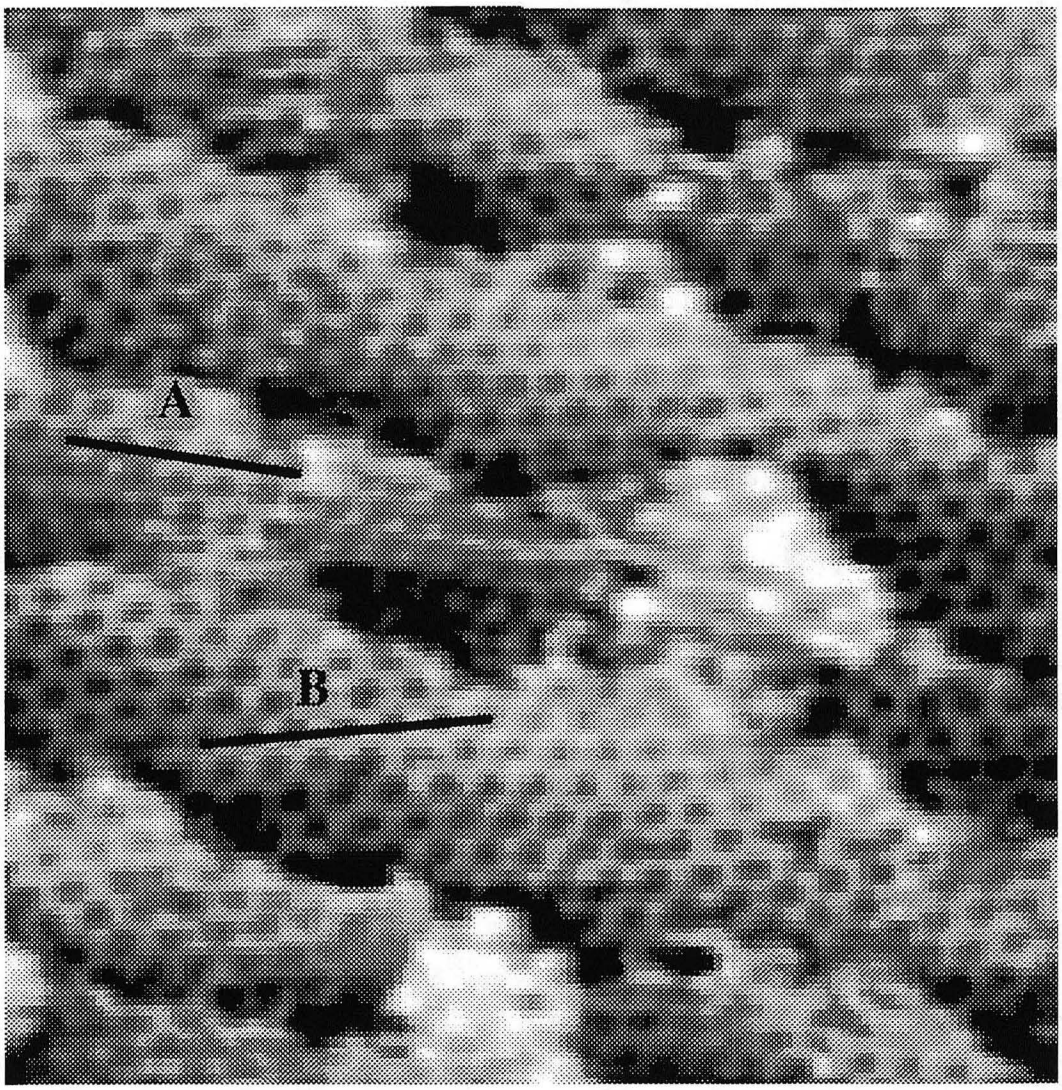

Figure 3.4 Rotational domains

In this 575 Å x 600 Å image, the two possible rotations with respect to the Pt lattice are both observed. The periodicity visible is the large periodicity due to the size of the image and two lines labeled A and B are drawn along the large unit cell direction in adjacent terraces. The angle between the lines is ~10°. (I = 1.0 nA, Bias = 464 mV).

Using the angles between the unit cells and counting the number of small unit cell distances between similar points of the large unit cell, such as those circled in Fig. 3.2, leads to a model of an FeO(111) bilayer with a very small rotation with respect to the Pt lattice constant. The model with the relevant lattice vectors and angles is shown in Fig. 3.5. The corners of the unit cell are drawn in black for emphasis. While the FeO lattice vectors are only rotated by 0.6° with respect to the Pt(111) directions, the large unit cell is rotated by 5.2° in agreement with the angles observed in Figs. 3.2-3.4. Two different domains of FeO would have a rotation of 1.2° between them which would not have been observable in the LEED experiments simply because the angle is too small compared to the size of the diffraction spots observed. It is also possible that due to the influence of steps, one domain is predominantly found on the surface. This is also suggested by the STM image in Fig. 3.4 as well as other images where mostly one domain is observed. In this case, the STM measurement has an advantage over the diffraction technique as it is more sensitive to the small rotation.

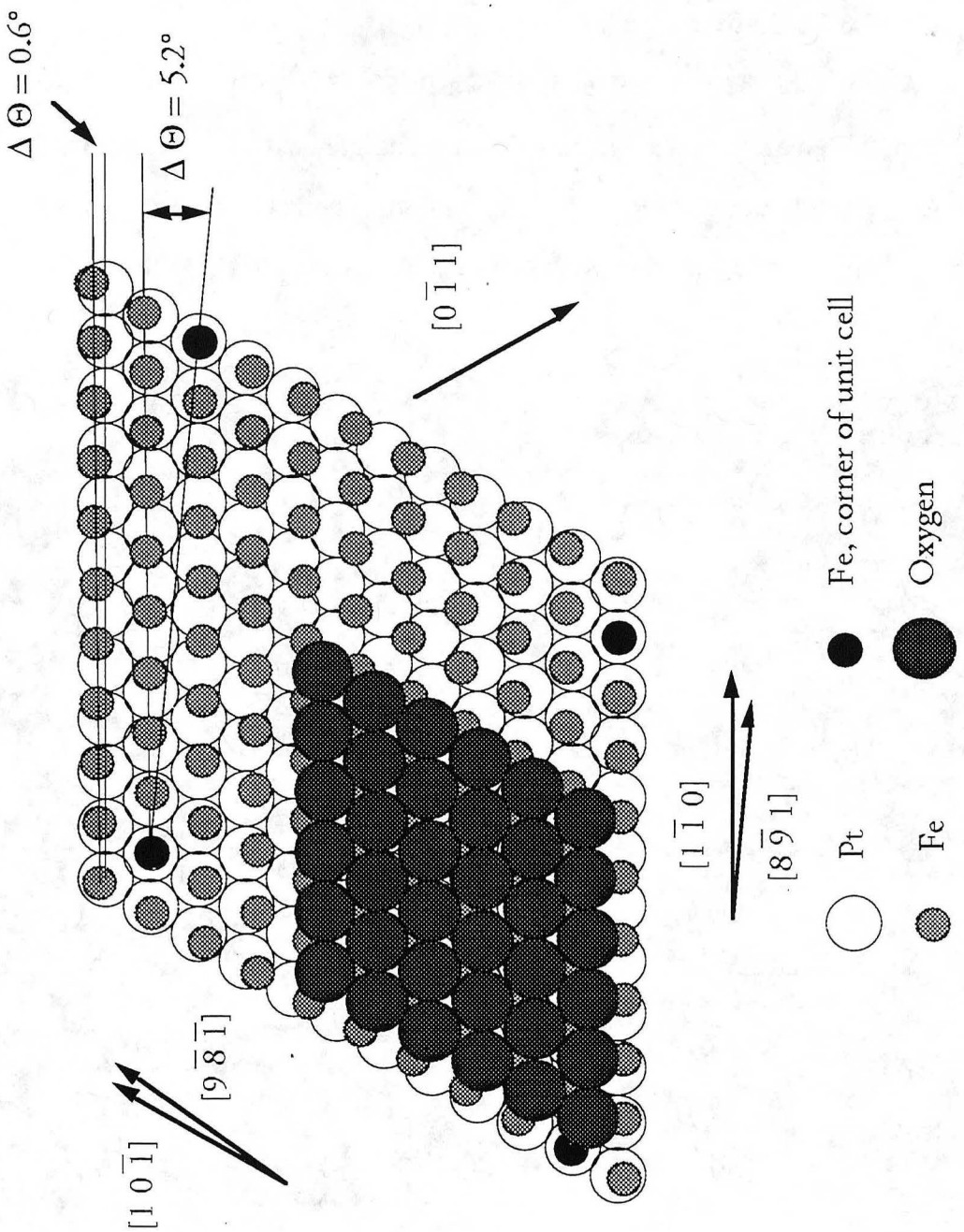

Figure 3.5 Unit cell model - FeO/Pt(111)

The unit cell model of the FeO overlayer is shown. The corner Fe atoms of the unit cell are marked in black for emphasis and only a portion of the oxygen atoms in the top layer are shown for clarity.

3.3.1.2 Lattice constant

A model of the two lattices is shown in Fig. 3.6 to illustrate how the lattice mismatch will give rise to the two periodicities measured experimentally. This type of STM image is often referred to as a Moiré pattern. The FeO will occupy a variety of sites, top, hcp, fcc, bridge, and those in between, with respect to the Pt lattice.

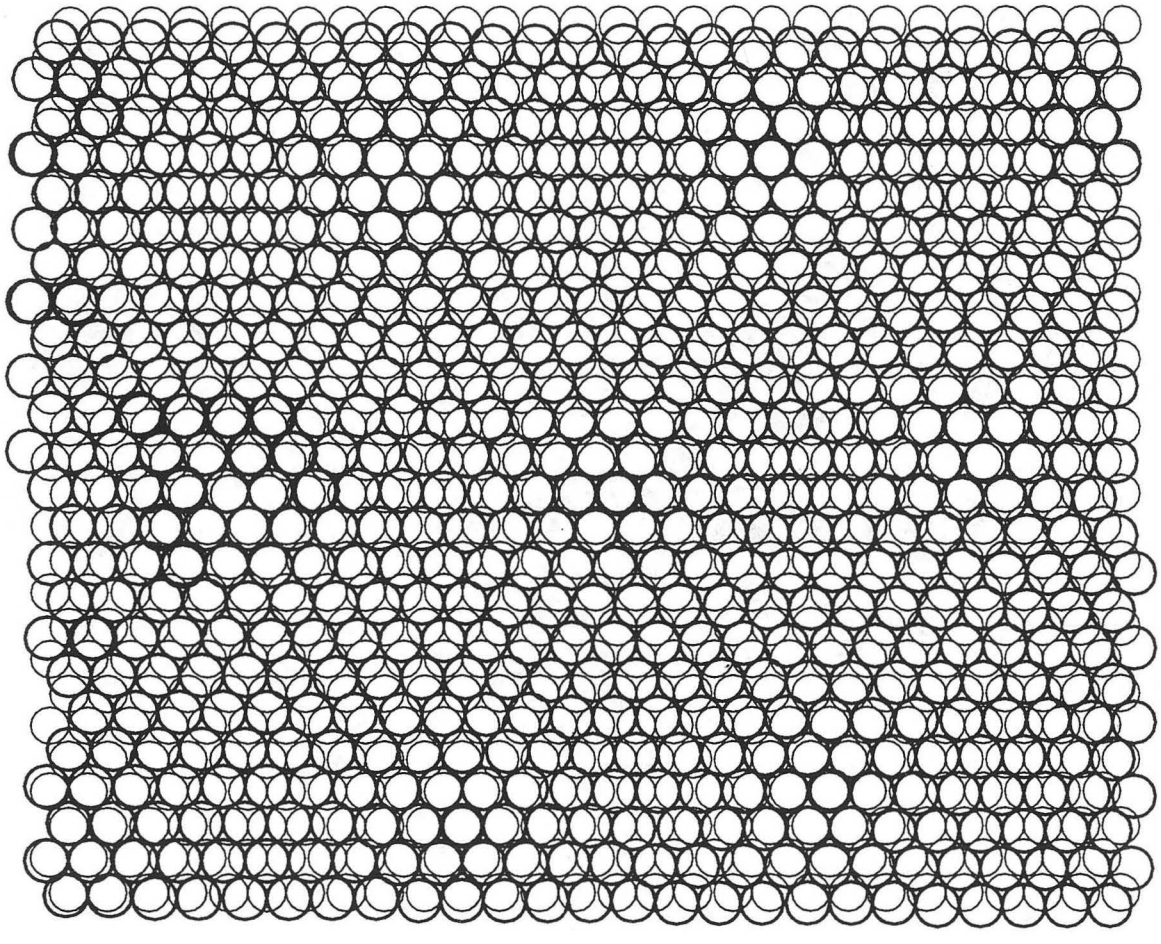

Figure 3.6 Overlayer model - Moiré pattern

Overlayer model showing the origin of the Moiré pattern due to the lattice misfit between FeO and Pt(111). The rotational mismatch between the large and small unit cells can also be seen in this figure.

The high symmetry of the structure does not allow an unambiguous determination of how these sites correspond to the image, but the large unit cell is three-fold rather than six-fold symmetric. This indicates distinct differences between the three high symmetry locations, top, fcc, and hcp, are seen in the tunneling experiment. Larger scale images may appear hexagonal (honeycombed as in Fig. 3.4) because the difference between two regions is small but it is observable in most atomic scale images. While the top and fcc would be expected to appear different as the local bonding geometry and probably the height of the overlayer vary between them, it is somewhat surprising that the difference between the hcp and fcc sites is measurable. Reasons for the difference between the hcp and fcc sites will be discussed in detail in Chapter 6.

This detailed model in Fig. 3.5 shows that two equivalent sites are connected by a displacement composed of eight lattice spacings along $[1\bar{1}0]$ and one along $[0\bar{1}1]$ in the FeO lattice and composed of nine lattice spacings along $[1\bar{1}0]$ and one along $[0\bar{1}1]$ in the Pt lattice. A simpler structure such as when n lattice constants in the FeO fit onto m lattice constants in the Pt would give a ratio between the two lattice constants as $a_{FeO}/a_{Pt} = m/n$. The observed relationship, $(8\,[1\bar{1}0] + [0\bar{1}1])a_{FeO} = (9\,[1\bar{1}0] + [0\bar{1}1])a_{Pt}$, leads to a ratio of $a_{FeO}/a_{Pt} = 9.539/8.555 = 1.115$. Since the Pt lattice constant is known to have a value of 2.77 Å, the FeO lattice constant is determined to be 3.09±0.02 Å. The low error bar is due to the fact that the next competing model, which can be ruled out by symmetry, has a very similar lattice constant. For example, an '8 fits 9' overlayer with no rotation would yield a value of 3.11 Å, but this is clearly not the case as this model would have no rotation. This measurement is not dependent on a precise calibration of the STM but rather on using a model to infer the FeO distance with respect to the platinum surface. The bulk lattice constant of FeO is 3.04 Å so the layer is slightly expanded (.05 Å) with respect to the bulk value.

Although a fairly detailed structural model is determined, several important parameters are not available from the STM results. The Fe-O and Fe-Pt bond distances

are not measured and more importantly the STM can neither confirm or refute the hypothesis that the surface is oxygen terminated. Due to the high symmetry, the various sites such as top, fcc, bridge, etc. cannot be assigned unambiguously to the image from direct interpretations of the data although the symmetry of the images indicates that the three high symmetry sites (top, fcc, and hcp) all yield different average currents.

3.3.2 X-ray photoelectron diffraction

Some of the questions left open by the STM experiment are accessible by another technique, X-ray photoelectron diffraction. The experiments described here were performed with the group of C. Fadley at LBNL [19]. Only a quick summary of the technique and results are given here [20]. The experiments consist of using an X-ray source to eject electrons from the sample. Although synchrotron radiation is often employed for XPD, an Al Kα source at 1486.7 eV was used for these experiments. As the energy of the electrons is determined by the binding energies specific to the elements in the sample, this technique is chemically specific and similar information to X-ray photoelectron spectroscopy is acquired. In addition, structural information is obtained by measuring the angular dependence of the photoelectrons using an arrangement of goniometers to rotate the sample and source with respect to the detector.

Detailed calculations considering multiple scattering of electrons are routinely used to fit data taken by XPD, but for these results, a simpler picture is adequate to understand the important results of the experiment [21]. In this model, electrons at high energies (> 500 eV) are forward focused by the other atoms. Although rigorously described by quantum mechanics, the general principle is that electrons which come closer to the atomic centers, which act as attractive potentials, are scattered through a larger angle and contribute to an increase in the intensity along the direction from the emitting to the scattering atom. This is depicted in the diagram in Fig. 3.7. For the experiment the intensity of the photoelectrons emitted at three different energy values is measured as a

function of angle. The three energy values are chosen for a binding energy of each of the three different components of the system: the Fe $2p_{3/2}$ at 777 eV, the O 1s at 956 eV, and the Pt 4f at 1414 eV. These are all at high enough energies that the forward focusing approximation applies.

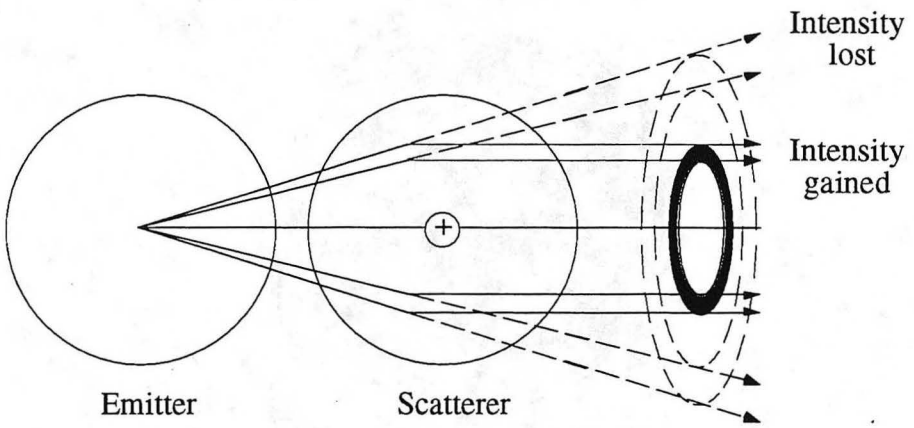

Figure 3.7 Forward focusing model - XPD

X-ray photoelectron diffraction model for forward scattering. In the semi-classical picture, the forward focusing is caused by the scattering due to the attractive potential at the atomic center creating a higher intensity along the interatomic directions.

The data are plotted in 2-D representations of the hemisphere in Fig. 3.8. The angles Θ and Φ refer to the polar and in plane angles with respect to the surface. The numbering for Θ across the bottom is for a line across the middle of the plot as indicated. The Pt 4f shows a three-fold symmetric structure that is essentially the same as the bulk Pt. This is because several layers are accessed by the technique so the structure is dominated by the bulk. The pattern does identify where the Pt $[1\bar{1}0]$ and $[11\bar{2}]$ directions are located for all three patterns as the data are acquired simultaneously. For the Fe and O diffracted intensities there is no bulk signal, so the technique is surface sensitive due to the elemental specificity. The oxygen intensity is only weakly corrugated

with a much lower anisotropy than observed for the iron (12% as compared to 50%) indicating that there are no scatterers between the oxygen and the detector. This confirms that the surface is oxygen terminated.

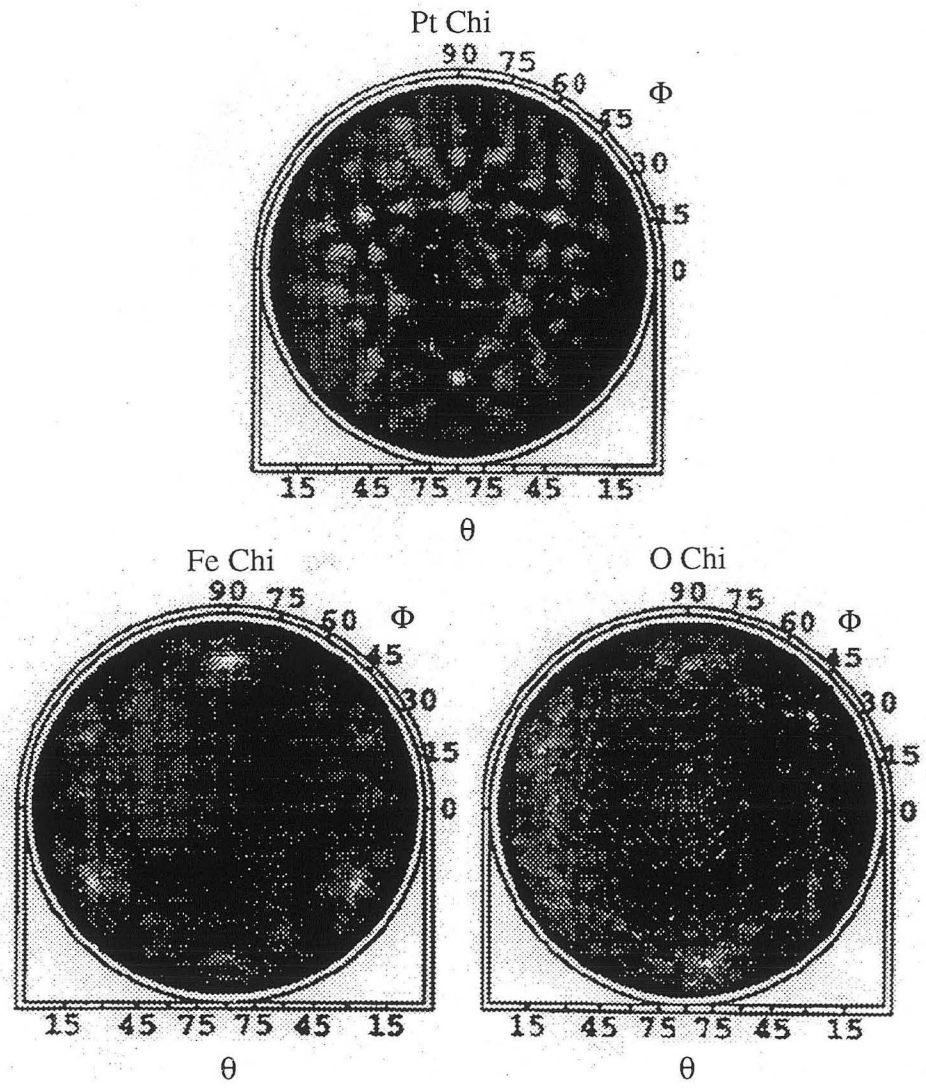

Figure 3.8 X-ray photoelectron diffraction patterns

Plots of the Pt 4f, Fe $2p_{3/2}$, and O 1s intensities are shown as polar plots. Φ is the angle in the plane of the surface and Θ is the polar angle above the surface. The Pt and Fe have strong peaks while the O is only weakly corrugated.

The Fe intensity pattern is three fold symmetric with three equivalent peaks, at Φ = 90°, 210°, and 330° at an angle Θ = 20° from the surface due to forward focusing from scatterers located between the iron and the detector. This indicates that Fe is not the terminal layer and that the local average arrangement of the iron atoms is below a trimer of atoms at the measured angle of 20° from the surface plane. More detailed simulations of the XPD data confirm this simple interpretation of the data to be valid [19]. The Fe-O bond length is determined using simple geometry to be 1.90 Å based on the 20° angle and the in surface plane spacing of 3.1 Å. This gives a perpendicular spacing between the Fe and O layers of 0.65 Å which is strongly contracted from the bulk value of 1.25 Å. The bulk bond length is 2.15 Å compared to the experimental value of 1.90 Å.

A contraction in the FeO bond length can be understood as the tendency of a polar surface to reduce its energy by lowering the dipole moment simply by flattening out the charge corrugation. This also agrees with the expansion in the lateral lattice constant as simply being due to keeping the unit cell volume closer to the bulk value. However, the magnitude of the change is still quite large. As the Pt intensity is dominated by bulk effects, no information is available from this experiment regarding the Fe-Pt bond. In addition there are two possible stackings of the O layer with respect to the second layer of Pt and the XPD is consistent with the majority of the surface containing only one stacking suggesting that there is a small energy difference between the two. As this involves the second layer of platinum or the fourth layer from the surface it is not expected to be detectable using STM. It is somewhat difficult to visualize the stacking differences but one way to understand the difference is that for the dominant stacking as observed by XPD the top sites have a stacking of ABC/CA and the two hollows are ABC/AB and ABC/BC while for the stacking that is not favored the stacking is ABC/CB for the top and ABC/AC and ABC/BA for the two different hollows. The notation used is starting from the 3rd layer of Pt and working towards the oxygen layer with the interface indicated by the slash mark. The stacking of the FeO layer will also be discussed further in Chapter 6.

3.3.3 Submonolayer coverages

In the submonolayer regime there is much greater difficulty in obtaining clean surfaces and atomic resolution on the islands of submonolayer iron oxide was not achieved. LEED shows the existence of the FeO(111) pattern well before the completion of the monolayer (.75 ML) but no other atomic structure evidence is available at this time. In Fig. 3.9, an image of the submonolayer coverage is shown at the top. Small islands with a lateral size of 10-20 Å and a height of 1.2 Å are seen on the surfaces for a coverage of 0.2-0.5 ML. The size of the islands is quite consistent. One possible explanation is that the center of the island nucleated in the lowest energy site and that as the island gets larger, it is forced to occupy less and less favorable sites due to the lattice mismatch. The site mismatch is changed by 10% at the nearest neighbor and already by 20% at the second nearest neighbor site as is illustrated in Fig. 3.10. This situation can be changed as is shown by heating the surface for a longer period of time, as depicted in the lower image of Fig.3.9. Now the iron oxide is nucleated at the step edges as demonstrated by the cross sectional height profiles shown in Fig. 3.9.

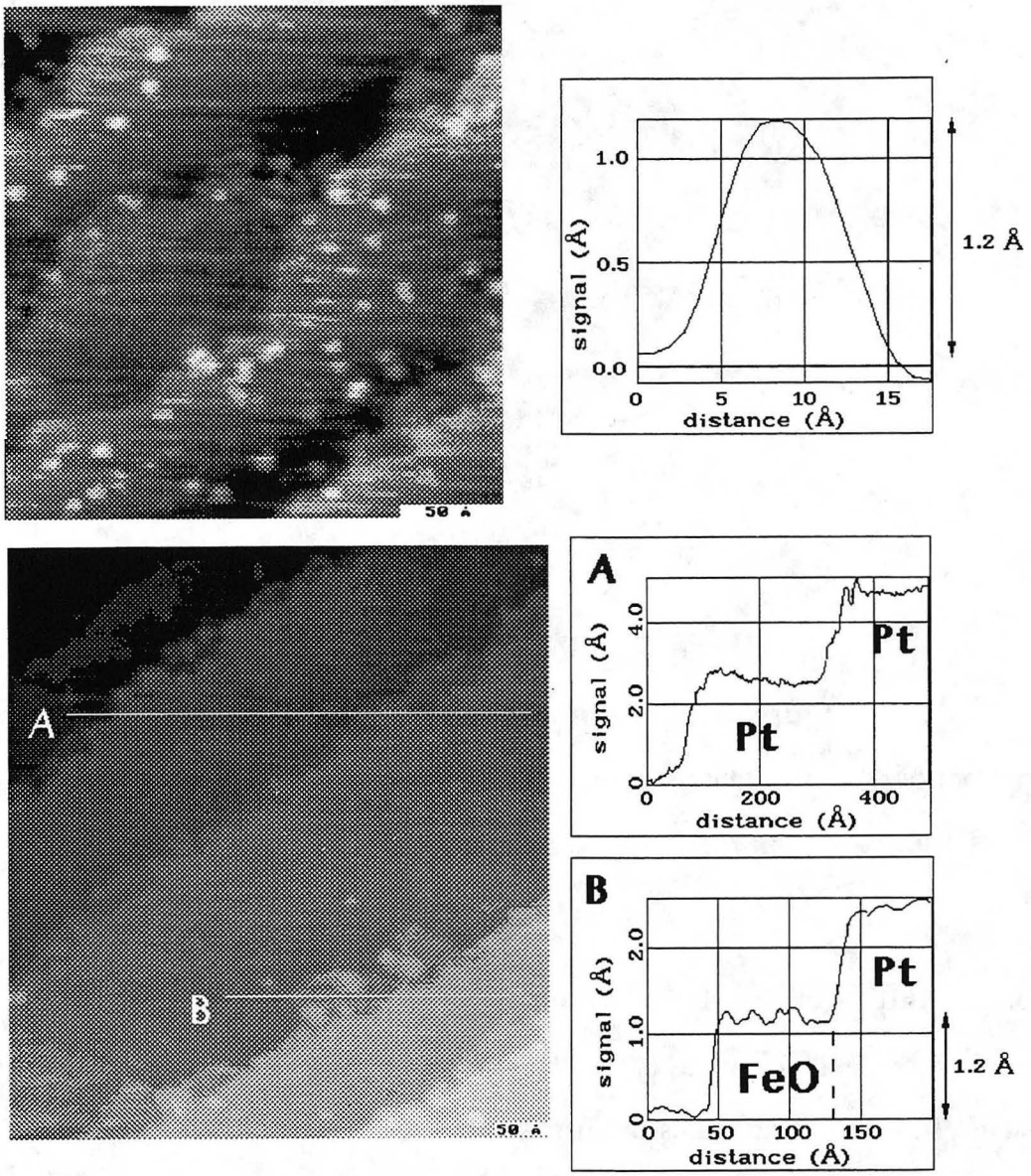

Figure 3.9 Submonolayer growth of FeO

In the upper image (250 Å x250 Å), small islands have nucleated on the terrace. A cursor plot shows the size of one of the islands. In the lower image (500 x 550 Å), the islands have nucleated along the step edge with the same apparent height as in the upper image as shown in the cursor plot. The Pt step height is 2.3 Å. (Upper: I = 0.9 nA, Bias = -52 mV, lower: I = 0.4 nA, Bias = -44 mV).

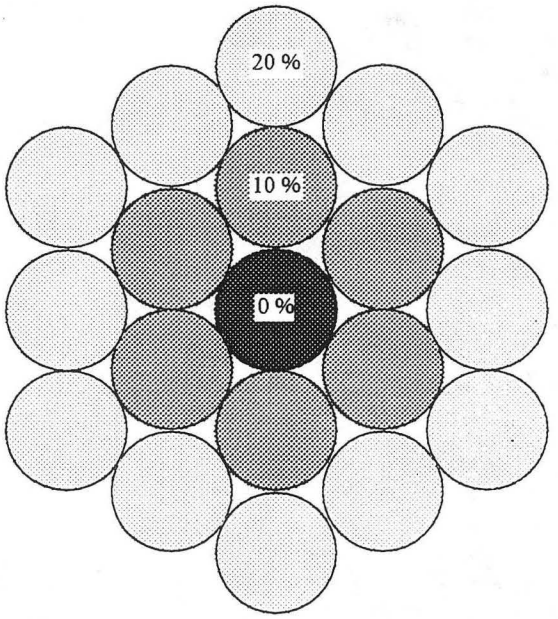

Figure 3.10 Submonolayer island model

Model of how the misfit would increase with distance away from the center of a small island.

3.3.4 Multilayer growth - disordered

Iron oxide at coverages above the monolayer shows a dependence on oxygen pressure. The ordered structures will be discussed in Chapter 4 but the structures grown at oxygen pressures of 5 x 10^{-6} torr are presented here. At this pressure of O_2 and at coverages of > 1 ML, the monolayer FeO structure covers most of the surface. However, multilayer islands are also observed. Atomic resolution images indicate that the islands do not have a very regular structure.

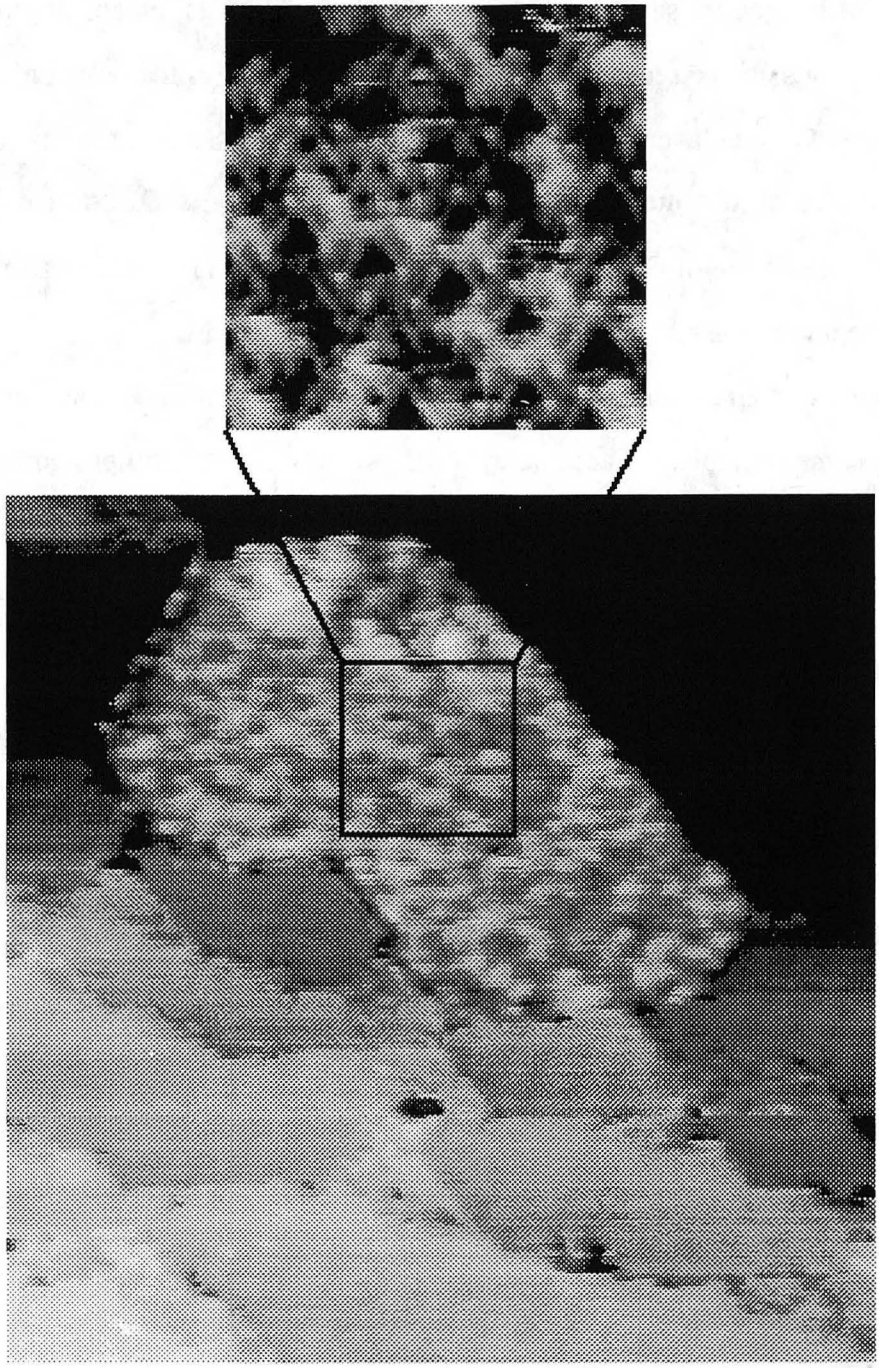

Figure 3.11 Disordered multilayer growth

A multilayer island on terraces covered by the FeO monolayer structure. In the inset image, a series of triangular pits are observed that have the periodicity of the underlying monolayer. (500 x 500 Å, Inset: 100 x 100 Å, I = 1.0 nA, Bias = 0.47 V).

STM images are shown in Fig. 3.11. In the small inset image, an ordered array of triangular pits can be seen that have the same periodicity as the large unit cell of the underlying FeO monolayer (~ 26 Å). These images show some similarity to the more well ordered result obtained by Condon, et al [9] for an α-Fe_2O_3 surface which was attributed to a mixture of FeO and Fe_2O_3 islands. In Fig. 3.11, different structures also appear to be nucleating at various parts of the monolayer unit cell.

This is an illustrative example of why epitaxy in metal oxide/metal systems quickly becomes complex. The first layer forms in a reduced form providing complete wetting of the substrate. However, the large mismatch that is usually present leads to a 'corrugated' surface. Additional layers cannot continue to form with the same structure as the monolayer because it is not an equilibrium structure when there is no metal surface to provide the additional coordination. Although the wetting is complete, the large mismatch has led to a surface that is considerably rougher than the original metal surface.

3.4 Summary and conclusions

By using STM in combination with XPD and LEED information, the initial states of the growth of FeO on Pt(111) can be investigated in detail. The first layer of iron oxide grows as an FeO(111) bilayer of iron and oxygen. The surface is oxygen terminated and the atomic directions are rotated by 0.6° with respect to the Pt(111) directions. The lateral lattice constant is slightly expanded from the bulk value of 3.04 Å to 3.09 Å and the Fe-O bond length is strongly contracted from 2.15 Å in the bulk to 1.90 Å. For comparison, the Fe-O bond lengths in α-Fe_2O_3 are 1.91 and 2.06 Å [22]. Although the Fe-Pt bond distance and the amount of buckling in the overlayer have not been determined experimentally, the surface is determined more quantitatively than other similar metal oxide interfaces.

At coverages below the monolayer, the lattice mismatch results in small islands nucleated on the terrace and at higher coverages the disordered growth is also strongly

influenced by the lattice mismatch showing various structures nucleating at different parts of the unit cell. These results indicate that there is strong intralayer bonding in the iron oxide overlayer which leads to the oxide essentially retaining its lateral structure rather than adapting to the bulk value and is also implied by the strong contraction of the FeO bond at the surface. This lattice mismatch then strongly influences the epitaxial growth of the iron oxide overlayer.

Chapter 3 References

[1] R. Wiesendanger, I.V. Shvets, D. Bürgler, G. Tarrach, H.-J. Güntherodt, J.M.D. Coey and S. Gräser, Science **255,** (1992) 583.

[2] R. Wiesendanger, I.V. Shvets, D. Bürgler, G. Tarrach, H.-J. Güntherodt and J.M.D. Coey, Europhysics Letters **19,** 2 (1992) 141.

[3] H.K. Bowen, D. Adler and B.H. Auker, Journal of Solid State Chemistry **12,** (1975) 355.

[4] G. Tarrach, D. Bürgler, T. Schaub, R. Wiesendanger and H.-J. Güntherodt, Surf. Sci. **285,** (1993) 1.

[5] N.G. Condon, P.W. Murray, F.M. Leibsle, G. Thornton, A.R. Lennie and D.J. Vaughan, Surf. Sci. **310,** (1994) L609.

[6] R.J. Lad and V.E. Henrich, Surf. Sci. **193,** (1988) 81.

[7] R.L. Kurtz and V.E. Henrich, Surf. Sci. **129,** (1983) 345.

[8] A. Barbieri, W. Weiss, M.A. Van Hove and G.A. Somorjai, Surf. Sci. **302,** (1994) 259.

[9] N.G. Condon, F.M. Leibsle, A.R. Lennie, P.W. Murray, D.J. Vaughan and G. Thornton, Phys. Rev. Lett. **75,** 10 (1995) 1961.

[10] G.H. Vurens, M. Salmeron and G.A. Somorjai, Surf. Sci. **201,** (1988) 129.

[11] G.H. Vurens, V. Maurice, M. Salmeron and G.A. Somorjai, Surf. Sci. **268,** 1-3 (1992) 170.

[12] C.F. Brucker and T.N. Rhodin, Surf. Sci. **57,** (1976) 523.

[13] S.E. Greco, J.P. Roux and J.M. Blakely, Surf. Sci. **120,** (1982) 203.

[14] K. Kishi, Surf. Sci. **192,** (1987) 210.

[15] S. Masuda, Y. Harada, H. Kato, K. Yagi, T. Komeda, T. Miyano, M. Onchi and Y. Sakisaka, Phys. Rev. B **37,** 14 (1988) 8088.

[16] G.W. Simmons and D.J. Dwyer, Surf. Sci. **48,** (1975) 373.

[17] V.S. Smentkowski and J.T. Yates Jr., Surf. Sci. **232,** (1990) 113.

[18] P. Watson, M.A. Van Hove and K. Hermann, *Atlas of Surface Structures: Volume 1A* , (American Chemical Society and American Insititue of Physics for the National Institute of Standards and Technology, New York, 1994).

[19] Y.J. Kim, C. Westphal, R.X. Ynzunza, H. Xiao, Z. Wang, H.C. Galloway, M. Salmeron, M.A.V. Hove and C.S. Fadley, in preparation (1995)

[20] C.S. Fadley, The Study of Surface Structures by Photoelectron Diffraction and Auger Electron Diffraction in *Synchrotron Radiation Research: Advances in Surface and Interface Science* (Plenum Press, New York, 1992)

[21] J. W.F. Egelhoff, X-Ray Photoelectron and Auger Electron Forward Scattering: A Structuraly Diagnostic for Epitaxial Thin Films in *Ultrathin Magnetic Structures I: An Introduction to Electronic, Magnetic, and Structural Properties* (Springer-Verlag, Berlin, 1994)

[22] R.G. Wyckoff, *Crystal Structures*, (Interscience Publishers, New York, 1963).

Chapter 4 Multilayer Iron Oxide on Pt(111)

4.1 Introduction

Besides the monolayer structure observed in Chapter 3, other ordered structures are also observed in the iron oxide/Pt(111) system. As was briefly mentioned previously, iron oxide has several forms. However, on the Pt(111) surface only three fold symmetric structures are observed so it is appropriate to consider only the planes of the three most common forms of the oxide that have the correct symmetry. From this point of view, all the iron oxides consist of nearly close packed planes of oxygen with varying amounts of Fe cations in between the planes [1]. Three models are depicted in Fig. 4.1.

The first is the simple FeO structure which has been discussed previously where the Fe cations are in a 1x1 arrangement with respect to the oxygen atoms. The Fe_3O_4 structure has both octahedrally and tetrahedrally coordinated Fe atoms. Since the Fe atoms are inequivalent it is possible to choose different terminations that would contain only one type of atom. Both are shown in the drawing. The unit cell is 2x2 with respect to the oxygen atoms and therefore also with respect to the FeO layer. For the α-Fe_2O_3 structure all the cations are octahedrally coordinated and the unit cell is $\sqrt{3}x\sqrt{3}R30°$ with respect to the oxygen atoms. The structures of the crystal are made up of a cubic stacking of the oxygen planes (ABCABC) for FeO and Fe_3O_4 while the stacking is (ABAB) for α-Fe_2O_3. The O-O in plane spacing for the three bulk structures are 2.90 Å for α-Fe_2O_3, 2.97 Å for Fe_3O_4, and 3.04 Å for FeO [2].

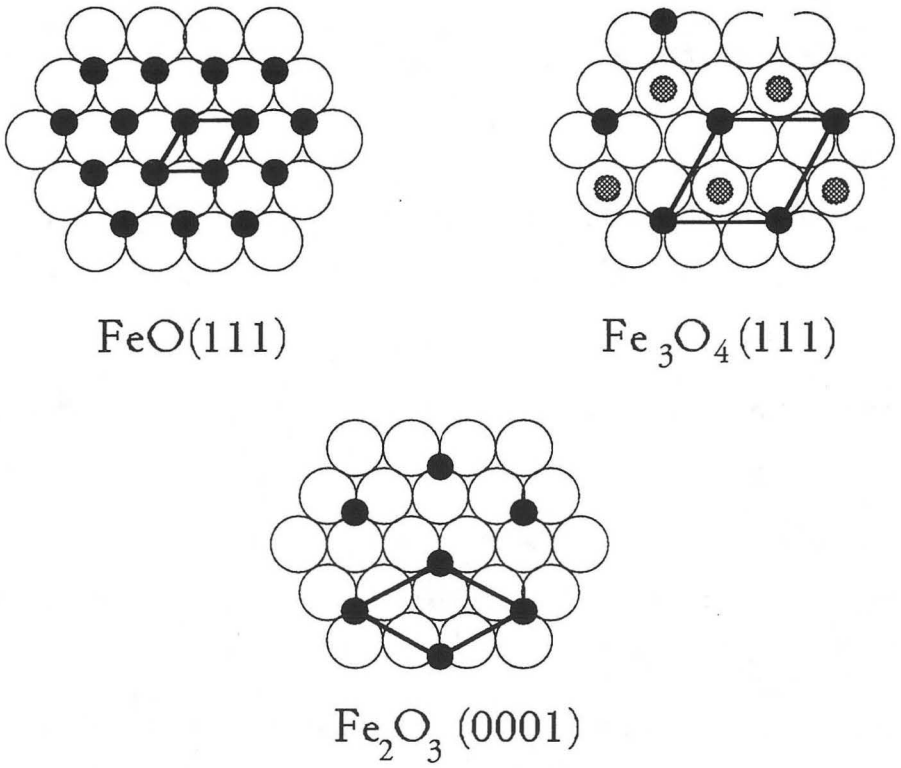

Figure 4.1 Iron oxide unit cell structures

Models of the three fold symmetric iron oxide structures are depicted with the close packed oxygen atoms as the large open circles. The octahedrally coordinated iron are the small filled circles and the hashed circles in the Fe_3O_4 cell are the tetrahedrally coordinated iron atoms.

For very thin films grown in UHV, different equilibrium structures may form due to the considerable influence of the substrate. However, as these films grow to thicker layers an increasing tendency to conform to bulk iron oxide structures might be expected. For this purpose, the bulk phase diagram is reproduced in Fig. 4.2. As has been stated previously, bulk FeO is not stable at room temperature. For the conditions used to prepare the iron oxide films, typically 750 C and oxygen pressures in the 10^{-4}-10^{-}

^{7} torr ranges, the stable bulk phase is changing from α-Fe_2O_3 at the higher oxygen pressures to

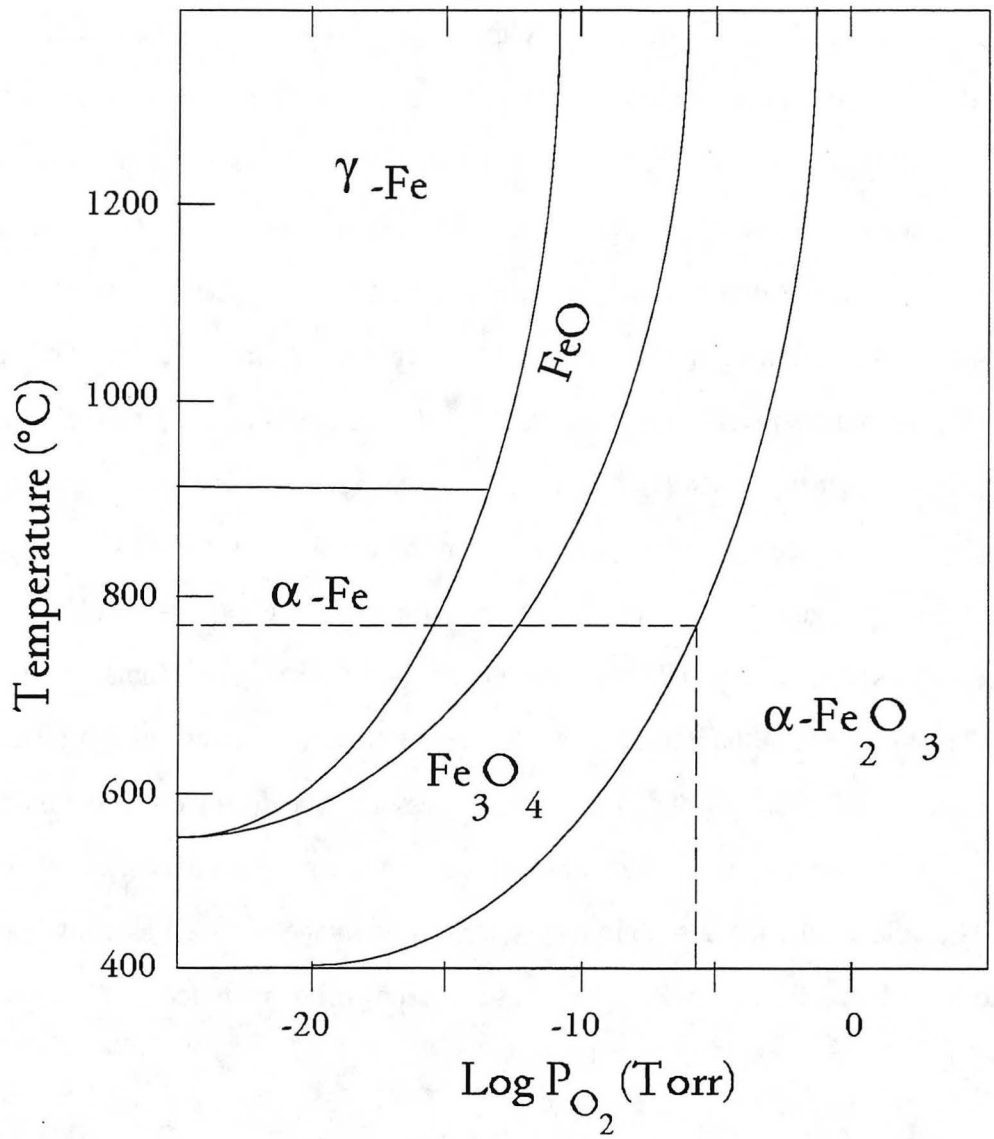

Figure 4.2 Iron oxide phase diagram

The bulk phase diagram for iron oxide is reproduced from [1]. FeO is not stable at room temperature for any oxygen pressure or at the conditions used to grow the oxide, 750 C and 10^{-4} to 10^{-7} torr oxygen. These are conditions where either α-Fe_2O_3 or Fe_3O_4 are the stable bulk phases.

Fe_3O_4 at the lower oxygen pressures. It has already been demonstrated that FeO is the most stable form of the oxide at the Pt interface for oxidation pressures of 10^{-4}-10^{-7} torr and 750 C. However, as the amount of iron oxide on the surface is increased other forms of the oxide are observed as predicted by the phase diagram. The ordered structures observed at coverages above the monolayer will be the focus of this chapter.

It is well known in the field of scanning tunneling microscopy that spontaneous changes in the tip structure can cause large effects in the appearance of the resulting images. In the case of tunneling into a metal oxide overlayer, spontaneous tip changes that result in large changes in the image contrast are very common and produce some seemingly anomalous results. Discussion of this type of result will be included as it is important to further the investigations of metal oxide surfaces using scanning tunneling microscopy. Although the existence of a gap in the density of states might also cause considerable changes in the image contrast with bias changes, as is observed on semiconductors, that has typically not been observed for the iron oxide films.

Thicker layers of the iron oxide are formed by first evaporating enough Fe to form one monolayer and oxidizing at a given oxygen pressure. The dosing of Fe and oxidizing step are repeated with no more than a monolayer equivalent being deposited at any one time. This allows the different amounts of iron to be imaged as well as allowing each layer to be fully oxidized. The oxygen pressures used will be included with the relevant section.

4.2 Fe_3O_4 - 2x2

For oxygen pressures of 10^{-5} torr and the preparation method detailed above, a structure with a 2x2 periodicity is observed. This structure is consistent with the $Fe_3O_4(111)$ surface. It is not found to coexist with the FeO monolayer for any of our experiments. The differences between 2x2 and $\sqrt{3}x\sqrt{3}R30°$ structures would be an angle of 30° and a change in the lattice constant of ~0.9 Å. Even without observing these

structures simultaneously with the FeO lattice, they are distinguishable from each other. The lattice constant difference would be difficult to detect unambiguously as it is close to the typical errors from piezo calibration problems. However, the difference in the angle is quite large. The atomically resolved images consist typically of symmetric maxima with a number of point defects as is shown in Fig. 4.3.

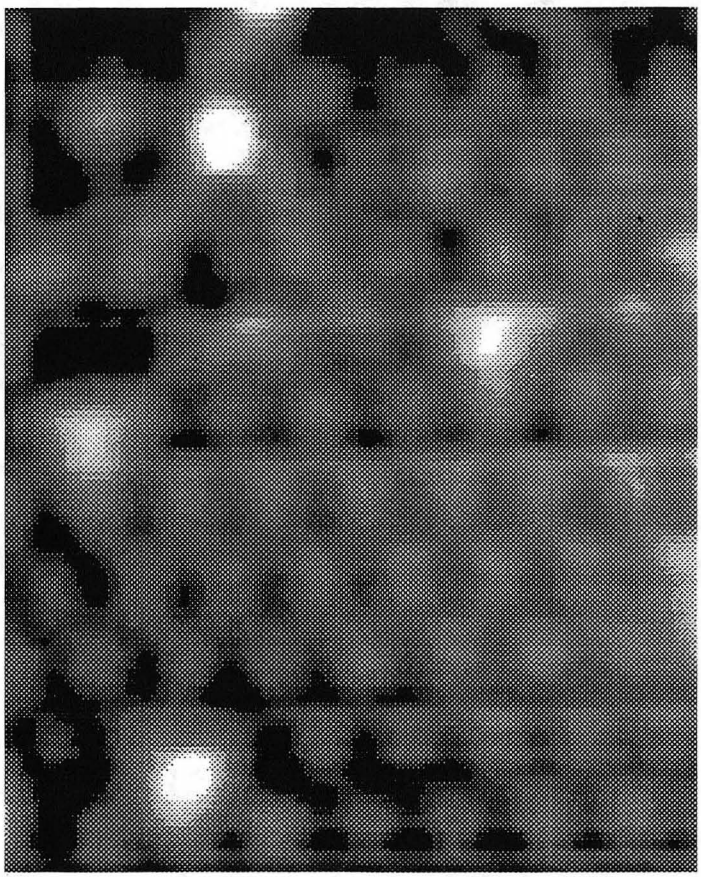

Figure 4.3 Fe_3O_4(111) atomic scale image

An atomically resolved 47 x 58 Å image of an Fe_3O_4(111) termination. Three point defects appear as bright spots centered between three maxima while the structure of the defect in the upper corner is more complicated. (I = 1 nA, Bias = -0.80 V)

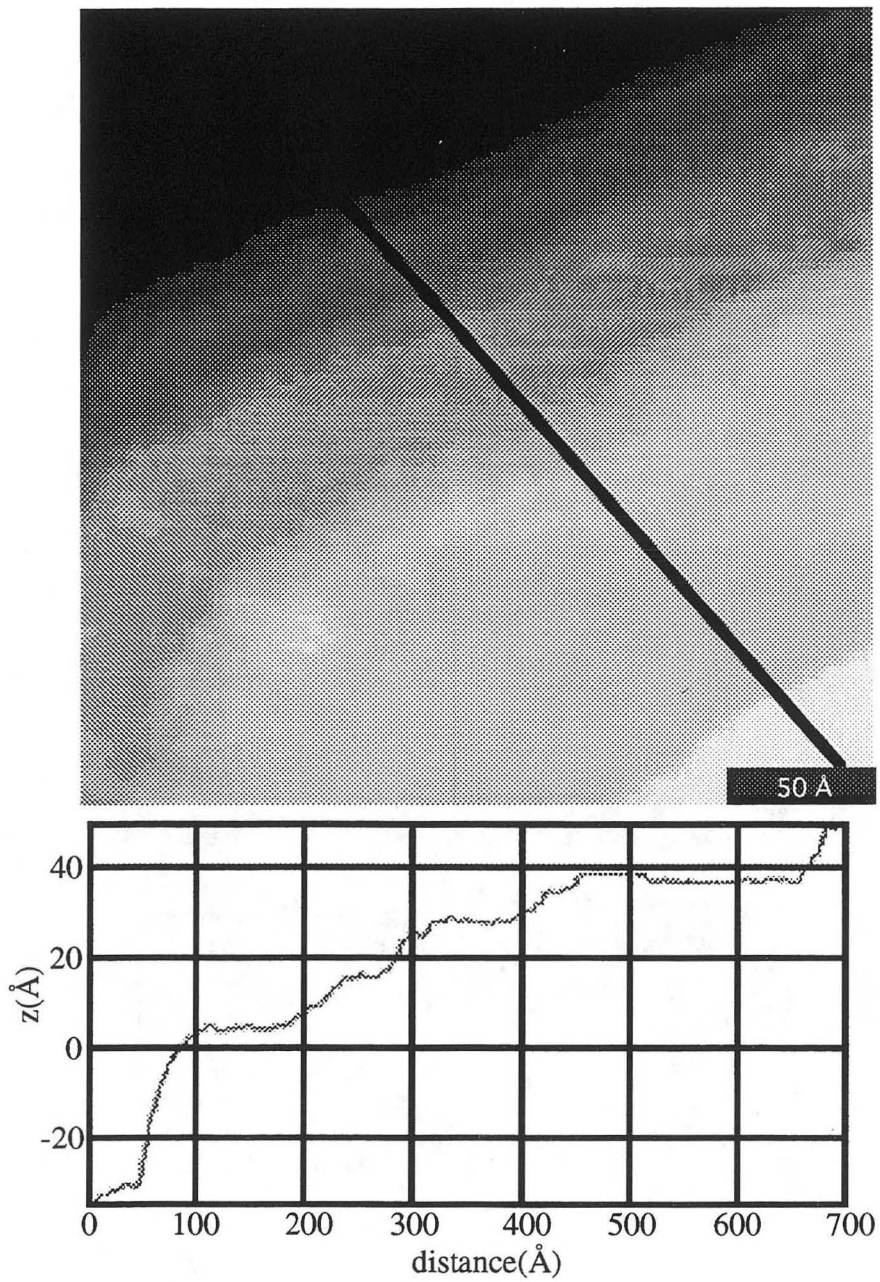

Figure 4.4 Fe_3O_4(111) large scale image

A large scale image of the Fe_3O_4(111) surface with a cursor profile. Although the steps are approximately parallel they are not monoatomic heights.

On a larger scale, multiple step heights are observed although the steps still retain the approximately parallel arrangement that is common on the clean single crystal as is shown in Fig. 4.4 (preceding page). This indicates a growth mode that is somewhat in between layer by layer and 3-D since only a moderate amount of surface roughening is seen.

By far the most noticeable feature of the surface is that the atomically resolved images have a large number of defects. Often so many are observed that the surface appears disordered and the image in Fig. 4.3 is actually in a region where the concentration of defects is low enough that the underlying structure is visible. Two detailed diffraction experiments have identified an $Fe_3O_4(111)$ structure for this system. One set of studies using a tensor LEED analysis [3, 4] found a best fit for a structure terminating in a 1/4 ML of Fe atoms while an XPD study found the fit to be better without the additional Fe atoms [5]. The STM images suggest as a possible cause for this discrepancy that the surface is prone to have large numbers of point defects possibly including additional Fe atoms. This would be extremely dependent on the precise stoichiometry of the surface and the exact preparation conditions and is likely to vary from study to study.

4.3 α-Fe_2O_3 - $\sqrt{3}x\sqrt{3}R30°$

At higher oxygen pressures of 10^{-4} torr, islands of a second form of iron oxide are observed to coexist with the FeO monolayer structure. In Fig. 4.5 an image is shown where the atomic periodicity is visible on the islands. After a sudden tip change occurs, in the last one third of the image, the large periodicity of the monolayer also becomes visible. The step edge appears as alternating bright and dark bands because the color table has been adjusted so that it is the same on all terraces. The location of the tip change is indicated in the image. The unit cell is $\sqrt{3}x\sqrt{3}R30°$ with respect to the FeO monolayer as determined from images where both structures are resolved. This structure is assigned to an α-$Fe_2O_3(0001)$ surface. The angle between unit cells in both structures measures

27°± 3°, but it is also necessary to take into account that the large unit cell of the FeO layer is rotated ± 5° from the close packed atomic directions. An image of the atomic structure is shown in Fig. 4.6.

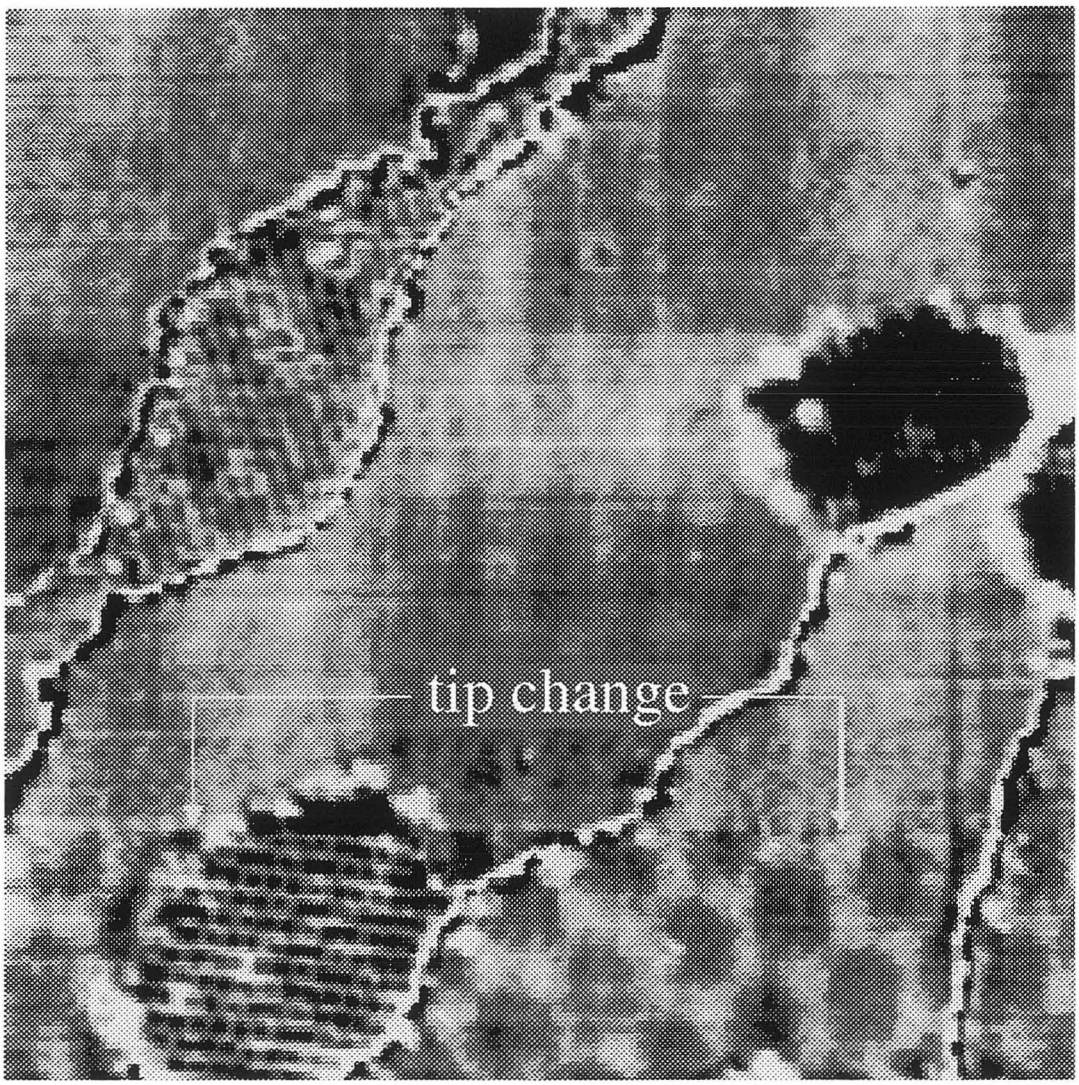

Figure 4.5 FeO(111) with α-Fe_2O_3 islands

Constant current image of 1.3 ML coverage. (300 x 300 Å) Islands with a $\sqrt{3}x\sqrt{3}R30°$ periodicity are located at step edges and after the uncontrolled tip change marked in the image, the large periodicity of the monolayer FeO is also visible. (I = 1.0 nA, Bias = -163 mV).

Unfortunately, most images show either resolution of the atomic periodicity on the $\sqrt{3}x\sqrt{3}R30°$ islands or resolution of the large periodicity of the large unit cell in the FeO monolayer but not both. (The atomic periodicity of the FeO would be expected to be more difficult to see simply because it is smaller than the $\sqrt{3}x\sqrt{3}R30°$ periodicity, but this is not true for the large unit cell of the FeO monolayer.)

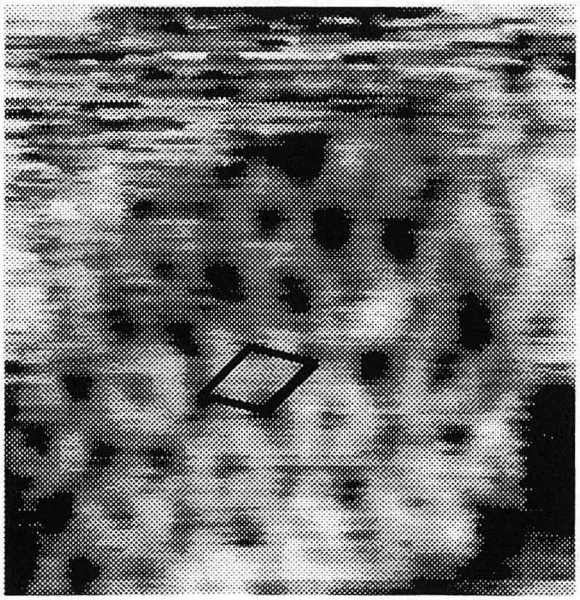

Figure 4.6 Atomic resolution - α-Fe_2O_3 island

In this 40 x 40 Å image, the atomic periodicity of the α-Fe_2O_3 island is visible. The unit cell of the α-Fe_2O_3 is indicated in black. (I = 1.0 nA, Bias = -163 mV)

4.3.1 Contrast reversal

A surprising tip effect is also observed where the two oxides coexist in the 1-2 ML range. In some images the α-Fe_2O_3 islands appear higher than the surrounding FeO terrace and in other images the islands appear lower. This change is not induced by changing the bias or other tunneling gap conditions but occurs spontaneously. In Fig. 4.7 an image is shown where the change occurs during acquisition of an image, inverting

the contrast in the middle of an island. Although the structures are not resolved in this image, subsequent images confirm that the FeO structure covers the terrace and the α-Fe_2O_3 structure covers the islands.

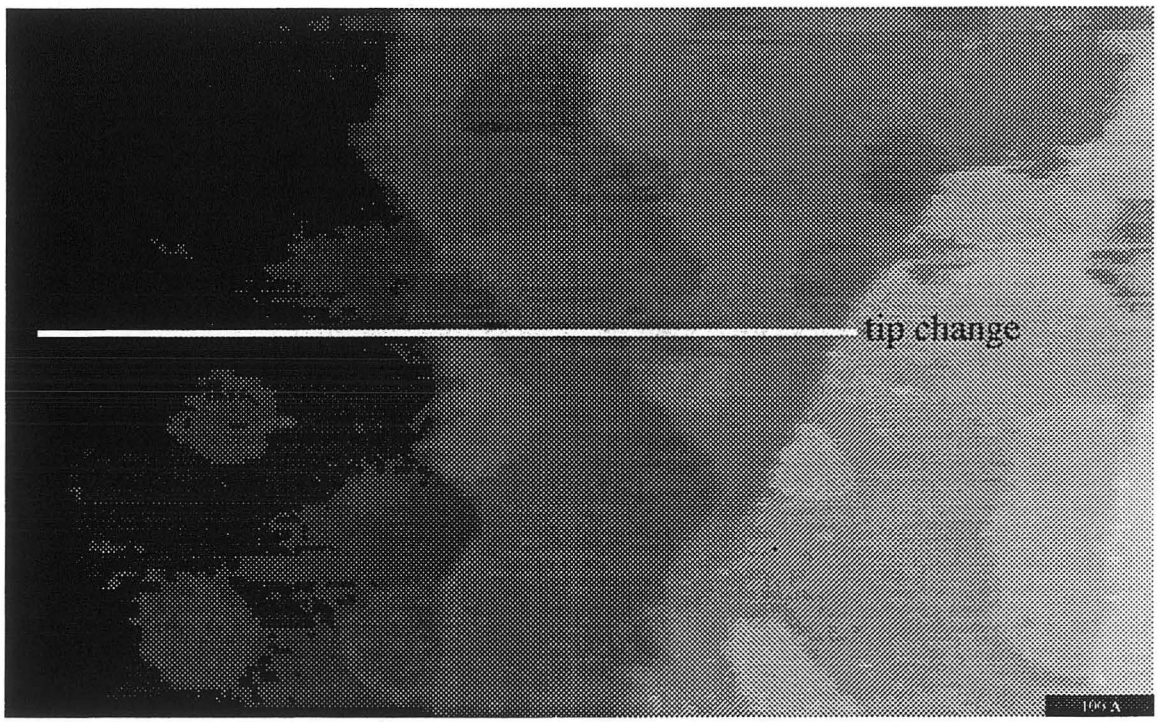

Figure 4.7 Contrast reversal - α-Fe_2O_3/FeO(111)

In the upper portion of the 1100 Å x 670 Å image islands occur that appear lower than the surrounding terrace but after a sudden tip change the islands now appear higher than the surrounding terrace. The islands have a $\sqrt{3}x\sqrt{3}R30°$ periodicity with respect to the FeO atomic periodicity.

Attempts to control the tip changes by cleaning the tip using voltage pulses or imaging in an oxygen environment to keep the tip oxidized were not successful as the changes still seemed to occur randomly for all conditions tried. One possible explanation is that a change in the tip termination or structure shifts the relative tunneling probability for tunneling into the two types of iron oxide. Since electronic and topographic effects

are coupled in the STM, it is not possible to extract the actual topography from the images. The apparent island height as measured in the STM images ranges from a value of +4 Å to -4 Å. This is a fairly large change to explain simply by electronic changes in the tip. Typical changes for other calculations where the tip is changed only cause changes of 2-3 Å at most [6, 7].

Another possibility is that for all tip terminations, the α-Fe_2O_3 islands are less conductive and that the height measured is always lower than the actual topography. It is even possible that the islands are not conductive enough to allow vacuum tunneling and therefore the tip is actually being forced into contact with the surface of the islands. If the tip or surface is covered by a passivating layer and thus chemical bonds are not formed, this type of contact could remain within the elastic regime. However, scanning in contact or at very small distances would probably enhance the possibility of damaging the tip leading to a larger number of tip changes. (Attempts to collect I-V spectra were also hampered by the numerous tip changes.) While no further experimental evidence exists, the conclusion that the α-Fe_2O_3 layer is becoming too thick to tunnel through is supported by the calculations on the FeO layer presented in Chapter 6 which show that the tip sample distance is already very small (~5 Å for a 20 MΩ gap) for that case.

4.3.2 Large periodicity α-Fe_2O_3

As more Fe is added to the surface and oxidized, some larger islands of α-Fe_2O_3 are formed along with higher crystallites. The islands continue to have the same $\sqrt{3}x\sqrt{3}R30°$ periodicity and in addition a Moiré pattern is observed when the islands become large enough. This second large unit cell has a 43 ± 4 Å periodicity. Both large unit cells have very similar angular orientations and are seen to coexist as is shown in Fig. 4.8. The respective unit cells are drawn on the image and the step edge appears as a band of alternating bright and dark as the color scale has been adjusted so that the contrast on both terraces would be approximately the same.

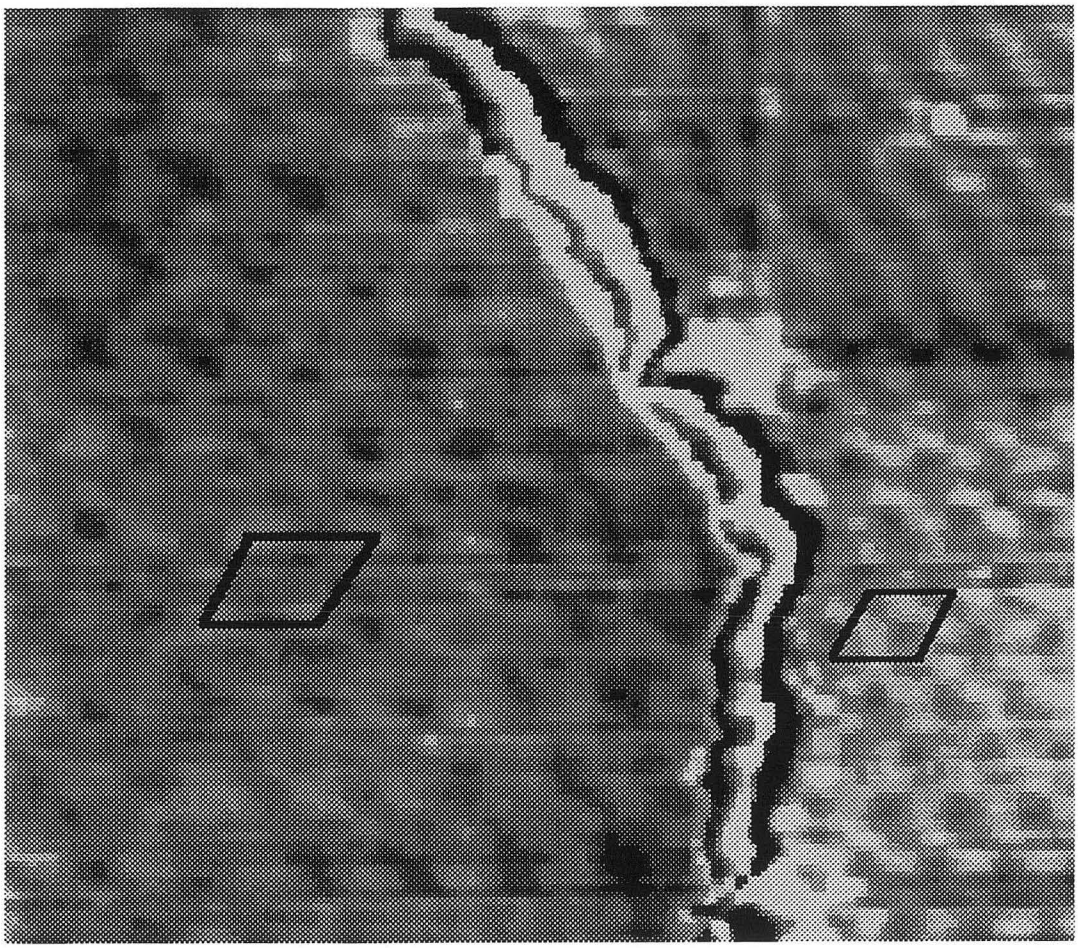

Figure 4.8 Coexistence of Moiré patterns

On the right, the monolayer FeO large periodicity is visible and the 26 Å unit cell is marked on the image. On the left of the step edge, a 43 Å periodicity Moiré pattern is observed and the corresponding unit cell is also drawn for comparison. (300 Å x 270 Å, I = 1.0 nA, Bias = -0.91 V)

An atomic scale resolution image of the Moiré pattern is shown in Fig. 4.9. One possibility is that this structure is due to a lattice mismatch between two iron oxide overlayers. The difference between the two lattice constants causing the mismatch should be smaller than between FeO and Pt because the Moiré pattern has a larger periodicity.

For example, the FeO and Fe_2O_3 lattices have bulk lattice constants of 3.04 Å and 2.90 Å for a difference of .14 Å or only 5%. There is also a slight rotation visible as a difference between the atomic and large periodicity lattice directions that has not been analyzed carefully.

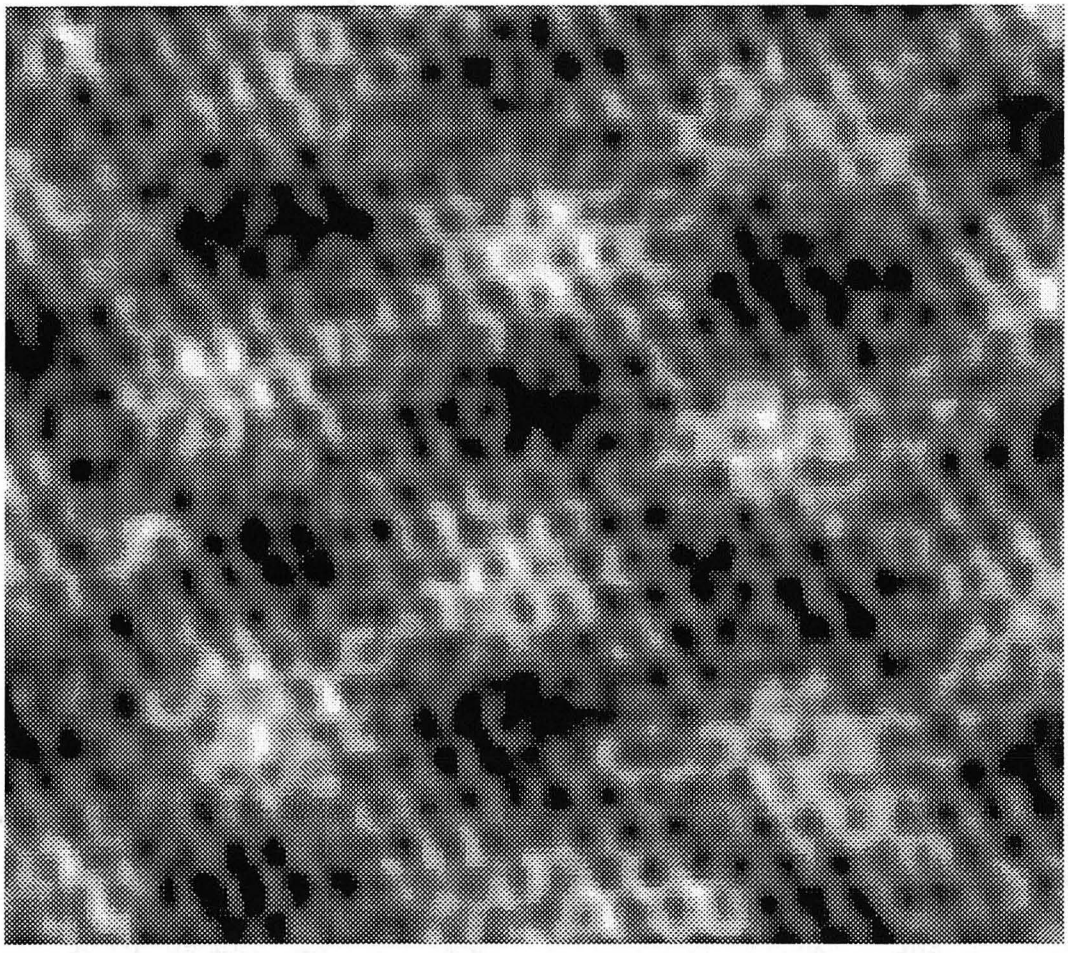

Figure 4.9 Atomic scale structure of α-Fe_2O_3 Moiré pattern

In this 121 x 106 Å image, the atomic unit cell and large unit cell are both clearly visible. (I = 1.17 nA, Bias = -0.84 V)

On α-Fe_2O_3 single crystals, a complex LEED pattern has been observed with a ~42 Å super structure and rosettes of beams observed around all the primary beams that

would be expected from a $\sqrt{3}x\sqrt{3}R30°$ periodicity [1, 8]. In recent work by Condon, et al, STM images of the α-$Fe_2O_3(0001)$ surface show that a structure consisting of an ordered array of islands of FeO on top of the α-$Fe_2O_3(0001)$ surface corresponds to the complicated LEED pattern [9]. The symmetry of the large Moiré α-$Fe_2O_3(0001)$ structure formed on Pt(111) and this result on the iron oxide single crystal are essentially identical with both having the same mixture of small and large periodicities and symmetries. This suggest that the result observed on the Pt(111) may be due to an α-$Fe_2O_3(0001)$ forming over an FeO(111) layer while the single crystal structure is formed by a partial layer of FeO(111) over α-$Fe_2O_3(0001)$. In their work, the FeO only partially covers the surface systematically overlaying one site in the unit cell while for the Pt(111) overlayer result, the coverage of the unit cell is complete. The lack of contact with the bulk iron oxide crystal may allow larger relaxations of the lattice constant.

The islands with this large Moiré pattern only grow slowly with increasing coverage. The rest of the iron oxide appears to nucleate in crystallites that are widely spaced on the surface. These crystallites have multilayer step heights and lateral sizes of 100-500 Å. Atomic resolution on the crystallites was not achieved.

4.4 Summary and Conclusions

For oxygen pressures of 10^{-5} torr, the iron oxide grows with a 2x2 structure with respect to the FeO monolayer and is assigned to $Fe_3O_4(111)$. The structure is difficult to order well on the local scale but has been more thoroughly investigated by diffraction methods. This structure always appears with a large number of defects possibly due to the strain energy associated with the lattice mismatch. For oxygen pressures of 10^{-4} torr, the oxide structure has a $\sqrt{3}x\sqrt{3}R30°$ structure and is assigned to α-$Fe_2O_3(0001)$ which coexists with the FeO monolayer. Forming a continuous layer of this structure was not achieved in these experiments even for amounts of iron oxide equivalent to several monolayers. A large periodicity Moiré pattern is also observed for the Fe_2O_3 structure

which is tentatively assigned to an α-Fe_2O_3(0001) surface over an FeO(111) layer largely due to the striking similarity of the unit cell periodicities to structures observed on the α-Fe_2O_3(0001) single crystal surface.

The 2x2 and $\sqrt{3}x\sqrt{3}R30°$ periodicities corresponding to Fe_3O_4(111) and α-Fe_2O_3(0001) are observed on both the Pt surface and the single crystal oxide surface [8, 10]. However, the complete FeO monolayer is not observed for the single crystal oxide system although an island structure of FeO is formed. Although a 43 Å periodicity structure with similar features is observed for both systems, STM images reveal that they do not correspond to the same structure although possibly to similar interfaces. Overall the multilayer structures of iron oxide appear to follow the bulk phase diagram with higher oxidation states observed at higher oxygen pressures, but the layer near the interface may not oxidize leaving the overall stoichiometry still somewhat reduced. As was also demonstrated for the case of FeO/Pt(111), obtaining results by examining the symmetry of real space images is the most direct and reliable method of extracting information from STM images.

Chapter 4 References

[1] R.J. Lad and V.E. Henrich, Surf. Sci. **193,** (1988) 81.

[2] R.G. Wyckoff. *Crystal Structures.* (Interscience Publishers, New York, 1963).

[3] A. Barbieri, W. Weiss, M.A. Van Hove and G.A. Somorjai, Surf. Sci. **302,** (1994) 259.

[4] W. Weiss, A. Barbieri, M.A. Van Hove and G.A. Somorjai, Phys. Rev. Lett. **71,** (1993) 1884.

[5] Y.J. Kim, C. Westphal, R.X. Ynzunza, H. Xiao, Z. Wang, H.C. Galloway, M. Salmeron, M.A.V. Hove and C.S. Fadley, in preparation (1995)

[6] H.C. Galloway, P. Sautet and M. Salmeron, in preparation (1995)

[7] B.J. McIntyre, P. Sautet, J.C. Dunphy, M. Salmeron and G.A. Somorjai, J. Vac. Sci. Technol. B **12,** (1994) 1751.

[8] R.L. Kurtz and V.E. Henrich, Surf. Sci. **129,** (1983) 345.

[9] N.G. Condon, F.M. Leibsle, A.R. Lennie, P.W. Murray, D.J. Vaughan and G. Thornton, Phys. Rev. Lett. **75,** 10 (1995) 1961.

[10] N.G. Condon, P.W. Murray, F.M. Leibsle, G. Thornton, A.R. Lennie and D.J. Vaughan, Surf. Sci. **310,** (1994) L609.

Chapter 5 Titanium oxide on Pt(111)

5.1 Introduction

5.1.1 Catalysis

Platinum/titanium oxide and rhodium/titanium oxide interfaces have a long history in the field of surface science for many reasons. The systems consisting of metal particles dispersed on metal oxide supports were demonstrated to show interesting catalytic properties both as real and as model catalysts. These systems were shown to have dramatically altered chemisorption and catalytic properties depending on whether the metal oxide was reduced or not. These properties, known as strong metal support interaction (SMSI) or the decoration effect were only observed for reducible metal oxides. The two major causes identified for the phenomena include charge transfer between the metal particles and metal oxide resulting in changed chemisorption properties and it has also been demonstrated that there is a structural change associated with the migration of lower oxides onto the metal surfaces. Although structural effects seem to have won out in the literature, the two are intricately related [1, 2].

Studies of model catalysts of TiO_x on Rh and Au have also been conducted [3-6]. In particular, for the case of TiO_x on Rh(111), a maximum rate for the hydrogenation of CO was observed for a .5 ML coverage. The model proposed to explain the rate variation consists of Ti^{+3} at the periphery of the islands. This agreed well with the STM results of Wang, et al [7]. However, attempts to reproduce those measurements in the early stages of this work were unsuccessful and were halted due to irreversible Si contamination of the Rh(111) single crystal. Results for submonolayer coverages of TiO_x on the Pt(111) will however be presented here.

As a result of the interest in the model catalytic systems, it was discovered by Boffa, et al [8] that TiO_x on Pt(111) forms ordered structures. At higher temperatures than those used to prepare the catalytic system (500-700 C as opposed to 300-400 C) a

variety of ordered LEED patterns are observed on the crystal. STM studies of the ordered structures of titania on Pt(111) will also be presented here.

5.1.2 Surface studies

In addition to catalytic studies, many surface science studies have been conducted on TiO_2 single crystal surfaces and one might hope to be able to use this background to understand the growth of ordered TiO_x layers on Pt(111). Titanium occurs readily in both the +3 and +4 oxidation states. Bulk structures include Ti_2O_3 which has the corundum structure (the same as α-Fe_2O_3 discussed earlier) and the most common form of TiO_2, which is called rutile (Fig. 5.1) [9].

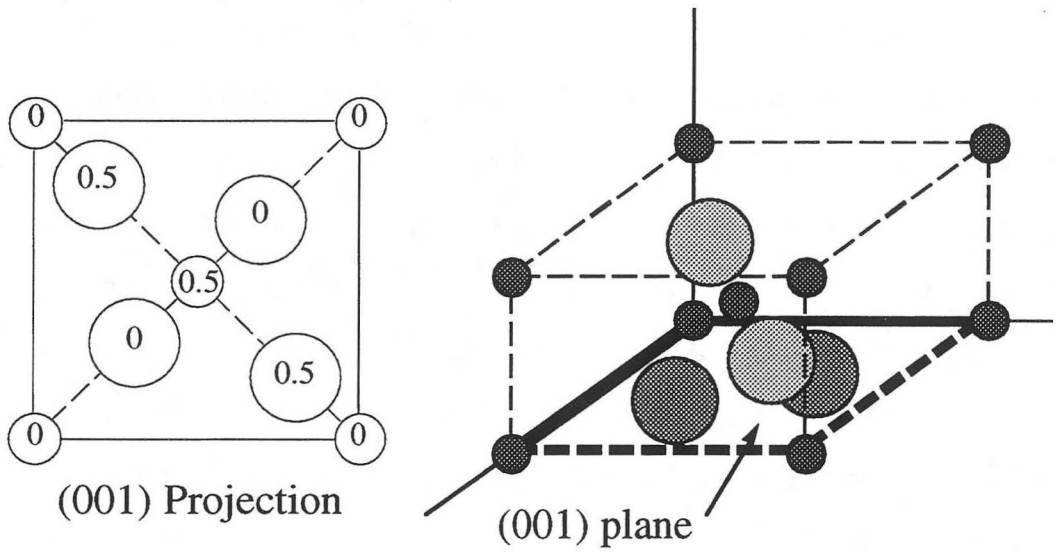

Figure 5.1 Rutile TiO_2

The small circles represent titanium and the large circles are oxygen. The projection onto an (001) plane is shown on the left with the height above the plane given for each atom in terms of the unit cell vector. On the right is the 3-D representation for the unit cell. The unit cell is 4.59 Å x 4.59 Å x 2.96 Å.

As an added complication, the stoichiometry can vary almost continuously as TiO_x, for $1.5 < x < 2$, by forming what are called Magnéli phases. These phases consist of an ordered array of defects occurring where oxygen octahedra are edge joined instead of corner joined effectively removing oxygen vacancy sites. More and more of this type of defect leads to increasing oxygen deficiency. This tendency complicates the structural possibilities for a thin TiO_x film.

TiO_2 is available as a bulk single crystal and can be made conducting by annealing in vacuum to produce oxygen vacancies. It has recently been confirmed that the (110) surface can be returned to stoichiometry by annealing in vacuum to a higher temperature (950 K) which allows Ti ions to migrate from the surface region into the bulk of the crystal leaving a stoichiometric surface [10, 11]. STM results with atomic scale resolution have been reported for the TiO_2(110), (001), and (100) surfaces with a variety of surface reconstructions [10, 12-18].

5.2 Experimental results

In these studies a layer of titanium is evaporated onto the clean Pt(111) surface using vapor deposition. The evaporator consists of a .030 inch diameter W wire wrapped with .020 inch diameter high purity Ti wire. Then the oxide is formed by heating the entire crystal in an oxygen pressure of 1–5 x 10^{-6} torr. At these temperatures, bare Ti metal begins to dissolve into the crystal so it is difficult to accurately assess how much Ti is lost but the majority remains on the surface. The platinum substrate does not form an oxide under these conditions. Sometimes the crystal is also post annealed in vacuum.

5.2.1 Ordered TiO_x/Pt(111)

5.2.1.1 High symmetry structure

A layer of titanium oxide is formed by evaporating Ti onto the surface, oxidizing at 550 C in a O_2 pressure of 1 x 10^{-6} torr and then the surface is post annealed in vacuum. XPS and ISS results have shown that the post annealing leads to a decrease in the surface

coverage to the monolayer level and a partially reduced oxide [8]. The AES Ti(387 eV)/Pt(237 eV) peak ratio for this structure consistently reduces to a value of ~2.5 regardless of the Ti/Pt ratio before oxidation. This value provides a calibration point for the completion of one monolayer.

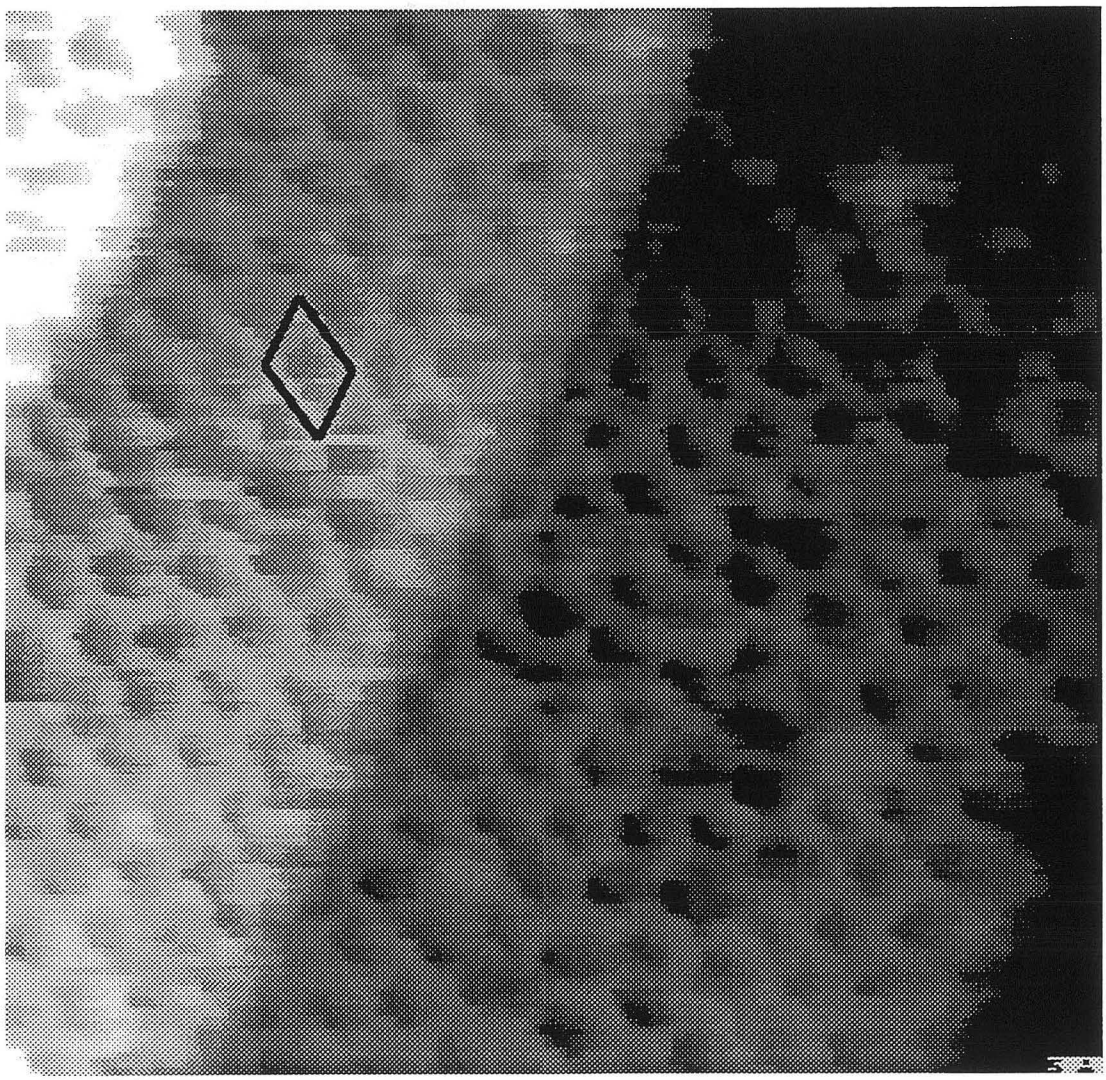

Figure 5.2 High symmetry structure

The unit cell of the high symmetry structure is marked on the central terrace. This unit cell is approximately 5.2 x 5.2 Å and the two directions appear to be equivalent. (100 Å x 100 Å, I = 0.98 nA, Bias = -470 mV)

A three fold symmetric atomic scale structure, shown in Fig. 5.2 (preceding page), with a ~ 5.2 Å lattice constant is observed that will be referred to as the high symmetry structure. The Pt(111) surface also has a three-fold symmetric unit cell with a 2.77 Å lattice constant. While the exact dimensions of the unit cell are difficult to determine with STM due to drift and hysteresis effects associated with the piezos, the symmetry with respect to the Pt(111) surface should be very straight forward. In fact on large terraces a Moiré pattern is observed that is also three fold symmetric as seen in Fig. 5.3. This type of structure is typical for a lattice mismatch with the substrate. Unfortunately most of the terraces on this particular crystal are too narrow to observe this pattern due to the fact that the crystal has a small miscut off the (111) plane and the periodicity of the large unit cell is big, ~40-60 Å. The structure is proposed to be Ti_2O_3(0001) based on the knowledge that it is a more reduced layer and on the unit cell symmetry. Unfortunately, XPS and structural measurements (such as STM or LEED) have not been made simultaneously making it difficult to assign stoichiometry unambiguously to each structure.

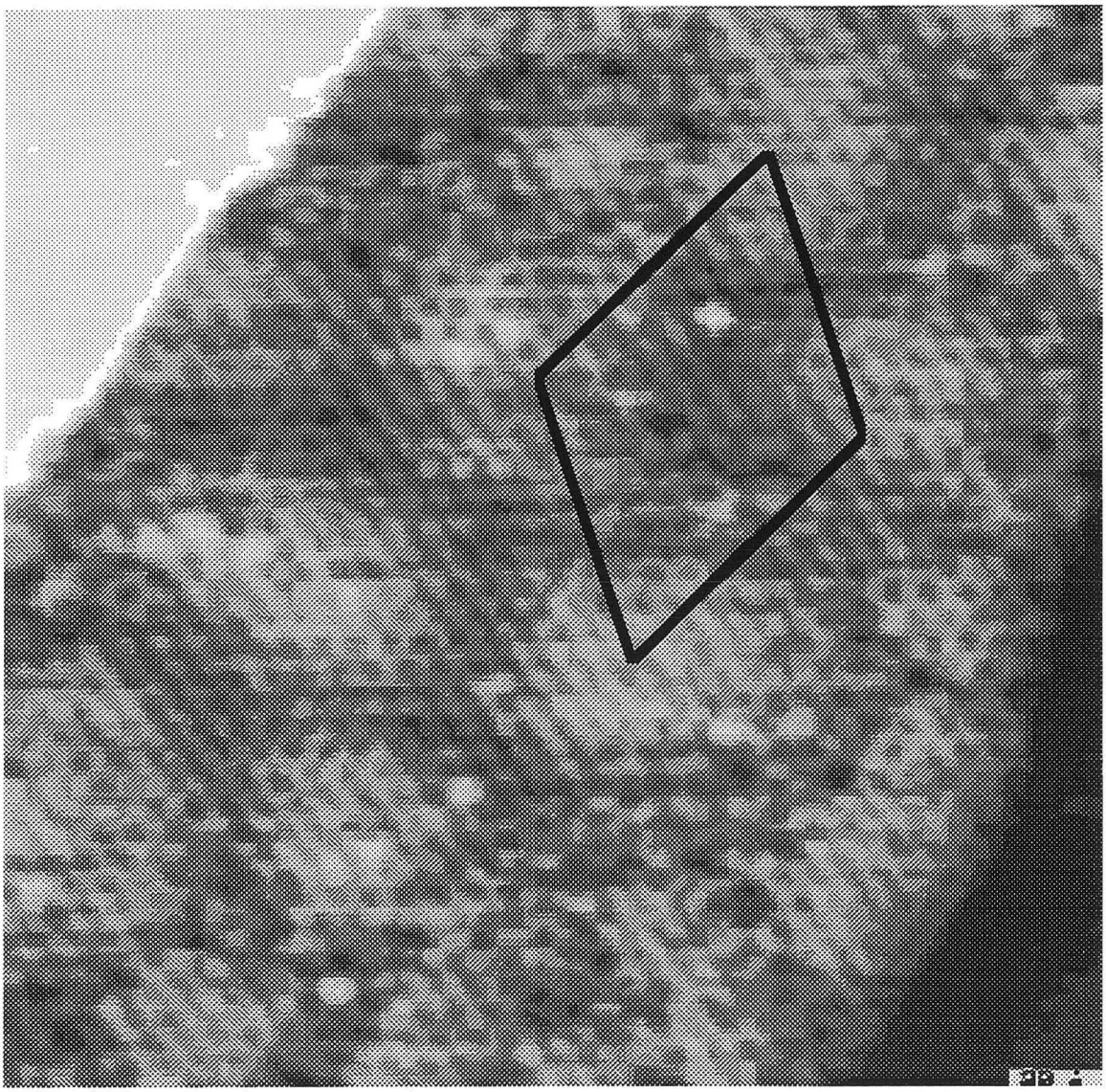

Figure 5.3 Moiré pattern - high symmetry structure

On the wide terrace in the middle of the image some circular areas appear to be 'higher' than the rest of the image. The contrast on the terraces in the corners has been removed for clarity but the same structure exists there. Only on large enough terraces is the Moiré pattern observed. (240 Å x 240 Å, I = 0.98 nA, Bias = -470 mV)

As shown in Fig. 5.4 the $Ti_2O_3(0001)$ is a close packed plane of oxygen atoms with Ti atoms in a $\sqrt{3}x\sqrt{3}R30°$ arrangement. The spacing of the Ti atoms is 5.15 Å, in good agreement with the STM data. Unfortunately the small terrace size of the Pt substrate in this experiment makes it very difficult to use the method discussed previously for calculating the lattice parameter of FeO/Pt(111) (as in Ch 3.3.3). The small and large unit cells again seem to be rotated with respect to each other by an angle of ~10°. As was detailed for the case of FeO this does not correspond to the amount of rotation with respect to the underlying Pt layer and in fact the small unit cell lattice directions seem to be along the close packed directions based on observations of the steps in the Pt substrate.

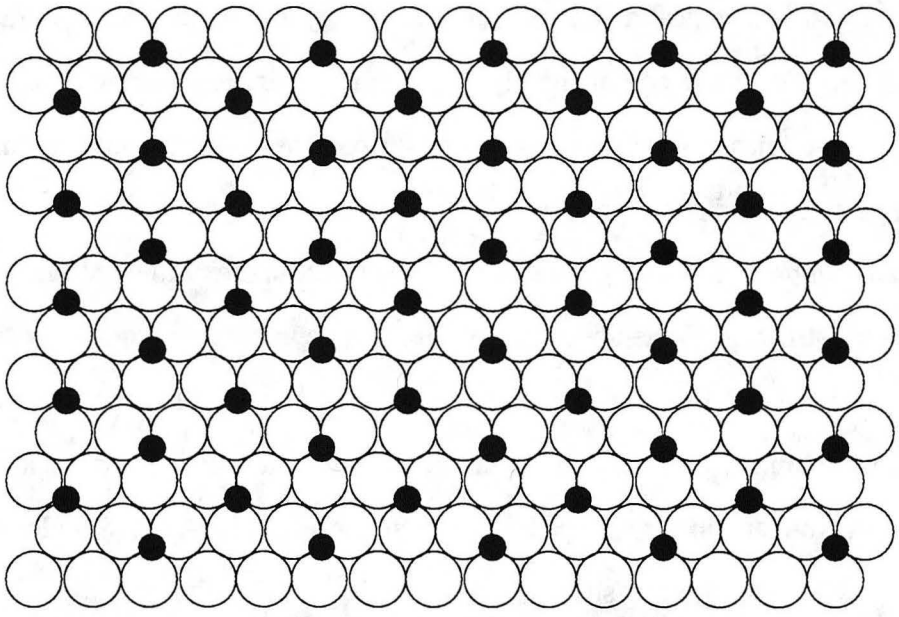

Figure 5.4 $Ti_2O_3(0001)$ surface

The small filled circles are titanium and the large open circles are oxygen. The spacing between neighboring Ti atoms is 5.15 and the O-O spacing is 2.97 Å

This structure also appears to uniformly cover the surface in Figs. 5.2 and 5.3 indicating complete wetting of the substrate. It has often been postulated that for metal oxide/metal interactions a slightly reduced layer of the oxide will have a stronger interaction with the metal leading to improved wetting.

5.2.1.2 Low symmetry structure

As the coverage is increased ≥ 1 ML, the complexity of structures observed on the surface increases dramatically. The sample preparation consists of evaporating Ti and then heating at 550 C in an oxygen pressure of 5 x 10^{-6} torr with no post annealing step. In these experiments the Ti(387 eV)/Pt(237 eV) AES peak ratios are ~4 for these preparation conditions indicating a coverage significantly above the monolayer (Ti/Pt ratio of ~2.5). In Fig. 5.5, an image obtained after such a preparation is shown. The ordered structure observed has a unit cell of ~15 Å x ~20 Å. There appears to be an alignment with the step edges and some patches of the previous high symmetry structure are still observed although not visible on this image. The new structure will be referred to as the low symmetry structure. When both the low and high symmetry structures are observed in the same image, the low symmetry structure always appears topographically higher than the high symmetry one, indicating that it only occurs for thicker layers than the high symmetry structure and in agreement with the trend observed by AES. Smaller images in the same area as Fig. 5.5 are shown in Figs. 5.6 and 5.7. These show increasingly smaller details of the structure but the large cell is no longer clearly visible, although some hints can be seen as alternating bright and dark rows.

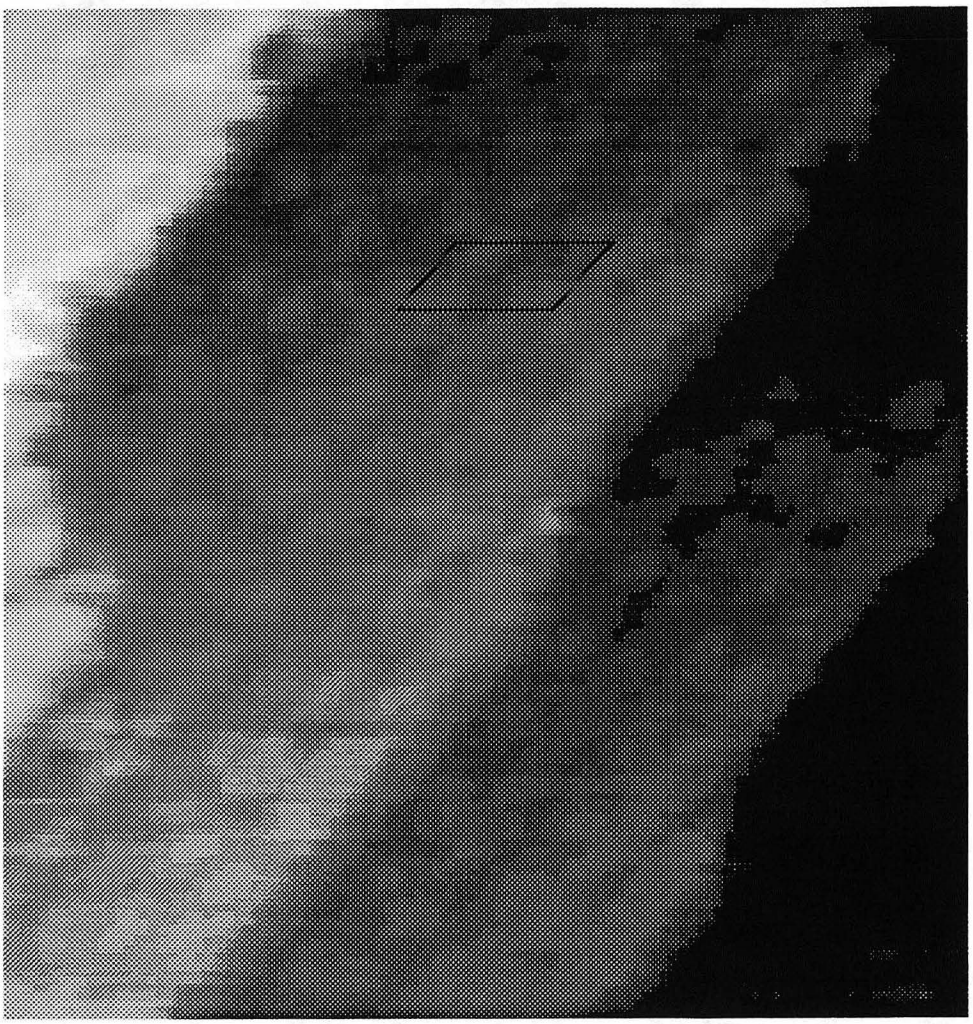

Figure 5.5 Low symmetry structure - large unit cell

In the 220 Å x 230 Å image the unit cell of ~15 Å x 20 Å is observed. The steps seem to be somewhat aligned with the structure. The step height between terraces is that of a Pt(111) monatomic step (2.3 Å). (I = 1.3 nA, Bias = -26 mV)

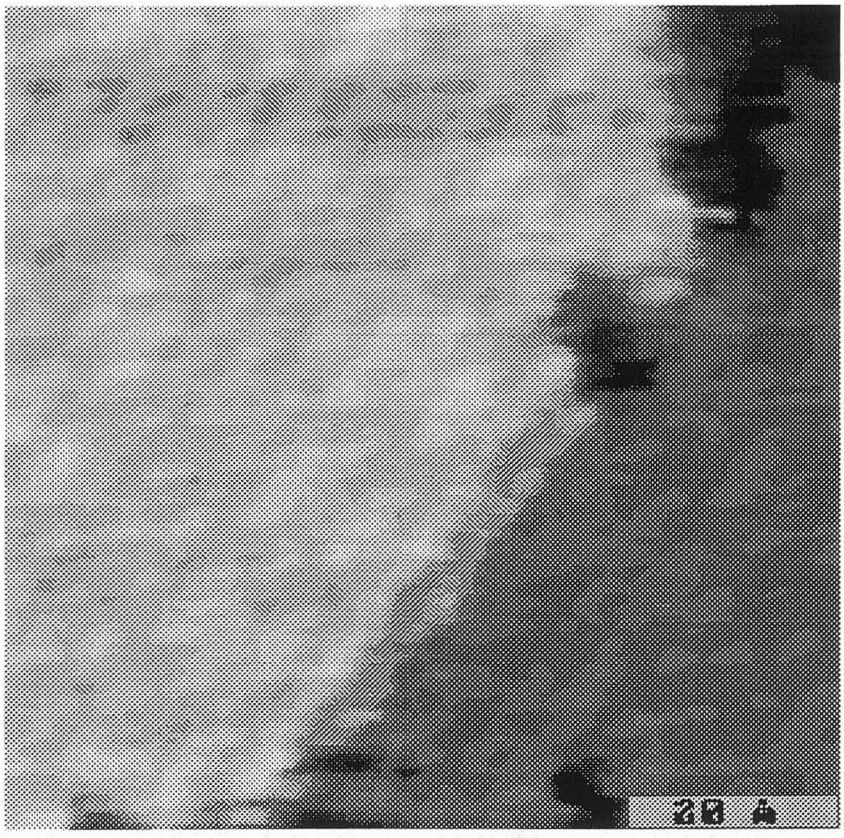

Figure 5.6 Low symmetry structure 80 Å x 80 Å

Smaller scale features of the unit cell are visible including ~5 Å space rows, but the previously seen 15 x 20 Å unit cell is not clear. (I = 1.27 nA, Bias = -27 mV)

Finally, to possibly remove some of the influence of defects a correlation image is made of Fig. 5.7 which is shown in Fig. 5.8. This is a data processing method to determine the average unit cell in the image. Some possible unit cell periodicities are indicated on the image. Several other possibilities exist and these particular unit cells are chosen by examining a large number of images for those that seem the most predominant. Since it is not clear what the fundamental symmetry or unit cell is from the different images, it is difficult to unambiguously assign a unit cell and thus the data does not allow the determination of the overlayer symmetry with respect to the substrate. However,

some simple observations can be made about the structure. Close examination of the images reveals that the smallest unit cell has some internal structure and the two most obvious lattice directions are not equivalent, so the surface is not three-fold symmetric like the underlying Pt(111) or the ordered iron oxide structures observed on Pt(111).

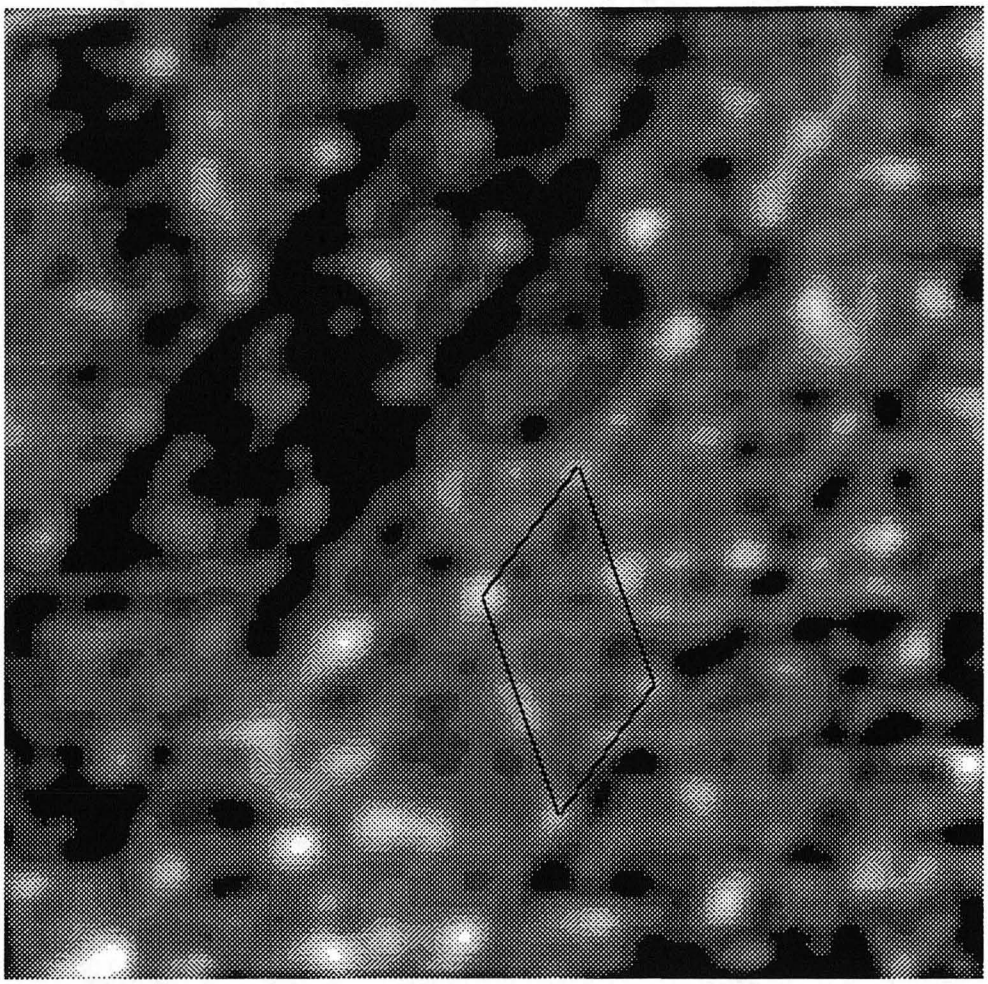

Figure 5.7 Low symmetry structure 40 Å x 40 Å

Atomic scale features are visible as well as alternating bright and dark rows that make up the periodicities observed in Figs. 5.5-6. The smallest unit cell (drawn on the figure) has dimensions of ~5.5 x ~5.5 Å. (I = 1.23 nA, Bias = -27 mV)

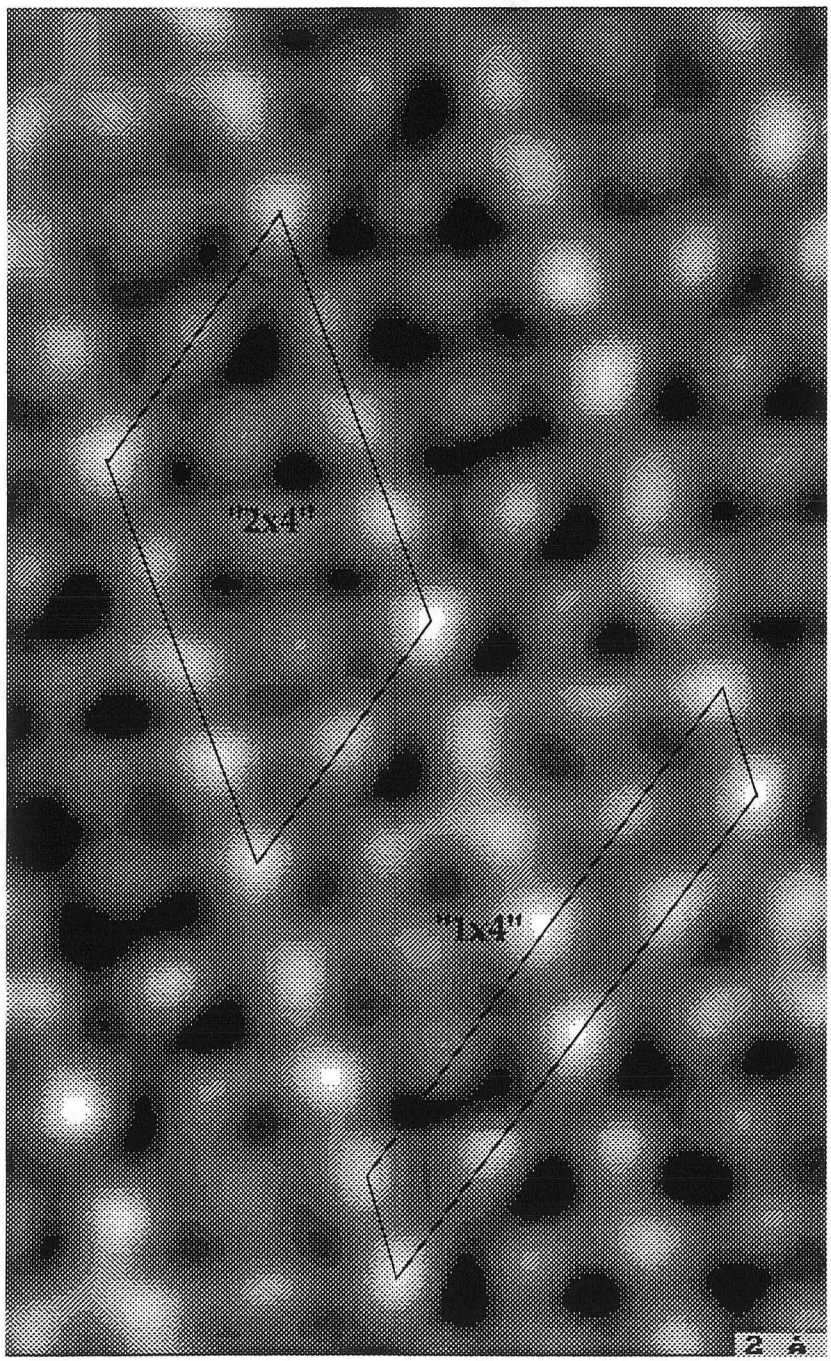

Figure 5.8 Correlation image of low symmetry structure

The correlation image shows two possibilities for the unit cell. The "2x4" and "1x4" refer to the number of TiO_x unit cell spacings and not to the underlying substrate.

From a different set of experiments in similar preparation conditions, a series of 70 x 70 Å images of the same terrace are shown in Fig. 5.9. The common feature in all of them is the bands running diagonally from top right to bottom left. The direction of the bands is approximately the same as one of the close packed Pt direction just as the images in Figs. 5.5-9 showed an alignment with the [110] direction steps. Only at the smallest gap values are atomic scale features visible although the two images at ~1.8 MΩ are different indicating tip changes may affect the image contrast as well. Again these images do not have easily recognizable symmetry but the complicated small unit cell and the inequivalence of the two directions is the same as in the previous sets of images.

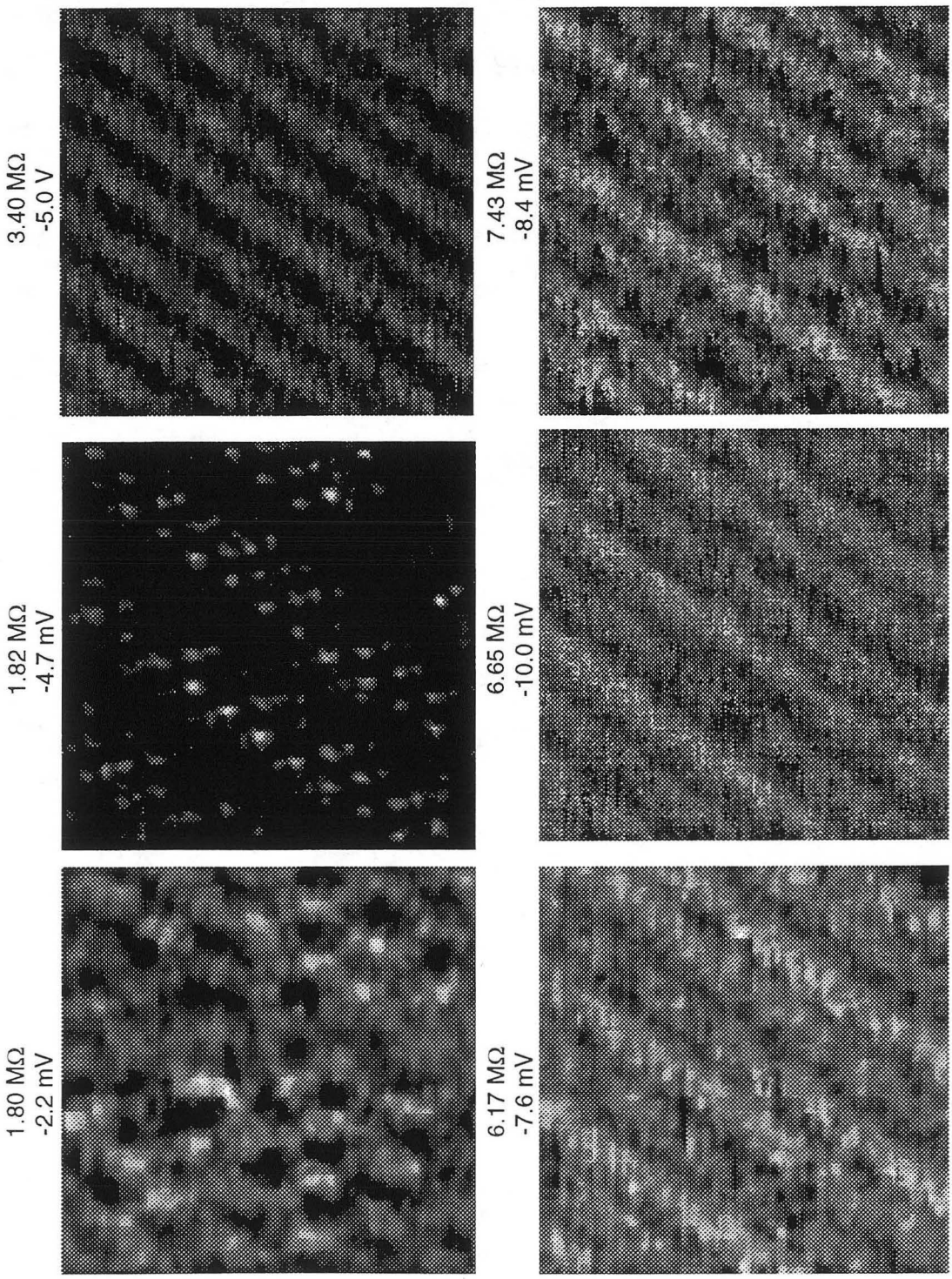

Figure 5.9 Gap dependence of low symmetry images

Images with the same size (70x70 Å) taken at slightly different gap values and bias voltages are shown.

The inequivalent directions suggest a Moiré structure caused by a pseudo hexagonal layer such as a $TiO_2(111)$ surface to explain the observed large periodicity of the overlayer. The $TiO_2(111)$ structure is shown in Fig. 5.10.

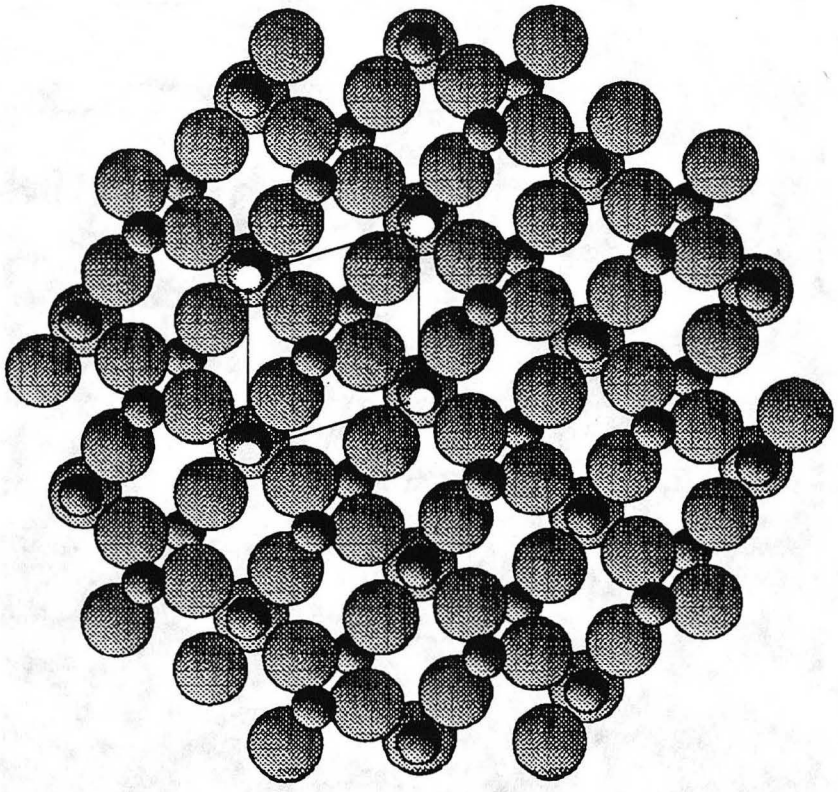

Figure 5.10 $TiO_2(111)$ surface

The $TiO_2(111)$ surface with a unit cell marked with black lines and white circles at the corners. Small circles represent Ti and the large circles are oxygen. The unit cell is 5.46 Å x 5.46 Å with an angle of 53° between the sides of the unit cell.

This structure has a lattice constant of 5.46 Å for both sides of the unit cell but the two sides are separated by an angle of 53°. The length is close to twice the Pt lattice constant of 5.54 Å but there is a 7° angle mismatch compared to the 60° angle on a (111) surface. A close up of the atomically resolved image in Fig. 5.9 is shown in Fig. 5.11. This suggests a "1x5" periodicity in the TiO_2 overlayer while in Fig. 5.8 the correlated image suggests a "1x4" or possibly a "2x4" cell.

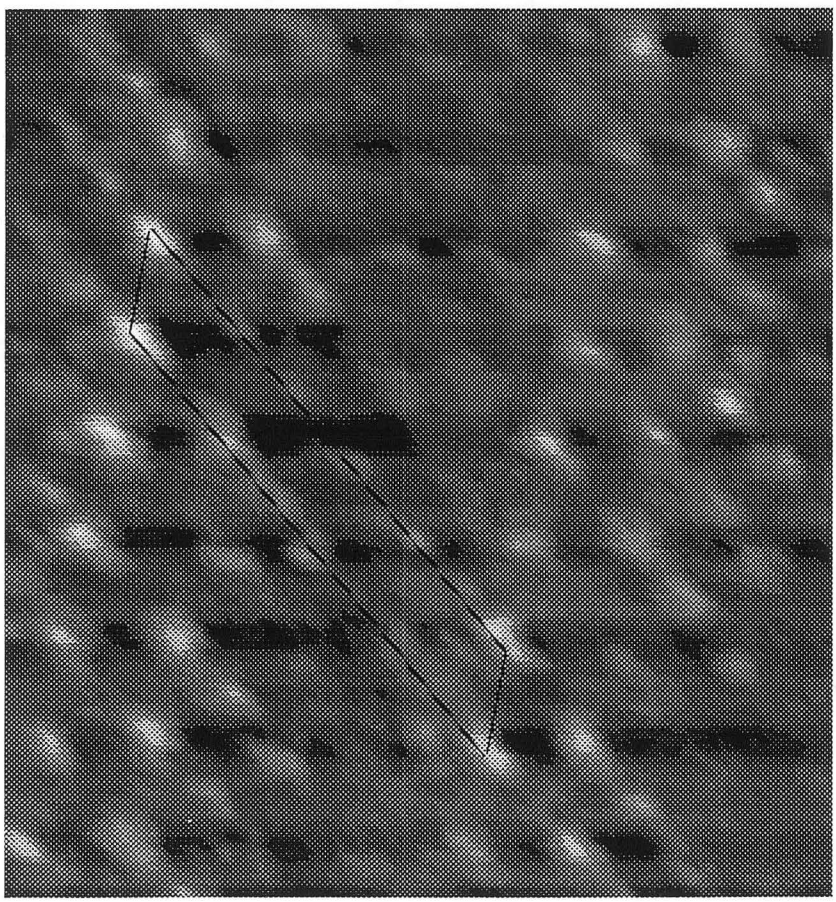

Figure 5.11 Unit cell of low symmetry structure - "1x5"

A magnified view of the second image in Fig. 5.9 with a "1x5" unit cell outlined. The maxima in the image are not evenly spaced along the large side of the unit cell making it hard to determine the exact periodicity. (I = 2.61 nA, Bias = -4.7 mV).

In Fig. 5.12 the overlayer is shown for a "1x5" unit cell. The parameters have been adjusted so that the overlayer fits exactly to aid in visualization.

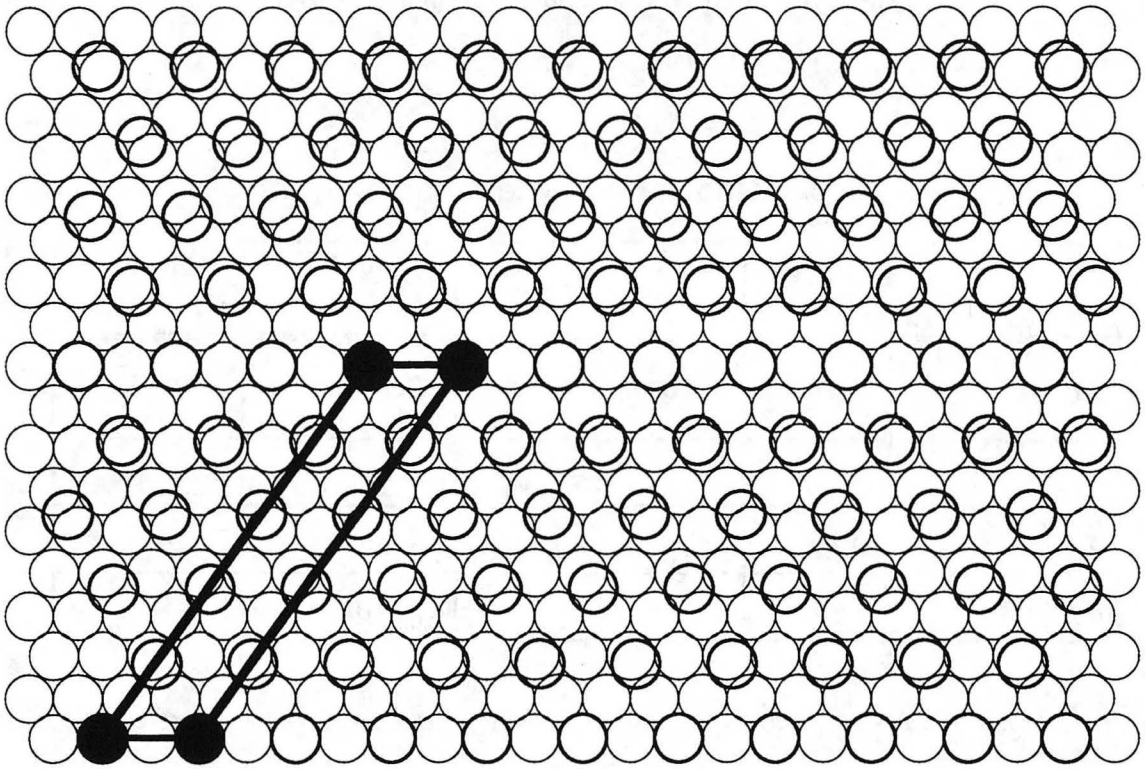

Figure 5.12 Model for the "1x5" unit cell

The heavy circles represent the corners of the $TiO_2(111)$ unit cell and the thin circles are the Pt lattice. The "1x5" unit cell is drawn in heavy lines and the corners of the unit cell are filled circles. Although the corners are chosen to be on top sites for this model the exact registry with the substrate is not known.

To further test the plausibility of this model, the change in an ideal $TiO_2(111)$ unit cell that would be required to fit exactly onto the Pt lattice has been calculated for each of the three proposed unit cells. In Table 5.1, the variations in the lattice parameters, angle and unit cell area required for an exact fit for each of the proposed model unit cells are summarized, where a and b are the two sides of the unit cell, Θ is the angle between them

and (ab)sin(Θ) is the unit cell volume. Δ is the change in unit cell area with respect to the bulk $TiO_2(111)$ unit cell area expressed as a percentage. These numbers are only to demonstrate the plausibility of the model and do not necessarily correspond to lattice constants of the surfaces.

Table 5.1 Model parameters for $TiO_2(111)$

	a (Å)	b(Å)	Θ	ab sin Θ ($Å^2$)	Δ(ab sin Θ)
Theoretical $TiO_2(111)$-1x1	**5.46**	**5.46**	**53.0°**	**23.81**	**0.0 %**
"1x4"	**5.54**	**5.23**	**53.4°**	**23.25**	**-2.3 %**
"1x5"	**5.54**	**5.38**	**54.8°**	**23.91**	**+0.5 %**
"2x4"	**4.99**	**5.23**	**52.7°**	**20.78**	**+12.7 %**

While the 2x4 cell seems to involve a severe change, the 1x4 and 1x5 are clearly plausible. Although the model is somewhat tenuous it is interesting to note that the $TiO_2(111)$ surface has only on occasion been reported to be stable [18]. However previous work on iron oxide [19, 20] and nickel oxide [21] overlayers on close packed noble metals have shown that other polar surfaces can be stabilized. It is also known that TiO_2 easily becomes oxygen deficient forming Magnéli phases so it is possible that more than one structure is observed as the stoichiometry changes slightly and ordered arrays of defects are introduced. This is also suggested by the variations in O/Ti ratio that are observed by AES.

5.2.2 Stoichiometric TiO_2

Finally in Fig. 5.13 is presented the structure observed for the highest O/Ti ratios. This surface has evenly spaced rows in one direction (labeled A) and disordered "snakelike" rows of maxima (labeled B) crossing them. Small pits are seen in the layer as

well, indicating only partial wetting of the overlayer. This is consistent with the XPS and ISS results that showed the reappearance of a Pt signal for the fully oxidized surface. Although no model has been developed for this surface the row structures do suggest the bulk $TiO_2(110)$ surface which is the most stable face of the rutile phase.

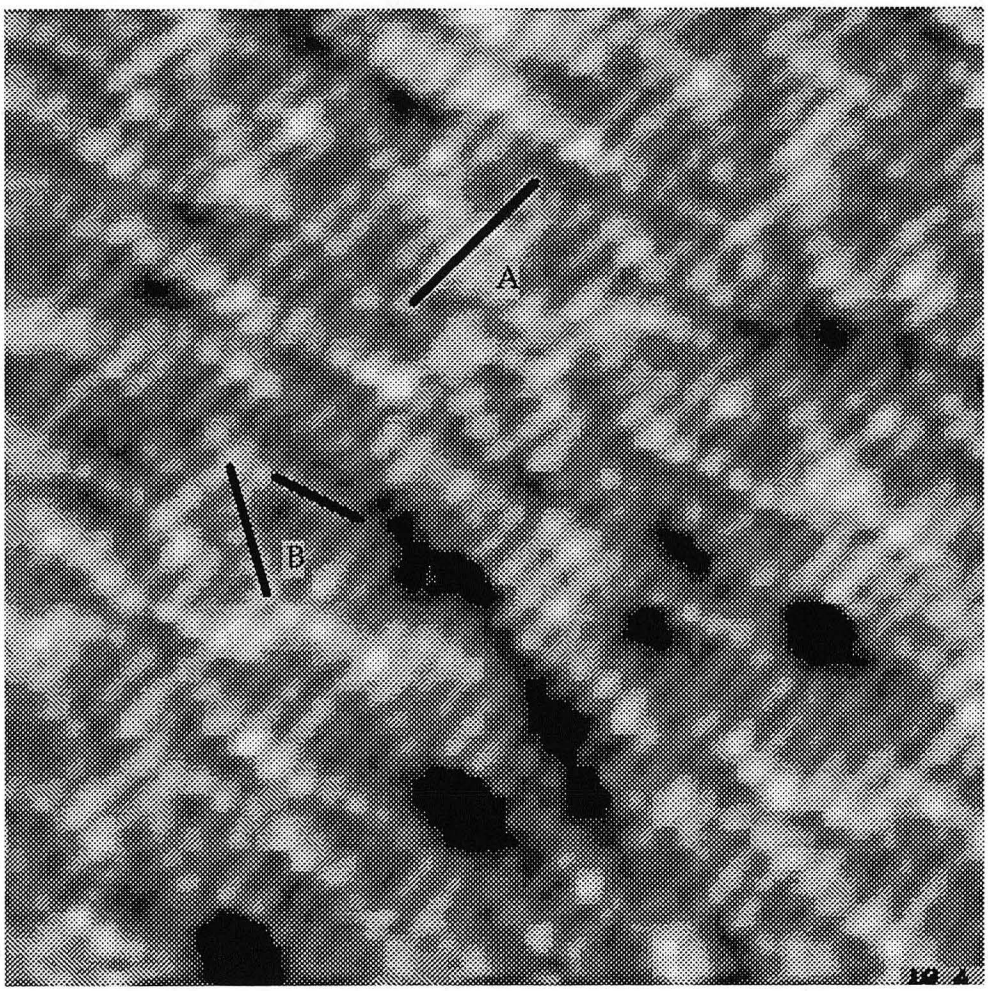

Figure 5.13 Fully oxidized TiO_2/Pt(111)

The ordered rows are in the direction marked as A and the disordered features are marked as B. Spacing between the A rows is ~3 Å. Note the small dark holes that are possibly pits down to the Pt substrate. (110 Å x 110 Å, I = 0.96 nA, Bias = 1.12 V)

5.2.3 Submonolayer TiO_x on Pt(111)

Submonolayer coverages of TiO_x were prepared by evaporating less than a monolayer of titanium and then heating to ~300 C in an oxygen pressure of $5x10^{-6}$ to $5x10^{-7}$ torr. To attempt to create a sample similar to that of the TiO_x/Rh(111) model catalyst, the sample is then dosed with CO and flashed (~5 sec) to 500 C. This reduction step is an attempt to change the stoichiometry of the titania from fully oxidized to partially reduced. However, only slight changes in the O/Ti ratio as measured by AES were observed. This may be due to an inefficiency in either the reduction step or in the fact that the sample as first prepared was not fully oxidized and therefore the reduction step had little effect. It is likely that on platinum surfaces in a vacuum environment, the equilibrium condition is quickly achieved for the submonolayer, due to background partial pressures of CO and H_2. This is different from the case for rhodium which binds oxygen more strongly than platinum. The reactions of CO and H_2 with oxygen are also known to occur at room temperature on Pt(111).

Scanning tunneling microscopy images show a variety of islands of TiO_x on the surface. They have basically rounded shapes and range in size from 40-300 Å. Probably the most interesting characteristic of the islands is that there is some second layer growth often located at the edge of the islands. Three topographs are shown in Fig. 5.14 for coverages of 0.3-0.5 ML. While one possible explanation is simply second layer growth of the oxide, a second explanation is a change in the tunneling probability due to a different stoichiometry and structure. Of course both a topographic and structural change could also be present. Unfortunately atomic resolution on the islands was not achieved so the structure could not be determined precisely.

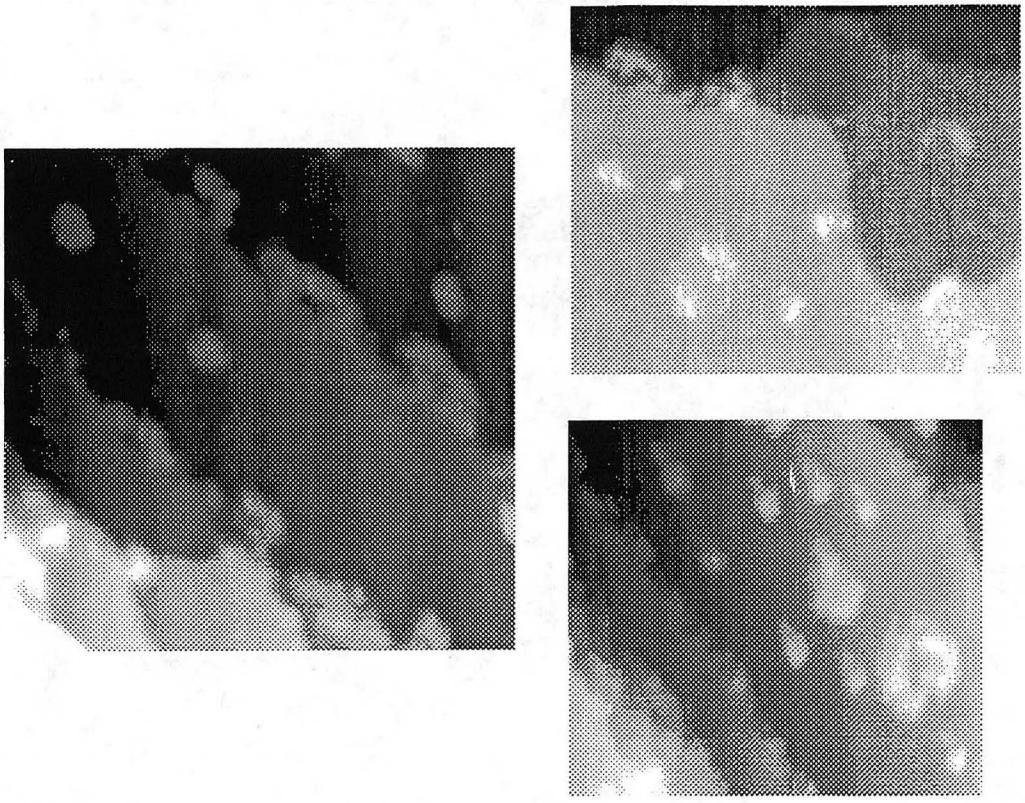

Fig. 5.14 Submonolayer TiO_x/Pt(111)

A selection of images are shown for submonolayer coverages. The image on the left is 950 Å x 950 Å, upper right is 1700 Å x 1200 Å and the lower right is 700 Å x 600 Å.

There is some indication that the two levels are different because they undergo different contrast changes. In Fig. 5.15 two images taken at the same bias and current are shown. In the left image, the larger islands appear approximately 2.2 Å above the terrace and the small second level island actually appears 2.4 Å below the terrace for a total height difference between the two of 4.6 Å. In the image on the right the large portion of the island is only 0.4 Å above the terrace and the smaller portion is 1.4 Å above for a total height difference of 1.0 Å. This change in contrast is analogous to that observed for the

Fe_2O_3/FeO structure discussed previously. In that case the structures were clearly resolved and were known to be different.

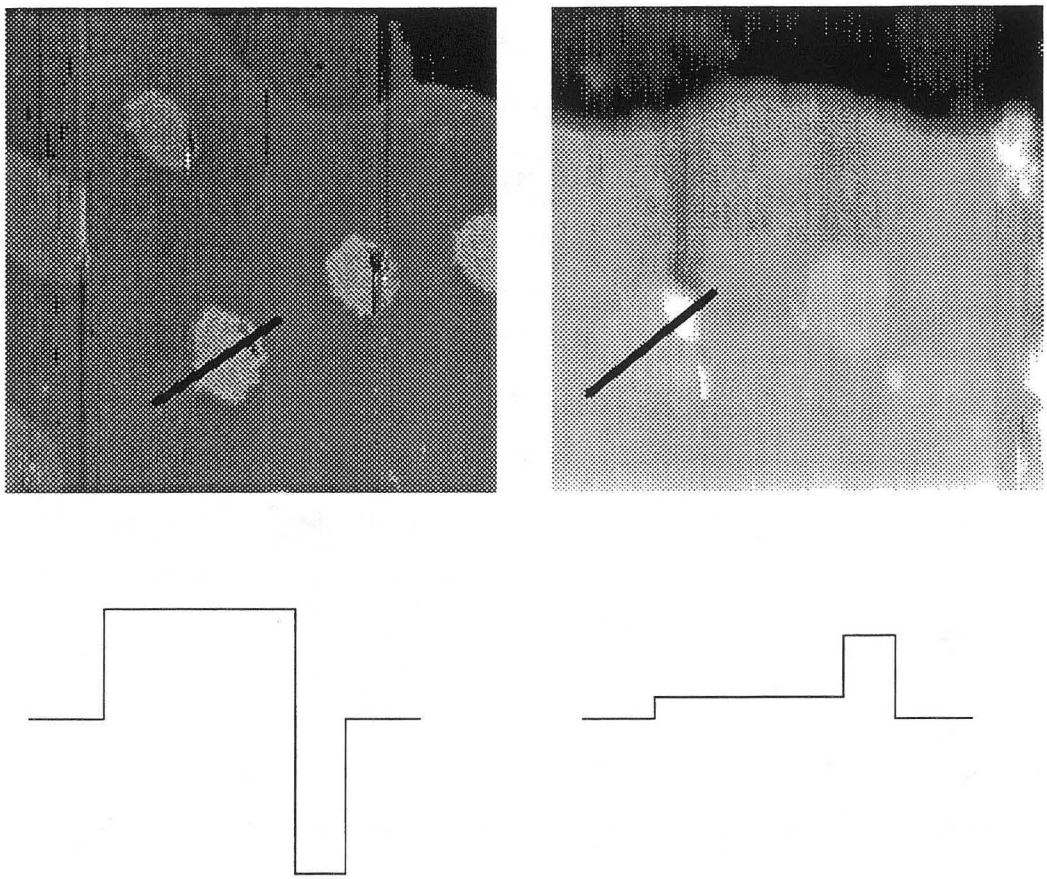

Fig. 5.15 Contrast reversal - TiO_x/Pt(111)

In the 770 Å x 800 Å image on the left the large islands are 2.2 Å above the terrace and the small islands are 2.4 Å below. In the 870 Å x 630 Å image on the right the small islands only appear 0.4 Å above the terrace and the small islands are 1.4 Å above the terrace. Both images are taken at a bias voltage 235 mV and a current of 0.55 nA. The schematics below the images are for the cursor lines drawn across each image.

5.2.3.1 Barrier height imaging

To investigate this further, barrier height images of the surface were recorded. In this imaging mode a small modulation is applied to the z piezo and the corresponding change in current is recorded with a lock-in amplifier. The average z height required to maintain the average current constant is also recorded. Thus, both the barrier height and constant current images of the same section of the surface are made simultaneously. From the one dimensional barrier formula for tunneling

$$\Phi = \frac{\hbar^2}{8m}\left(\frac{1}{I}\frac{dI}{dz}\right)^2 \qquad (1)$$

Since I should be constant the simplest interpretation of the contrast in a barrier height image is that it is proportional to the square root of the average sample barrier. For large enough tip sample distances and for vacuum tunneling where there is no contact between tip and sample, Φ should approach the average of the tip and sample macroscopic work function values. This is obviously complicated by topographic coupling at step edges but might be expected to have some validity on flat terraces. In Fig. 5.16 two pairs of images are shown. Images on the left are the z variations while the images on the right are barrier height contrast. The top and bottom pairs are acquired simultaneously. A modulation of 6 mV or a z motion of 0.1 Å at 13 kHz was used to take the images. Several small islands as well as a few second layer islands are visible. Using (1) to calculate Φ from the measured quantities yields the values listed in Table 5.2, where Φ_{Pt} is on the substrate, Φ_1 is on the big first level island and Φ_2 is on the second level island. V_{Bias} is the sample bias.

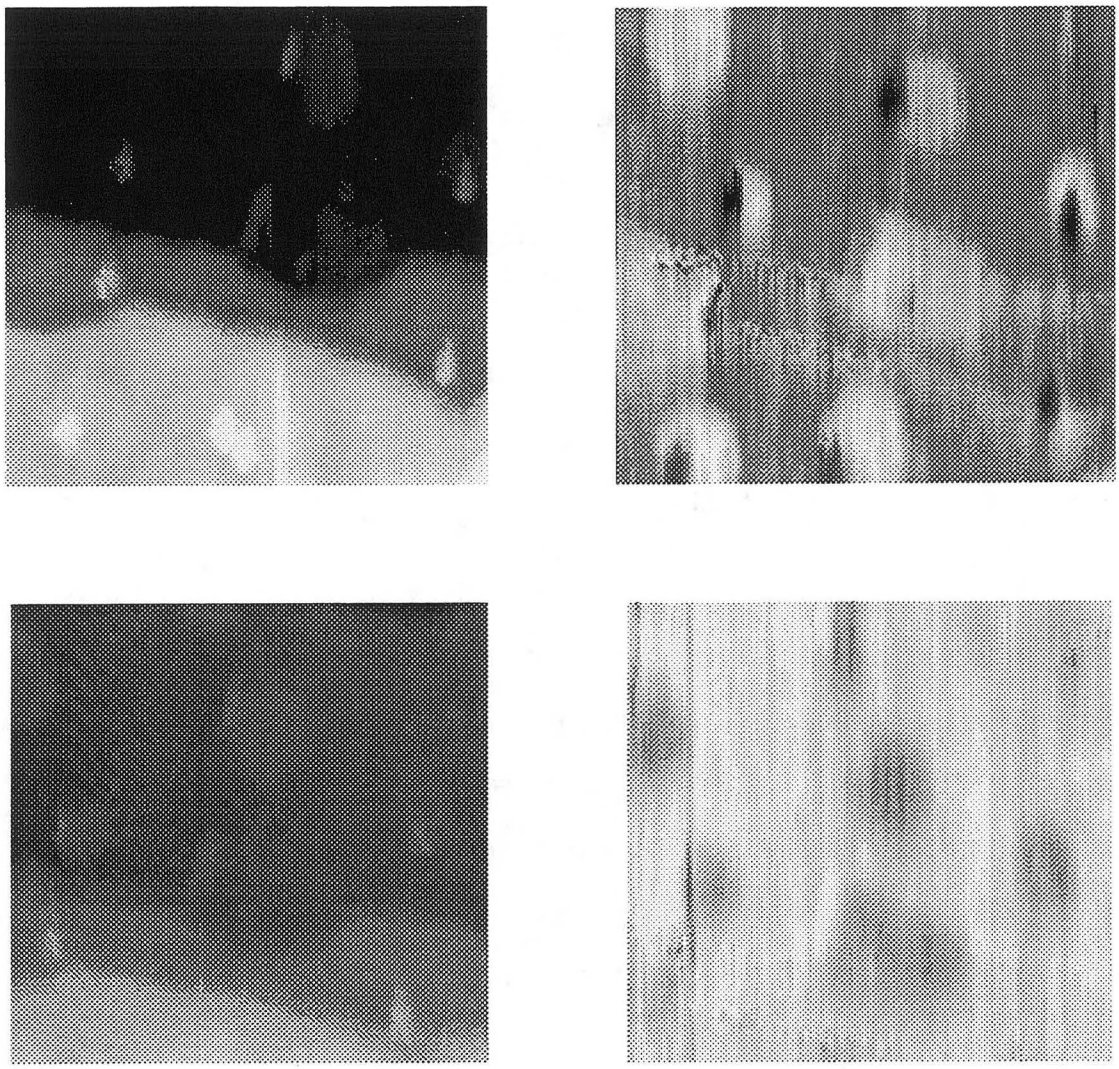

Fig. 5.16 Barrier height images of submonolayer titania

Two sets of images. The left side are topographic images both taken at a current of 1.31 nA. The top image sample bias is 0.026 mV and 0.53 V for the lower one. The images on the right are the corresponding barrier height scans. The images are both 900 x 900 Å and are taken in the same area of the sample as can be seen by the arrangement of islands. The barrier height contrast is reversed for the two images.

Table 5.2 Measured local barrier heights

	top image	bottom image
Φ_{Pt}	2.0 eV	2.9 eV
Φ_1	2.9 eV	2.0 eV
Φ_2	.5 eV	—
V_{Bias}	.026 V	.53 V

As can also be seen in the images, the relative values of the local barrier height for the substrate and island as measured by this method have inverted. In addition, the values of .5-3 eV are much lower than typical bulk work functions. This collapse of the barrier height has been observed for other systems. One explanation is that for very close proximity of tip and sample that the barrier is decreased by the overlap between the tip and sample wave functions [22]. Calculations for FeO/Pt(111) do indicate very small tip sample distances (as low as 4.2 Å). Another possible complication is that forces may be acting to deform the tip or sample so that the actual z displacement is less than the applied z, yielding incorrect values of the barrier height [23]. It is also possible that there is a layer of contaminants between tip and sample that are actually in mechanical contact thus also reducing the actual z displacement. This effect of reversed contrast, both in topography and barrier height images, is seen to be quite general for the oxide surfaces occurring in both the titanium and iron oxide systems. Similar effects have also been reported by other authors such as for the NiO/Au(111) interface [21]. While these effects complicate the interpretation of STM images, with better models taking into account more accurately the tip influence, it may be possible to extract information from these types of image contrast changes in the future.

5.3 Summary and conclusions

The ordered structures of titania proceed from a reduced layer at coverages close to one monolayer which can be assigned to a $Ti_2O_3(0001)$ surface to the lower symmetry structures that grow in the 1-3 ML range and are consistent with the $TiO_2(111)$ surface. For the highest oxidation achieved of the titanium, only partially ordered structures are formed. At the submonolayer level, islands are formed with an edge structure that appears to be electronically different. The islands nucleate on the terraces and also at step edges. The edge structure observed on many islands appears as a topographic elevation or depression, possibly depending on the tip structure. The barrier height on the edge structures appears to be lower than on the center of the islands. A summary of the structures and properties is detailed in Table 5.3.

Table 5.3 Summary of structures observed for titania on Pt(111)

Structure	Coverage and Stoichiometry	Properties
Submonolayer	< 1ML partially reduced	Two different phases of oxide are formed with contrast changes observed by STM
High symmetry structure	~ 1ML Ti2O3	Large periodicity, three-fold symmetric Moiré pattern, Ti2O3(0001)
Low symmetry structure	> 1 ML TiO2, or slightly reduced	Large periodicity, lower symmetry Moiré pattern, (bands in one direction), TiO2(111), complicated structure possibly due to small stoichiometry changes
Fully oxidized	> 1 ML TiO2	Partially ordered, highest oxidation state achieved in UHV conditions

In general, the understanding of titania on Pt(111) lags far behind the more detailed understanding achieved for the iron oxide system. However, there are several similarities that seem to be emerging that are also seen in other systems. One is that the first monolayer is a reduced form of the oxide. In this case, a $Ti_2O_3(0001)$ surface is postulated for the first monolayer growth. The first monolayer wets the surface forming a continuous structure indicating a reduction in energy due to the interaction between the substrate and overlayer. This can be understood in terms of the fact that in the reduced structure the metal cations are still available for bonding to the substrate. However, the surface appears to retain its own structure as seen by the observation of a Moiré pattern rather than adapting to the substrate lattice constant. This indicates that the overlayer-overlayer interactions are dominating the substrate-overlayer interactions, as was also observed in the iron oxide system. Unlike the case of FeO/Pt(111) where no contrast changes are observed in the < 1 ML regime, the titania seems to form two types of metal oxide in the form of islands with modified edge structures. This may be connected with the catalytic activity on the titania/Pt(111) system that the reducibility of the oxide at the interface is enhanced.

Chapter 5 References

[1] V.E. Henrich and P.A. Cox, *The Surface Science of Metal Oxides* , (Cambridge University Press, Cambridge, 1994).

[2] H.H. Kung, *Transition Metal Oxides: Surface Chemistry and Catalysis* , (Elsevier, Amsterdam, 1989).

[3] M.E. Levin, M. Salmeron, A.T. Bell and G.A. Somorjai, Surf. Sci. **195,** (1988) 429.

[4] K.J. Williams, M.E. Levin, M. Salmeron, A.T. Bell and G.A. Somorjai, Cat. Lett. **1,** (1988) 331.

[5] K.J. Williams, M. Salmeron, A.T. Bell and G.A. Somorjai, Surf. Sci. **204,** (1988) L745.

[6] M.E. Levin, M. Salmeron, A.T. Bell and G.A. Somorjai, J. Chem. Soc., Faraday Trans. I **83,** (1987) 2061.

[7] H.C. Wang, D.F. Ogletree and M. Salmeron, J. Vac. Sci. Technol. B **9,** 2 (1991) 853.

[8] A.B. Boffa, H.C. Galloway, P.W. Jacobs, J.J. Benítez, J.D. Batteas, M. Salmeron, A.T. Bell and G.A. Somorjai, Surf. Sci. **326,** 1-2 (1995) 80.

[9] R.G. Wyckoff, *Crystal Structures* , (Interscience Publishers, New York, 1963).

[10] M. Henderson, Surf. Sci. **343,** 1-2 (1995) L1151.

[11] H. Onishi and Y. Iwasawa, Surf. Sci. **313,** 1-2 (1994) L783.

[12] G.W. Clark and L.L. Kesmodel, Ultramicroscopy **41,** 1-3 (1992) 77.

[13] F.-R.F. Fan and A.J. Bard, J. Phys. Chem. **94,** 9 (1990) 3761.

[14] M. Sander and T. Engel, Surf. Sci. **302,** 1-2 (1994) L263.

[15] D. Novak, E. Garfunkel and T. Gustafsson, Phys. Rev. B **50,** 7 (1994) 5000.

[16] P.W. Murray, F.M. Leibsle, H.J. Fisher, C.F.J. Flipse, C.A. Muryn and G. Thornton, Phys. Rev. B **46,** 19 (1992) 12877.

[17] P.W. Murray, N.G. Condon and G. Thornton, Phys. Rev. B **51,** 16 (1995) 10989.

[18] G.E. Poirier, B.K. Hance and J.M. White, J. Vac. Sci. Technol. B **10,** 1 (1992) 6.

[19] W. Weiss, A. Barbieri, M.A. Van Hove and G.A. Somorjai, Phys. Rev. Lett. **71,** (1993) 1884.

[20] H.C. Galloway, J.J. Benítez and M. Salmeron, J. Vac. Sci. Technol. A **12,** 4 (1994) 1.

[21] C.A. Ventrice, T. Bertrams, H. Hannemann and A. Brodde, Phys. Rev. B **49,** 8 (1994) 5773.

[22] N.D. Lang, Phys. Rev. B **36,** (1987) 8173.

[23] M.B. Salmeron, D.F. Ogletree, C. Ocal, H.-C. Wang, G. Neubauer, W. Kolbe and G. Meyers, J. Vac. Sci. Technol. A **9,** (1991) 256.

Chapter 6 Electron Scattering Quantum Chemistry Calculations for the FeO/Pt(111) system

6.1 Introduction

The real space information provided by scanning probe microscopy has already been extremely important in the field of surface science. However, a large portion of the observations are only qualitative. One major improvement necessary to advance the field of STM is the development of theoretical methods for image interpretation. This would allow the detailed structural analysis in real space that is now mostly available from diffraction techniques that average over large areas of a surface. Furthermore, numerous experiments have shown that simple approximations of the tunneling process quickly become inadequate. Since the usefulness of STM is clearly limited by how accurately surface structural information can be extracted from images, a more detailed understanding is necessary.

In spite of considerable efforts towards STM calculations, the problems remain difficult. Some of the difficulties include accounting for tip structure which is not usually measured directly and is only seen in its effect on the STM images. Also, the tunneling process is essentially quantum mechanical in nature and requires calculational methods that take this into account. While a number of calculations exists for metals and semiconductors, to our knowledge, none exist for metal oxide surfaces; yet understanding how STM images relate to topography and electronic structure remains just as important for these systems.

Several experimental results have demonstrated that oxygen chemisorbed on metals [1, 2] often appears as a depression in the STM images although it is higher in topography suggesting that tunneling on oxide surfaces might show similar behavior. This is supported by calculations for the case of oxygen on metals [3] but similar results for an oxide as opposed to a chemisorbed system are not available. In an attempt to better

understand the tunneling process from an oxide surface and to learn more about the FeO/Pt(111) interface in particular, electron scattering quantum chemistry calculations of the tunneling current have been undertaken for this system.

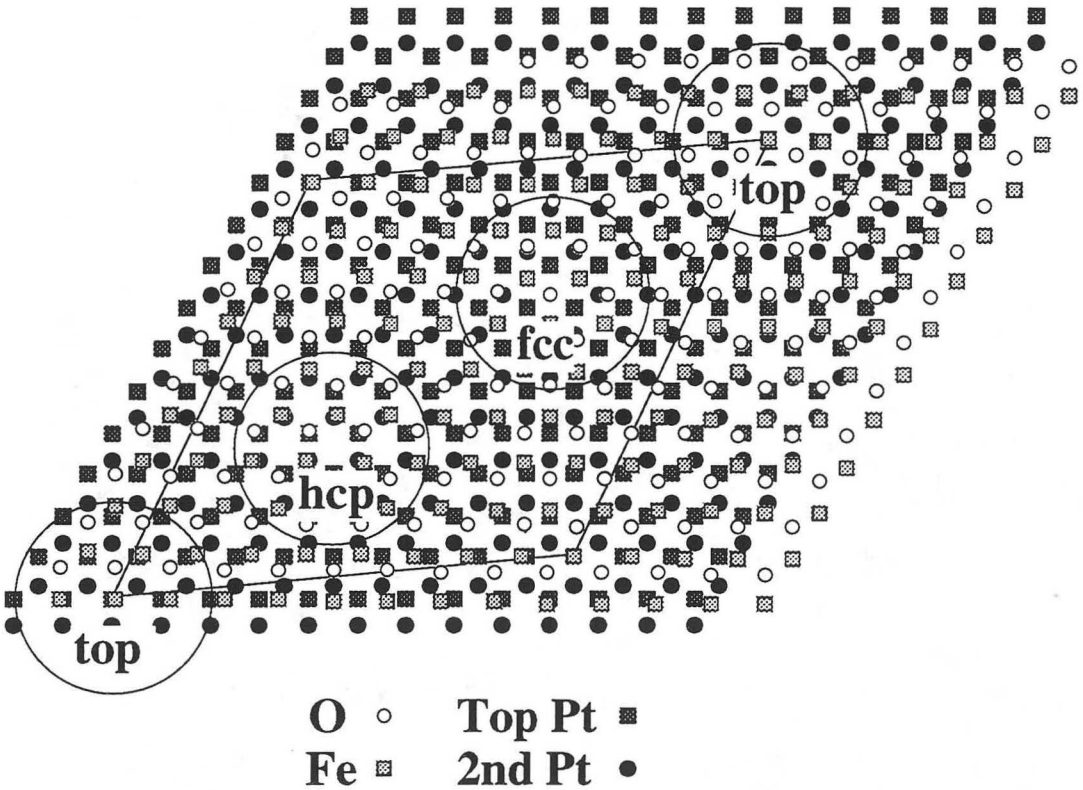

Figure 6.1 Model FeO/Pt(111) with site labels

Different configurations of the FeO overlayer relative to the Pt substrate occur due to the lattice mismatch as illustrated in this figure. The three sites with highest symmetr are labeled (top, hcp, fcc). Bridge sites are found between any two high symmetry sites.

6.1.1 Experimental

The model presented in Fig. 6.1 for the FeO/Pt(111) bilayer is labeled by the approximate sites of the FeO lattice with respect to the platinum. As is seen in the

illustration the FeO layer occupies a variety of configurations with respect to the close packed surface of the Pt crystal. STM data [4] shows that the structure has a small rotation (0.6 Å) with respect to the Pt lattice and a 3.1 Å lattice constant. From X-ray photoelectron diffraction experiments [5] it has been determined that the Fe-O bond distance is 1.90 Å and ascertained that the surface is oxygen terminated. The preferred stacking of the oxygen with respect to the Pt has also been determined and is as shown in Fig. 6.1.

Although the detailed structural models and experimental results for FeO/Pt(111) have been discussed previously in Ch. 3, the important details of the STM images are summarized here. Both a short (3.1 Å) and a long (26 Å) periodicity are observed in what is commonly called a Moiré pattern. The long range periodicity has two components. The first modulates the magnitude of the average current and the other modulates the atomic corrugation amplitude. (An experimental current image is shown in Fig. 6.7.)

6.1.2 Calculation goals

While this system is clearly not a very simple oxide surface, many of the structural parameters have been determined experimentally. This is not the case for most oxide surfaces which makes this oxide monolayer a strong candidate for performing STM calculations to better understand the imaging of an oxide. The thin oxide layer on a metal also allows tunneling with a very small bias voltage as no band gap is observed and the bulk states are simply those of Pt. In addition, the Moiré type of image that is observed for FeO/Pt(111) due to the mismatch between substrate and overlayer lattice constants has been seen for other systems [6, 7] yet it is not clear what correlation exists between this type of image and the topography of the surface. The goal in performing calculations is to understand the origin of both the short and long range corrugations that are observed experimentally to verify the validity of the model used for the calculations. The results

will then allow an understanding of how the tunneling current depends on the structural parameters of the FeO layer, including the stacking of the iron and oxygen with respect to the fcc Pt(111) surface and the Fe-O bond distance. It will also allow an understanding of how the tip structure and tip atom termination affect the image.

The results should determine whether the maxima observed in the image correspond to the positions of the iron or oxygen atoms and what areas on the experimental image correspond to the top, fcc, hcp, etc. configurations of the FeO bilayer with respect to the Pt. While it is tempting to relate the average tunneling current variation to a simple buckling of the surface layer, no experimental evidence supports that assignment. More importantly, the goal is to understand what is the origin of the variation in tunneling current corrugation and amplitude as the stacking is changed across the different portions of the large Moiré unit cell and what orbitals of the surface atoms are contributing the most to the electronic states important for tunneling. Due to the large number of parameters in this system a quantitative fit of the structure is not possible at this time but as will be demonstrated here, the calculations provide insight into the origins of the experimentally observed images.

6.2 Method

The Electron Scattering Quantum Chemistry method was first developed by Sautet and Joachim [8] and the computer programs used for this work were written by P. Sautet. The method consists of considering electron tunneling as a scattering problem. The amplitude for electrons in one sample to be scattered into another (or be reflected back) is calculated within the scattering formalism. The Hamiltonian is projected into a basis set consisting of the atomic orbitals of the chosen positions of tip and surface atoms. The matrix elements for the propagators that are used to build the scattering matrix are calculated in the framework of extended Hückel theory. The tip and substrate are described atom by atom with the boundary conditions that both sides of the gap are semi-

infinite in z (perpendicular to the surface) and periodic in x and y. Both tip and sample consist of the same bulk structure and the overlayer or adsorbates are added to the sample side in well specified atomic positions. A cluster of atoms of a specific chemical composition is added to the tip surface to make the tunneling apex. The periodic boundary conditions require that the tip is actually repeated in x and y and thus the unit cell must be large enough to prevent tip-tip interactions (> 10 Å).

Each atom is described by an orbital basis set consisting of the outermost atomic orbital wave functions. For the bulk of the tip and sample, only an s-wave description is used for simplicity as the deeper layers do not contribute significantly to the tunneling process and function mainly as electrodes or Bloch wave sources. The atoms in the tip cluster and first surface layers are described by full s, p, and d angular orbital functions and a linear combination of two exponentially decaying radial functions (known as a double zeta description) [9].

The probability for tunneling is described as a scattering matrix and the conductance is calculated using the generalized Landauer formula. The matrix elements are calculated with the extended Hückel theory which assumes that the off diagonal Hamiltonian matrix elements are proportional to the overlap of atomic orbitals. Calculation of the scattering matrix uses a propagative technique. The wave functions and the matrix elements are approximate and the calculation of the tunneling current from the conductance uses a low voltage approximation, but the calculation of the scattering matrix is exact and includes multiple scattering effects.

One major advantage of the method is that both the substrate and tip are described atom by atom allowing calculations of complicated structures and variations in the tip structure and chemical identity. The theory has been successfully applied to chemisorbed atoms and molecules on metals and correctly describes the image shape as a function of bonding geometry. Systems investigated include benzene, CO and O on platinum and rhodium [10, 11] and sulfur on rhenium, platinum, and molybdenum surfaces [12-14]

The Fermi level and bulk electronic parameters are taken from calculations fitting bulk properties and other electronic parameters and are found in standard references and previous fits with experiment. The iron and platinum parameters in particular are taken from an Fe-Pt alloy calculation which should also be appropriate here. Preliminary tests are conducted to verify that no anomalous results occur for reasonable variations of the electronic parameters.

6.3 Models

The model used for the present ESQC calculational method must have the same bulk for sample and substrate. In this case, the bulk sample is Pt and the experimental tips are Pt-Rh alloy wire so Pt is chosen as the bulk. Tips are composed of a trimer of Pt atoms with a single tip atom that is either Pt or O, or just the Pt trimer is also used. (A carbon atom at the tip apex produced qualitatively similar results to O in all the calculations performed.) The boundary conditions require that the set of atoms chosen for the calculation is periodically repeated in x and y (parallel to the surface) so working with the entire unit cell at one time would require a large number of atoms (~700). To avoid this problem, small unit cells (~150 atoms) that each mimic a portion of the large unit cell are used, with the substrate and overlayer having the same lattice constant.

The FeO layer lattice constant is 3.1 Å [4] and the bulk Pt lattice has a value of 2.77 Å, which is smaller by 10.6%. In order to simplify the calculation it is desirable to construct a unit cell with the smallest dimensions. Possibilities include artificially expanding or contracting one of the lattice constants so that they match or to pick some intermediate value that produces a smaller unit cell than the experimental one of 26 Å. The best and simplest solution is to expand the Pt lattice to a value of 3.1 Å since it is located two layers farther away from the tip and its structure has a reduced effect on the tunneling current (as has been tested quantitatively). Therefore, the FeO which comprises the first two layers is kept at its correct x-y lattice constant. The Pt tip trimer is kept at the

bulk Pt distance of 2.77 Å and the tip atom-trimer bond is chosen based on experimental results, so that the situation is symmetric with respect to the tunneling gap with two layers on each side kept at the correct bond distances. Thus, the interactions in the tunneling gap are not modified with respect to the real system. The model is shown in Fig. 6.2. The local bonding geometry of the Fe with respect to the Pt is studied piecewise by choosing four high symmetry configurations where the FeO layer is in the fcc, hcp, top or bridge sites with respect to the Pt. The four configurations are shown in Fig. 6.3. The continuous variation of the Fe registry with respect to the Pt lattice in the real system is hence modeled in a discrete way by the different positions of the FeO overlayer on an expanded matching Pt substrate. The variation across the unit cell is studied by performing calculations on this set of four different configurations and systematically varying parameters for all of them.

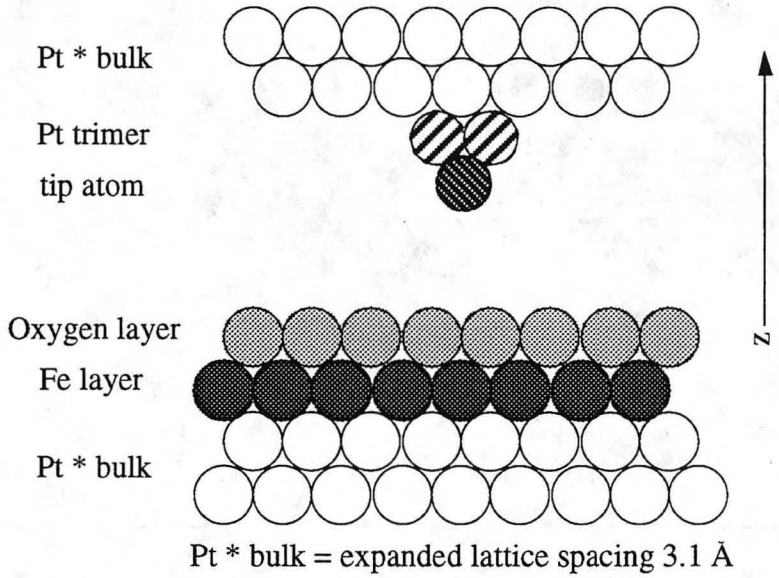

Figure 6.2 ESQC calculation model

The components of the atomic layers used for ESQC calculations.

In an attempt to compensate for the expanded lattice, the Pt-Pt interaction was varied by changing the coefficient of the Pt atomic orbitals to keep the Pt-Pt interaction equal to the bulk value. Again, this had only a very small effect on the calculated results further supporting our claim that the effect on the tunneling is weak. For the purposes of the ESQC model, the Pt substrate primarily functions as a Bloch wave source for electrons tunneling through the gap. However, as will be shown here changing the configuration of the FeO layer with respect to the Pt(111) does have an effect on the current corrugation and amplitude. The local arrangement of the FeO with respect to the Pt in the large unit cell is kept by changing from one to another of the different configurations that are depicted in Fig. 6.3.

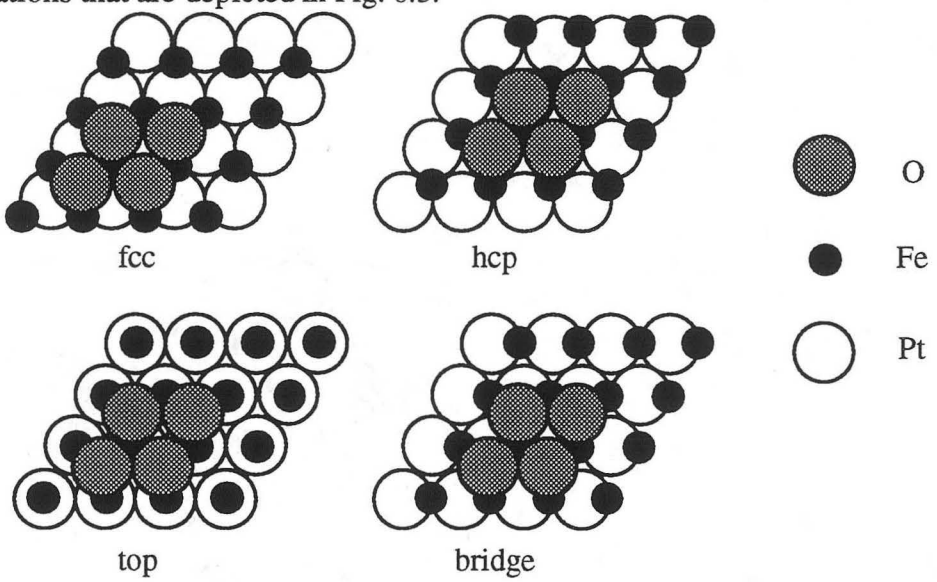

	fcc1	fcc2	hcp1	hcp2	top1	top2	bridge
Oxygen layer	B	A	C	C	A	B	*
Fe layer	A	B	B	A	C	C	#
Pt * bulk	C	C	C	C	C	C	C
	B	B	B	B	B	B	B
	A	A	A	A	A	A	A

Figure 6.3 ESQC configurations

The different stacking configurations used for the ESQC calculations in this study.

Using the expanded Pt lattice substrate, the ESQC calculations were performed in 12.4 Å x 12.4 Å cells composed of unit cells of the FeO lattice periodicity of 3.1 Å. These cells then consist of the bulk Pt and a layer each of Pt, Fe, and O with the full orbital description. Four configurations are considered labeled fcc, hcp, top, and bridge by the positions of the O-Fe-topmost Pt layers and the model is summarized in Figs. 6.2 and 6.3. For the high symmetry configurations (top, fcc, and hcp) there are two possibilities labeled 1 and 2. Those labeled 1 are due to the oxygen stacking as determined experimentally by XPD [3]. The FeO layer is thus shifted over and up or down in z to adjust to the cell type and the Fe-Pt bond length. This leads to an overall z variation or surface buckling of the FeO layer of 0.44 Å between the top configuration which represents the highest point on the surface and the hcp and fcc hollows which represent the lowest points on the surface. The bridge cell is intermediate at 0.16 Å above the hollow configurations. Assuming no surface buckling would lead to unrealistic Fe-Pt bond distances. The results for top1 and top2 are identical to each other as are the results for fcc1 and fcc2 while the results for hcp1 and hcp2 also form an identical pair. Thus in the following discussions only one of each pair (labeled 1) will be presented. It is important to note that the fcc and hcp designations refer only to the last three layers and not to the position of the Fe with respect to the Pt. The effects of the hollow configurations stacking will be discussed in detail in 6.5.2.1

For the Fe-O bond distance, a value of 1.90 Å as determined by X-ray Photoelectron Diffraction [5] is used. It is important to note that the change in bond distance from a bulk FeO value of 2.15 Å to 1.90 Å is only a 11.6% contraction. However, it produces a much larger change in the Fe-O z distance, from 1.25 Å for the bulk value to a 0.65 Å spacing in z using the XPD value. To see the effect of changes in z, calculations for Fe-O bond distances of 1.8 Å, 1.86 Å, 2.0 Å and 2.15 Å have also been performed and the effect on the images will be described later.

The one structural parameter that has not been measured experimentally is the Fe-Pt distance. The expected Fe-Pt bond length from average metallic radii is 2.66 Å and one possibility is to simply keep the Fe-Pt bond distance always at this value for all configurations. However, this type of hard spheres model does not take into account the fact that the Fe-O bond is strong and therefore the Fe-Pt bond must be weaker, as evidenced by the strong contraction of the Fe-O bond and the formation of the Moiré pattern which indicates the oxide overlayer is keeping its own structure in spite of the underlying substrate. In more chemical terms, the principle of bond order conservation, implies that the Fe-Pt bond is expected to expand slightly for highly coordinated sites. Therefore a value of 2.76 Å was selected for the fcc and hcp hollows and for the bridge configurations. By the same argument the top site, where the coordination is lower should have a reduced bond distance. A value of 2.56 Å was chosen for the top configuration. Although this variation of the Fe-Pt distances does make small quantitative changes it does not alter the trends that are discussed in this work.

These values of the Fe-Pt bond were also found to show the best agreement with the experimental data. Although a precise fitting was not conducted, reducing the Fe-Pt bond for the fcc and hcp configurations causes the average current for the two configurations to become further apart until there is no overlap in the current values for the fcc and hcp cells. Experimentally the range of values observed for the different tip positions across the large Moiré unit cell have a small overlap. Expansion of the bonds beyond the chosen values by more than 0.1 Å was not attempted.

6.4 Results

6.4.1 Topographic calculations

The first series of results are presented in the bar graph shown in Fig. 6.4. Each column of data corresponds to a specific configuration (top, fcc, hcp or bridge) and the three rows are for different tip terminations as shown at the side of the graph. The z scale

is defined as the distance between the last atom(s) of the tip and the plane of the O atoms in the fcc or hcp surface. The calculations consist of determining the tip z values such that the current is 1 nA at a bias voltage of 30 mV. This calculation is done at three high symmetry points on the surface for each cell type (top, fcc, etc.) Then the minimum and maximum tip z values for each calculation are used to make the graph. Bars are drawn between the maximum and minimum z heights found for each configuration. (The positions of the maxima and minima with respect to the surface atoms will be discussed later.) Thus the length of the bars represents the calculated corrugation in one section of the image the lines connecting the midpoints of the bars follows the corrugation of the long range periodicity. The location of the labels (top, fcc, br, hcp, top) in the x-axis is the same as that found along the long diagonal of the unit cell (see Fig. 6.1). For comparison, the geometric buckling of the different FeO configurations (height of the O atoms) is also shown at the bottom of the graph.

For both the Pt and O single atom terminated tips, the atomic scale corrugations are on the order of 0.1-0.3 Å for a gap value of 30 MΩ (1 nA at 30 mV). The small periodicity (3.1 Å) corrugation is dependent on the configuration and shows the trend hcp $\leq$ fcc $\approx$ br < top for all three tips. However the trend in average z amplitude (with a 26 Å periodicity) is fcc $\approx$ top < br < hcp for the Pt tip and fcc < hcp < br $\leq$ top for the O tip and fcc < top $\approx$ hcp $\approx$ br for the Pt3 tip. As we can see this is quite different from the surface topography which has the trend fcc = hcp < br < top. Although, the sequence of average heights for the O-tip is similar to that of the surface topography, the magnitude is not. There is only a 0.13 Å change in average z whereas the surface topography has a corrugation of 0.44 Å for our model. For the Pt tip the ordering is not topographic with the fcc and top configurations giving the same average z in spite of the 0.44 Å geometric difference between them. Finally, all tips show a distinction between the fcc and hcp configurations which is not a result of topography as these are at equal heights in our models.

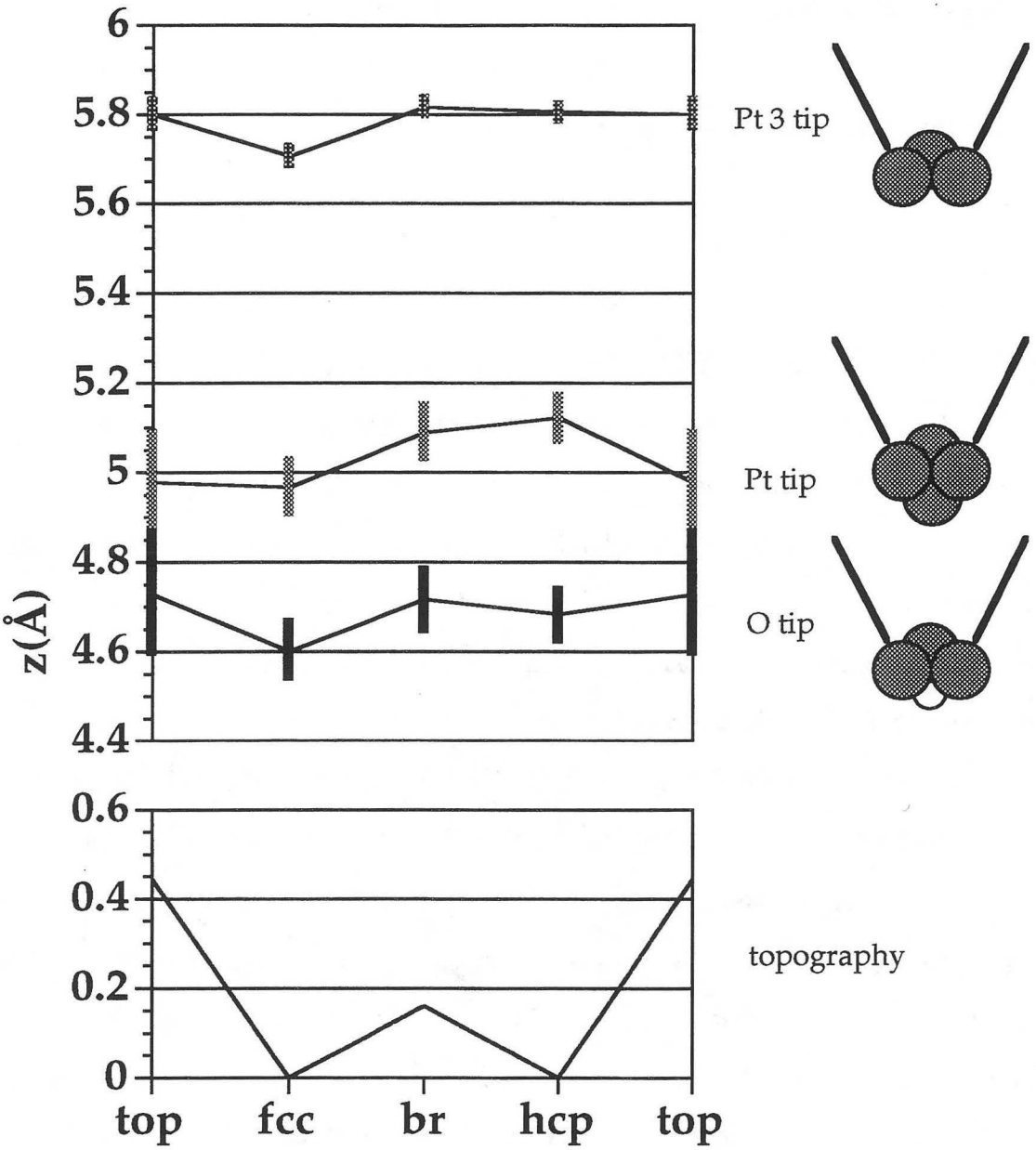

Figure 6.4 Topographic calculation - Pt, O and Pt3 tips

The bars represent the atomic corrugation and z values for each of the configurations shown along the x-axis, at I = 1.0 nA and Bias = 30 mV. The lines connecting the midpoints of the bars correspond to the calculated long range corrugation. The z scale is the distance from the center of the tip apex atom(s) to the fcc oxygen plane in the surface and the topography of the surface is shown at the bottom for reference.

The Pt3 tip gives an increased overall z distance (by 0.7-0.8 Å compared to the single Pt tip) and the atomic scale corrugations (bar lengths) are smaller than the single atom tips by a factor of ~3-4. The maximum z for the Pt tip is always located over an O atom on the surface and the minima over an Fe while for the O tip, the maximum and minimum points are reversed so the experimentally observed maxima cannot be simply assigned to an atomic position. In general, the calculation reproduces the major features of the experimental data, namely the change in atomic scale corrugation across the large Moiré unit cell and the overall amplitude variation. A more detailed comparison of the calculations to experiment will be discussed in the following section where both calculated and experimental images are shown.

6.4.2 Current results

Many experimental images are obtained in the current mode with the tip held at a fixed but unknown height. Therefore, the values of the current as a function of substrate tip spacing have also been calculated to match with these images. The information extracted from these images is similar to that obtained from topographic calculations although some features of the system become clearer in this mode. The same four types of FeO/expanded Pt configurations are used as before. For each one, the current as a function of z is calculated for the tip positions that correspond to the maximum and the minimum current in a current image. These extreme values of the current are found for the tip above an Fe atom or an O atom giving the minima/maxima and maxima/minima for the Pt/O tips respectively. Plots are shown of the average current and the corrugation, $\Delta(\log I)$, for three configurations in Fig. 6.5. Since the current and corrugation are decreasing exponentially both should have an exponential decay with distance. Thus, both the average current and $\Delta(\log I)$ should appear linear on a log scale. The same trends as noted for the topographic data are reproduced. The average current for the different cells does not follow the topography. In fact, there is a contrast change for the

O tip with the top configuration becoming lower than the hcp configuration at a tip height above the fcc O of ~4.2 Å. A similar contrast change is observed for the Pt tip with the top configuration becoming lower than the hcp configuration for tip height values lower than 4.7 Å. The bridge configuration is left off for simplicity. The value of Δ(log I) for the fcc and hcp configurations is very similar showing that the only difference between the two configurations is that the current is higher for hcp than fcc but the corrugation and the z dependence of the two are essentially the same.

While this representation of the data is useful for comparing to a current (or constant height) image it hides the fact that the relevant parameter for tunneling is the absolute distance between the tip and sample. The top configuration has a smaller separation from the tip for the same z due to the surface buckling, so the z scale for the top configuration should be shifted lower by 0.44 Å to see the contributions to the current other than from the geometrical height due to the buckling of the FeO. The curves are then replotted in terms of constant tip-surface separation as shown in Fig. 6.6. Two important conclusions are apparent. The first is that although the Pt tip and O tip give different long range corrugations (bottom panels), the trends are actually very similar. Both show the trend, top < fcc < hcp, for the average current values.

The second important revelation of these plots is that the Δ(log I) differences between the top and 3-fold hollow configurations (fcc, hcp) almost disappears when the effect of the topography is removed (Fig. 6.6). The exponential decrease in Δ(log I) is only ~15% faster for the top than for the fcc or hcp. This is true for both tips but since the oxygen curves have a smaller overall decrease the difference appears less. The second point implies that there is a simple relationship between the surface topography (or tip-surface separation) and the atomic scale corrugation: as the tip-surface separation decreases the atomic scale corrugation is increased consistently across the surface.

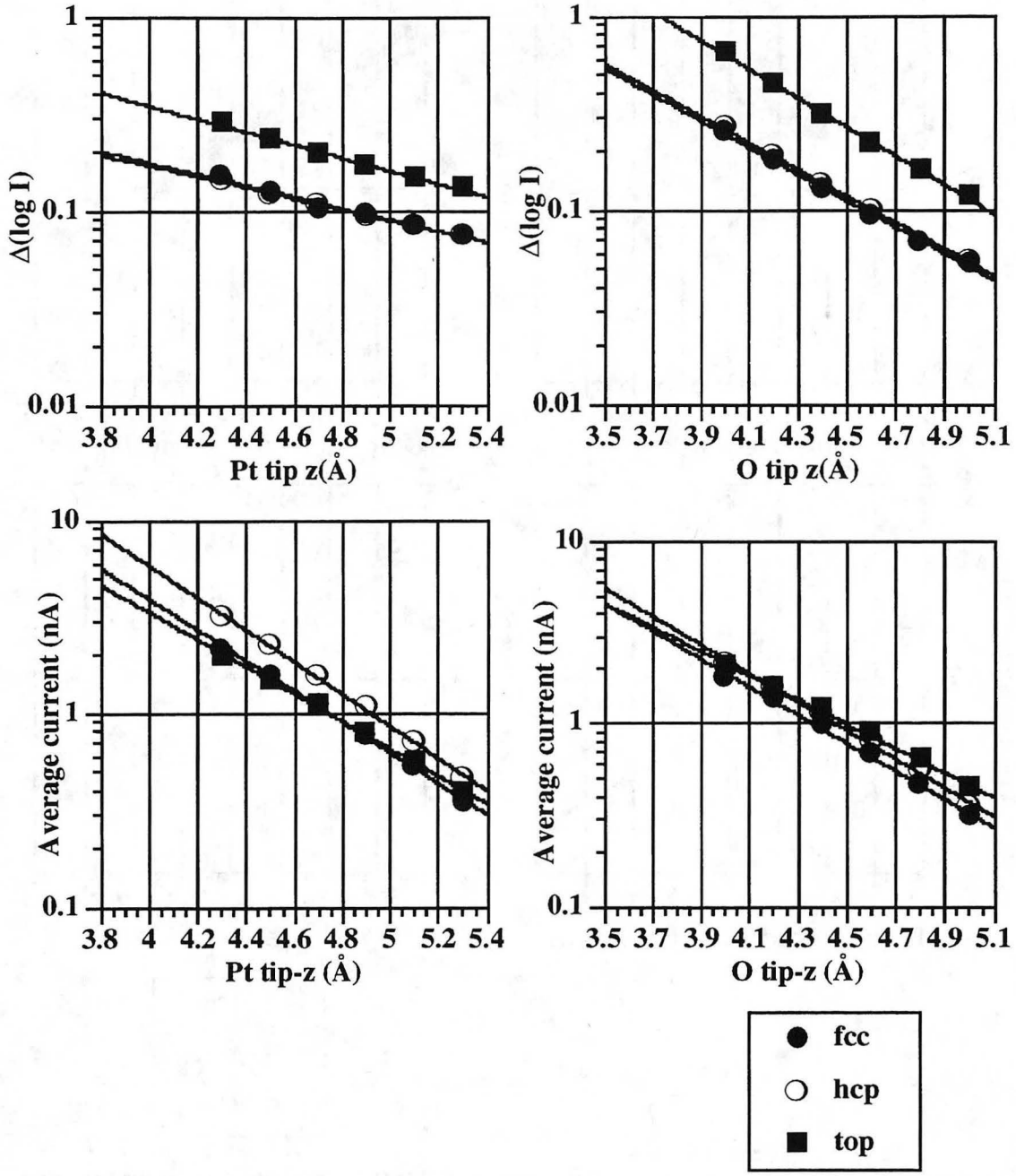

Figure 6.5 Average current and Δ (log I) vs. tip z value

Δ (log I), or the relative corrugation and the average current values for three configurations are plotted. The Pt tip results are on the left and the O tip results are on the right. While the Δ (log I) results show the same trend, the average currents have a different ordering for different tips and show a variation with tip z height.

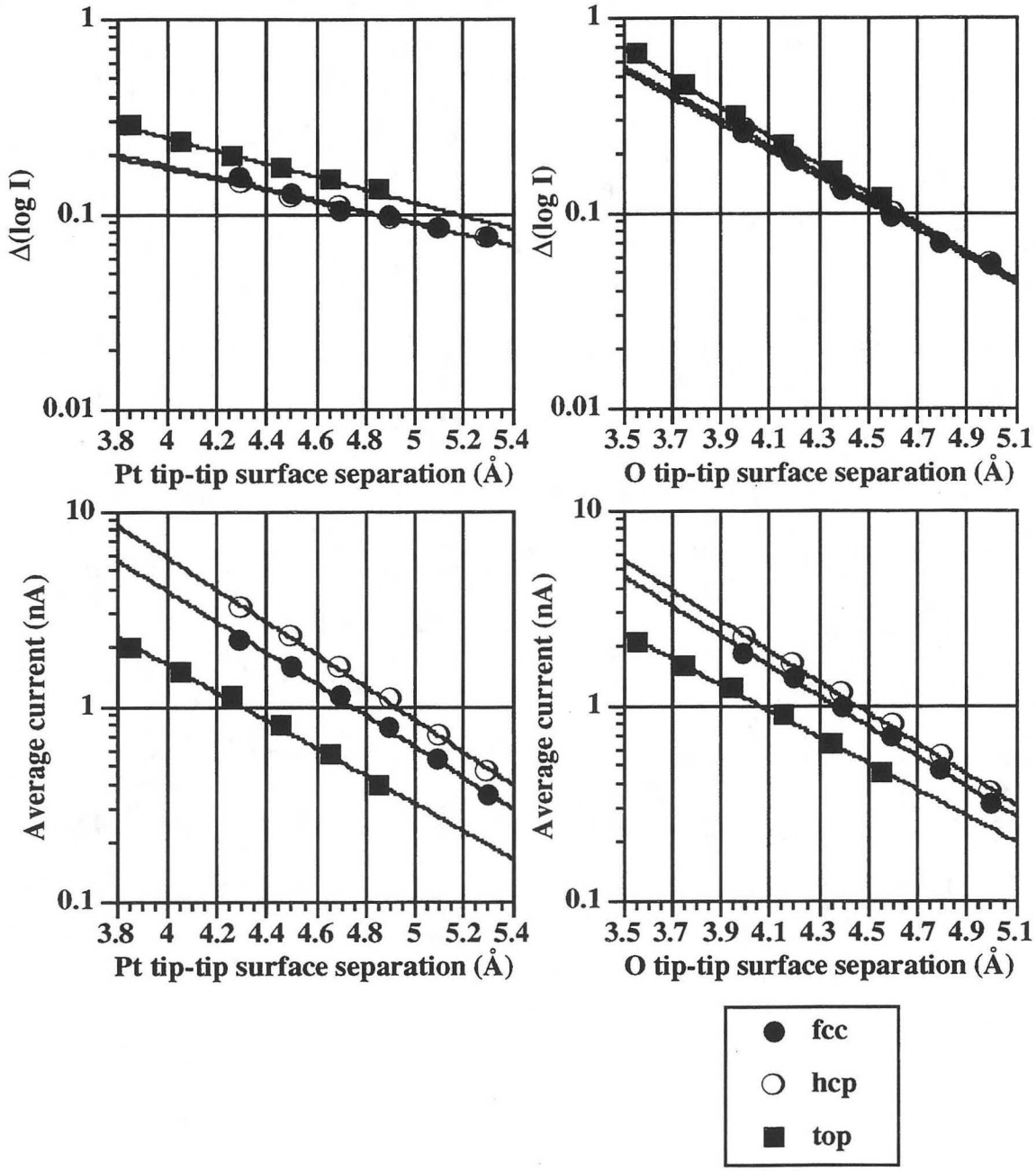

Figure 6.6 Average current and Δ (log I) vs. tip-surface separation

The same graphs as in Fig. 6.5 are replotted as a function of tip-surface separation by shifting the top configuration by 0.44 Å lower in z. The average current trends are now identical for the two tips. The Δ (log I) results are almost identical (only a 15% difference in exponential coefficient) for the three configurations but different for each tip.

This would be more difficult to see in topographic data as the tip adjusts to keep the current constant, but is simple for the case of current mode imaging or calculations where the tip height is not changing with respect to the substrate, so the only change in tip surface distance is due to the buckling. A current image can then be simply interpreted that the regions of highest atomic scale corrugation correspond to the regions closest to the tip, or highest topography. This does not account for the entire corrugation change as evidenced by the fact that the $\Delta(\log I)$ curve for the top does not exactly match the curves for the hcp and fcc even after removal of the effect of FeO buckling. The remaining small corrugation differences must then be due to electronic effects due to the different configurations. In spite of the fact that for topographic images the situation is more complicated as the tip will move to maintain constant current, the atomic corrugation still gives a more consistent picture of the topography. As is seen in Fig. 6.4, the top does show a higher atomic corrugation than the hollow configurations consistently for all tips. However, the hcp has a smaller corrugation than fcc only because the current is higher and hence the tip-surface distance is increased and this difference is not due to a geometric height difference.

Finally, an experimental current image is shown alongside with calculated images for each of the four types of cells (Fig. 6.7). As was detailed above, the highest corrugation is assigned to the top configuration while the other areas of the image are assigned to the fcc and hcp configuration by symmetry and by the prediction that the hcp configuration will have a higher current. The agreement with the experimental image is remarkably good. The top configuration area has the lowest minimum current values in better agreement with the Pt tip predictions than with those from an O tip. The magnitude of the corrugation suggests a single atom terminated tip as well.

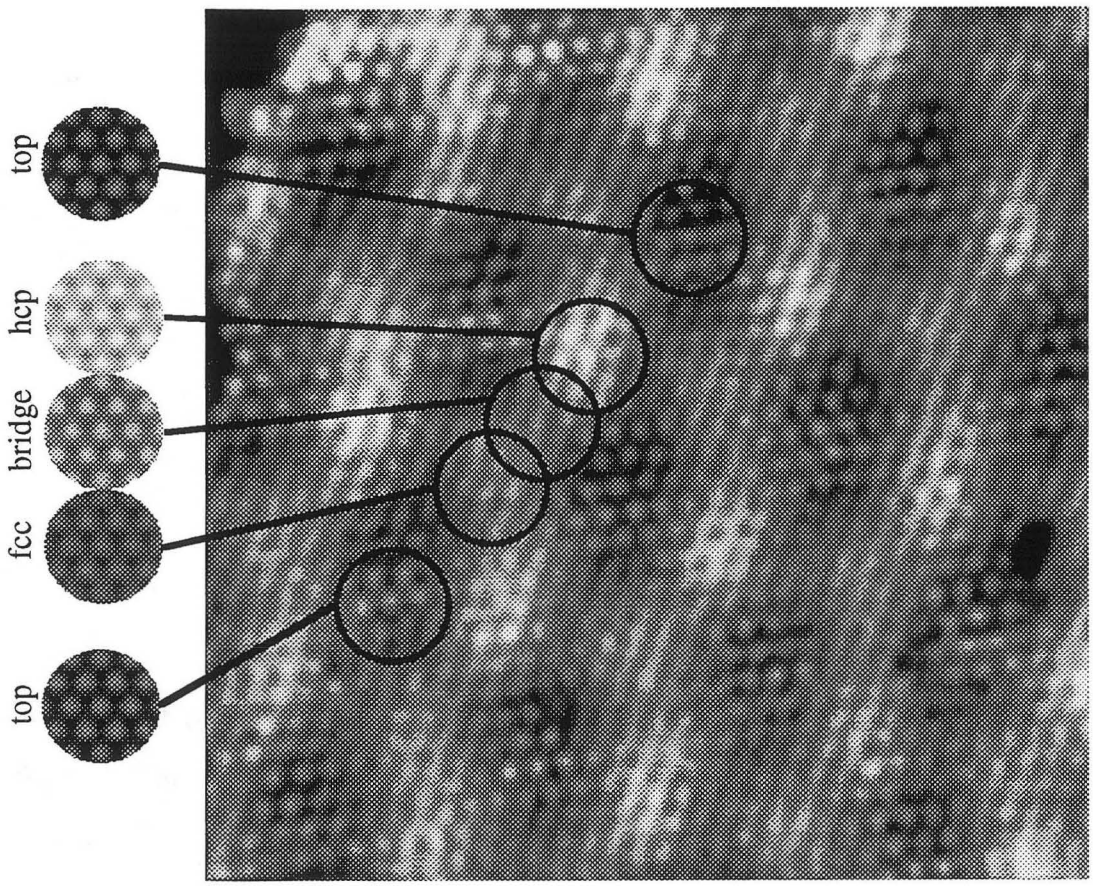

Figure 6.7 Experimental and calculated current images

An experimental image of the surface is shown. The calculated images on the left are matched up with the large unit cell regions. A consistent color scale is used for all calculated images. The ordering of the calculated configurations across the unit cell is in agreement with the model in Fig. 6.1.

The experimental values for this particular image are a corrugation of 0.2-0.3 nA and an average current of 0.7-0.9 nA in the top region and the corrugations in the hollow regions are about 0.1 nA and the average current is 1.1-1.2 nA at the fcc region and 1.2-1.3 nA at the hcp region. The corrugations match a calculated tip z height of 5.1 Å for a Pt tip. For this tip height the difference in the average currents of the top and hcp configurations is 0.3 nA, which agrees with the experimental value with the error bar.

However, the average current of the top configuration predicted theoretically is 0.4 nA compared to the 0.7 nA value observed experimentally. In general, the relative agreement with experiment is quite good, but the absolute magnitude of the current is underestimated. This is likely due to the artificial situation where the correct Pt lattice tip is joined to the expanded lattice bulk and again where the Fe and expanded Pt layers are connected. These can be thought of as extra resistors in the theoretical STM circuit that decrease the average value of the current. The relative values of the corrugations and the relative values of the amplitudes of the current are in remarkable agreement.

6.4.3 Fe-O bond distance

Although the Fe-O bond distance can be measured experimentally, two values have been reported. One is the 1.90 Å value by Kim, et al using XPD [5] and the other is 2.23±0.22 Å by Schedel-Niedrig, et al [15]using NEXAFS. To demonstrate the effect of this parameter on the calculation, both the atomic scale corrugations and long range corrugations were calculated, for various Fe-O bond distances. The results are shown in Fig. 6.8. As can be seen clearly, the atomic scale corrugations fall off to values which would not have been observable experimentally due to the limits of STM resolution for this experiment for bond values of 1.80, 2.00, and 2.15 Å. Only in the range around 1.90 Å is there significant atomic corrugation that is comparable to the long range corrugation as found in the experiment. It should also be noted that for Fe-O bond distances $\geq$ 2.00 Å, the large periodicity has a corrugation of 0.6-0.7 Å similar to that of the surface geometry (0.44 Å) although the magnitude is enhanced. The difference between the hcp and fcc configurations is reduced for the longer Fe-O bonds, with only extremely small differences in amplitude of the corrugation (.0003 Å) or average height (.04 Å). For bond values of 1.8 Å, the topography is again strongly enhanced to 1.2 Å and the difference between the hcp and fcc configurations average values becomes larger, similar to what is observed for decreasing the Fe-Pt bond. Experimentally, the long

range corrugation and atomic corrugations have very similar amplitudes, in line with the calculated values for the Fe-O bond of 1.90 Å and are consistent with the value reported by XPD experiments. However, a simultaneous fitting with other structural parameters would be necessary to justify a more quantitative test. Since the focus here is primarily on understanding the tunneling gap, a precise fit with experiment will not be attempted at this time.

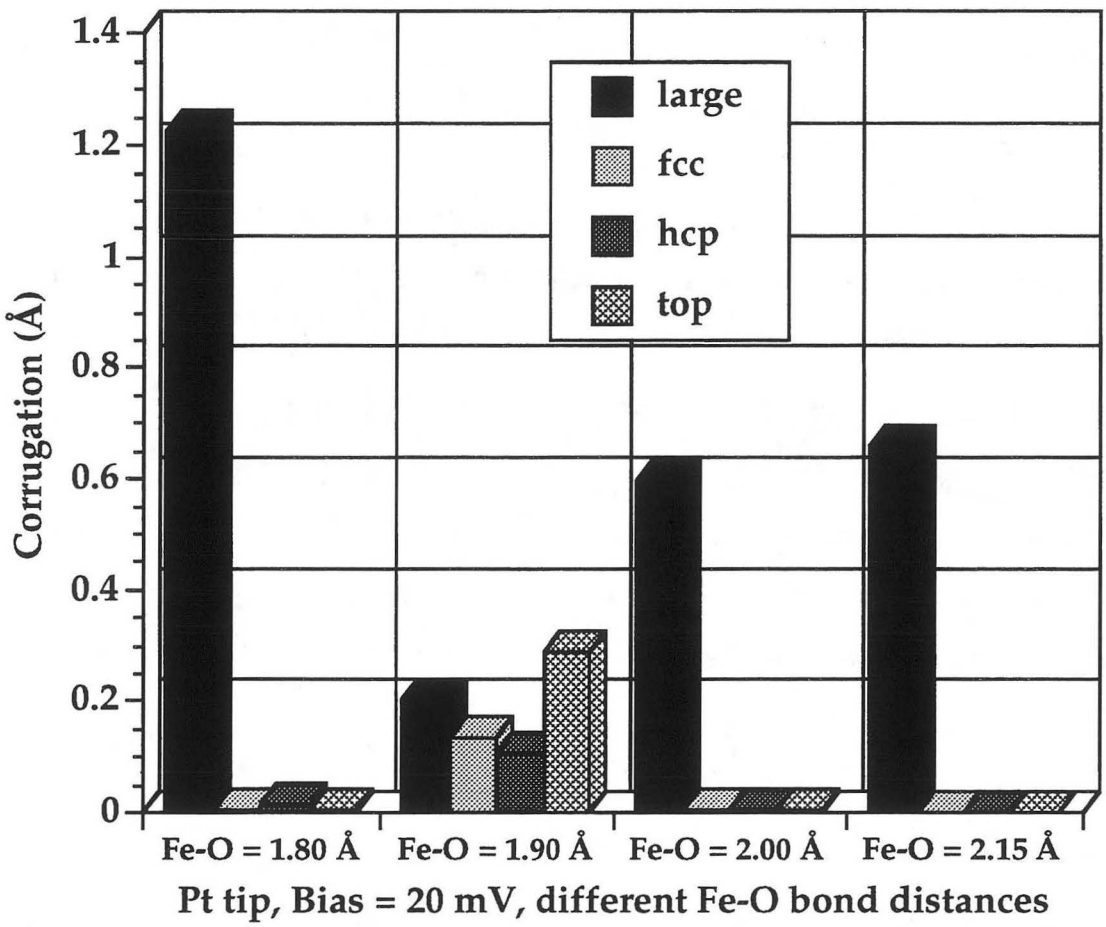

Figure 6.8 Corrugation values for different Fe-O bond distances

The bars represent the corrugations of the configurations labeled fcc, hcp and top, while large represents the corrugation of the large periodicity. Only the Fe-O bond length of 1.90 Å is in agreement with the experimental results, where the large corrugation is the same order of magnitude as the atomic corrugations and all observed corrugations are 0.1-0.5 nA in magnitude.

6.5 Analysis - Decompositions

Several aspects of the STM calculations have been summarized in the previous section but many questions remain as to the origins of these effects. In addition to calculating the entire tunneling current, the framework of ESQC allows some of the matrix elements between the tip and surface to be set to zero, effectively cutting some interactions while leaving others. For example, the contribution of only the oxygen atoms to the tunneling current can be calculated by setting the interactions between the tip and the Fe and first layer Pt atoms to zero.

A calculation of this type for an fcc cell and a Pt tip is shown in Fig. 6.9. The three points in x for each data set are for three points on the surface. For the fcc cell, the first one is above an O atom, the second above a Fe atom and the third point above a first layer Pt atom. The three symbols are for the contributions of the Fe atoms only, the O atoms only and the total current. (Tip sample distance is kept constant.) The most striking feature is that the Fe and O contributions are both higher than the total current. This is due to the quantum mechanical nature of the tunneling problem. The probability amplitudes for tunneling by different paths do not simply sum up to get the total current but may interfere constructively or destructively. Furthermore, the amount of interference can and does change with tip position above the surface, tip structure and of course any surface structural parameters. An interference ratio for the Fe and O currents can be defined as $I_{total}/(I_O + I_{Fe})$ where values < 1 are destructive and values > 1 mean constructive interference.

The role of the destructive interferences between the iron and oxygen contributions is critical in understanding the details of this system. In general, the major effect is to keep the overall tunneling current low, so that the tip is closer to the surface for a particular gap value and thus significant corrugations are observed. It is also important that the contributions have similar values because interference effects are stronger when two values are close in magnitude. (For equal contributions,

$I = \|A\|^2 = \|1+1\|^2$ is between 0 and 4 but the $I = \|A\|^2 = \|1+0.1\|^2$ is only between .8 and 1.2.)

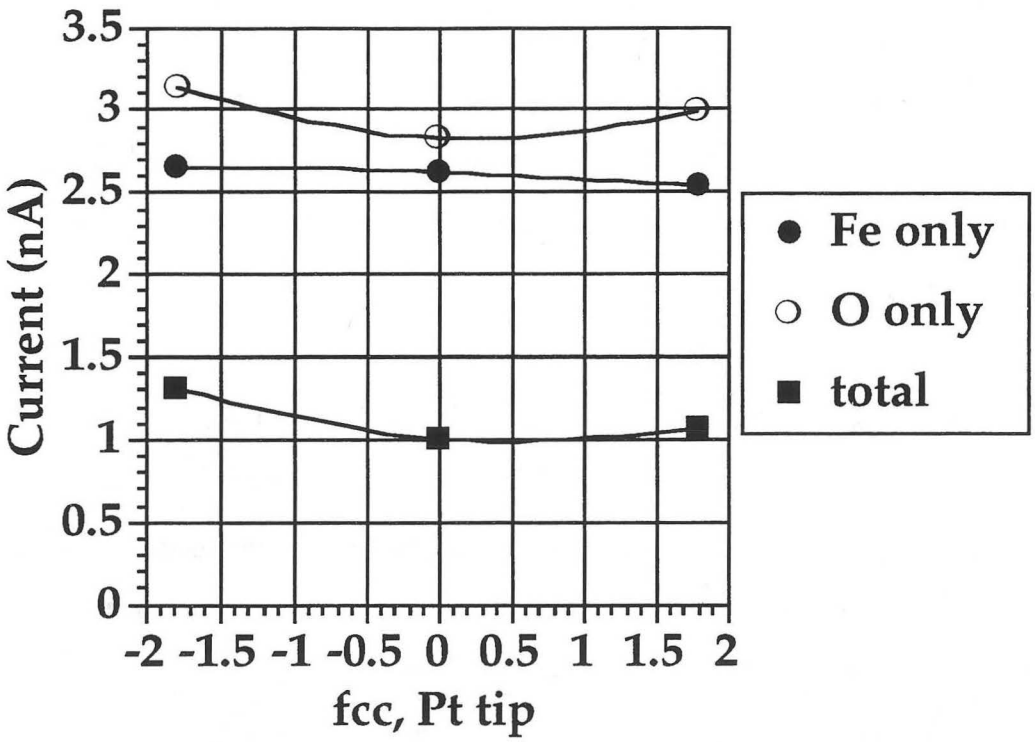

Figure 6.9 Current decomposition, fcc configuration, Pt tip

Surface oxygen and iron individual contributions to the tunneling current are shown along with the total current. The calculation is for the fcc configuration and a Pt tip. The three points are along the high symmetry points of the small unit cell and include the maximum and minimum observed current (1st and 2nd points above an O and Fe atom respectively) as well as the saddle point (3rd point). The Fe and O contributions interfere destructively yielding a total current that is smaller than either contribution.

6.5.1 Maxima positions and image shape

In all cases where the decomposition of the current described above has been attempted, the oxygen contribution is more corrugated and in most cases it has a higher magnitude. The observed corrugation for the total current also follows the same direction as the oxygen contribution. In particular the O p_z orbital can also be shown to have the largest single orbital contribution (Ch. 6.6). Therefore, it is to be expected that the maxima is localized over the O on the surface for a Pt tip. The O tip however shows a minima in the tunneling current when it is located over an oxygen atom. The atomic decomposition of the current explains this apparent reversal.

The O and Fe contributions are again shown along with the total current in Fig. 6.10. In addition, the tunneling current through only the tip atom and through the three Pt atom trimer of the tip base are also calculated separately. This shows that the majority of the current is coming from the Pt3 tip base. This means that the maxima occurs when the tip base is over the oxygen atoms on the surface. Again the maxima is due to the Pt tip-O surface interaction but this occurs when the center of the tip is above an Fe position with the position over the Pt having an almost equivalent value. Thus for both the O and Pt tip, the oxygen atoms on the surface dominate the final tunneling current and corrugation. This also determines the image shape. The basic model is shown in Fig. 6.11.

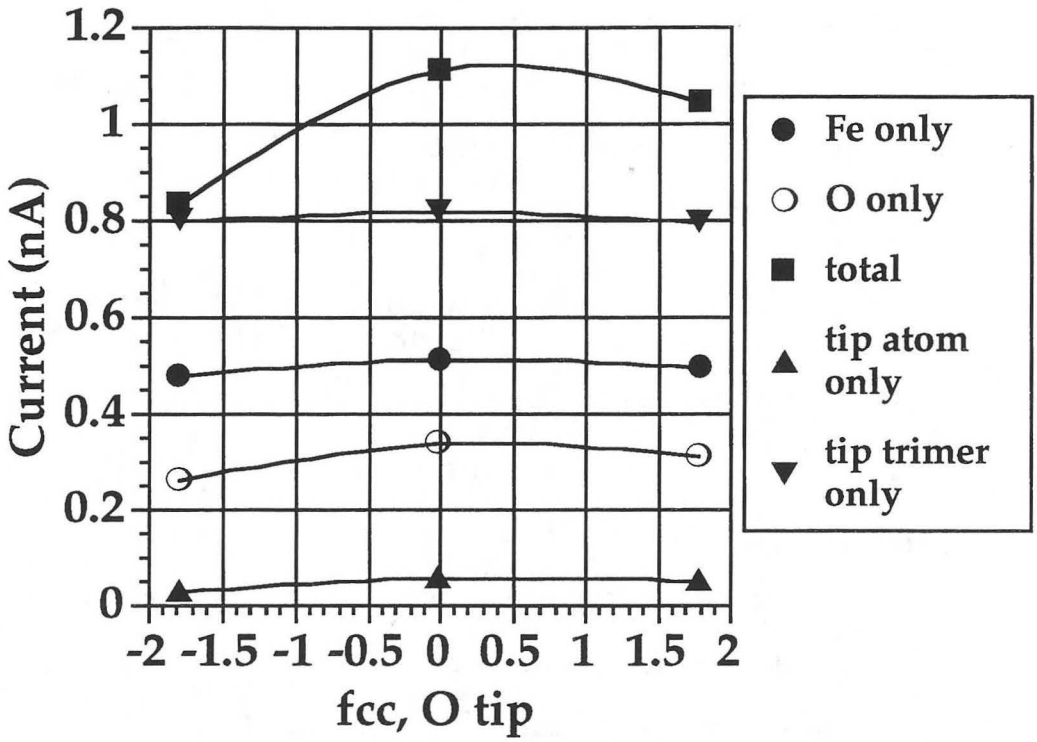

Figure 6.10 Current decomposition, fcc configuration, O tip

Similar decomposition to Fig. 6.9 for the fcc configuration and an O tip. The contribution for the tip atom and tip trimer are also shown independently. The majority of the tunneling current is from the tip trimer in contrast to the Pt tip where most of the current is from the tip atom. The 1st and 2nd points are above an O and Fe atom respectively.

For the Pt tip, the image shape is "ball" like with the maxima over the O and the minima and saddle points being roughly equivalent. For an O tip, the minima are above the O atoms and the maxima and saddle points are roughly equivalent leading to a "honeycomb" shaped image. Both types of images are observed experimentally. The Pt3 tip is qualitatively similar to the O tip except that the atomic corrugations are much smaller. This indicates that although the O tip atom is not dominant for direct tunneling process, it does contribute strongly to the corrugation.

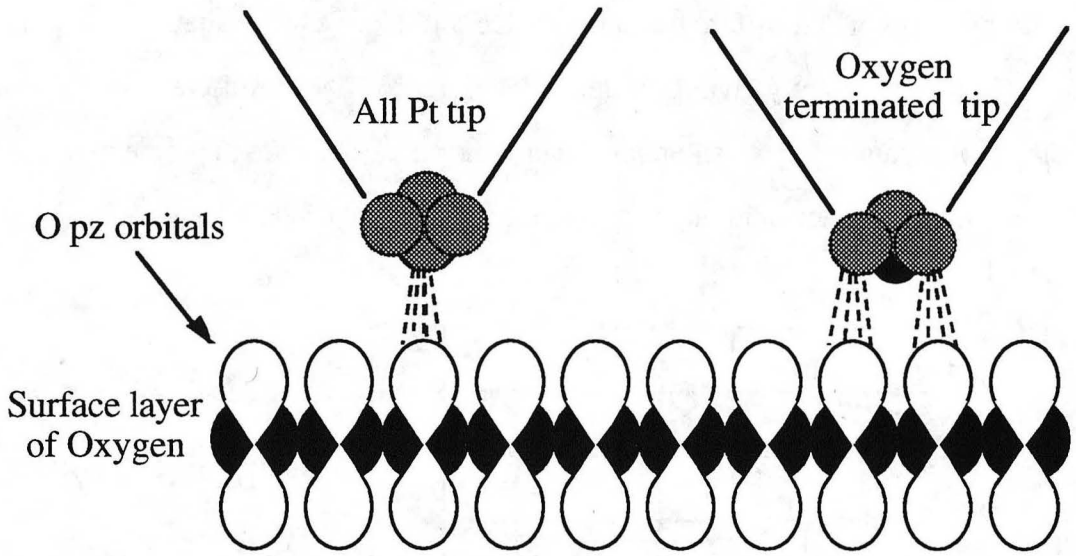

Figure 6.11 Image contrast model Pt vs. O tip

Although the maxima position is shifted for the Pt and O tips, both maxima are due to O(surface)-Pt(tip) tunneling as depicted in the simple model.

6.5.2 Configuration Dependence

6.5.2.1 Fcc vs. hcp

It is important at this point to consider all four possible hollow stackings on the surface. The two stackings where the Fe is in a prismatic configuration (hcp1 and hcp2) and the oxygen atoms are directly over the first layer Pt atoms give the same result while the stackings with Fe in an octahedral coordination (fcc1 and fcc2) and the oxygen atoms are over the 2nd or 3rd layer Pt atoms are also equivalent. The fcc and hcp current decompositions are shown in Fig. 6.12. The iron contributions are essentially identical but the hcp O value is significantly higher for the (~4 nA for the hcp compared to ~3 nA for the fcc). The hcp also has a slightly less destructive interference (Table 6.1) but the majority of the effect is in the increased magnitude of the O current. This suggests two

possible reasons for the difference between fcc and hcp. One is that the Fe is in a different bonding geometry giving a different interference effect or different overlap with the tip. This seems a very small effect because the Fe currents are the same magnitude and the Fe-O interference ratios are very close for the fcc and hcp (see Table 6.1)

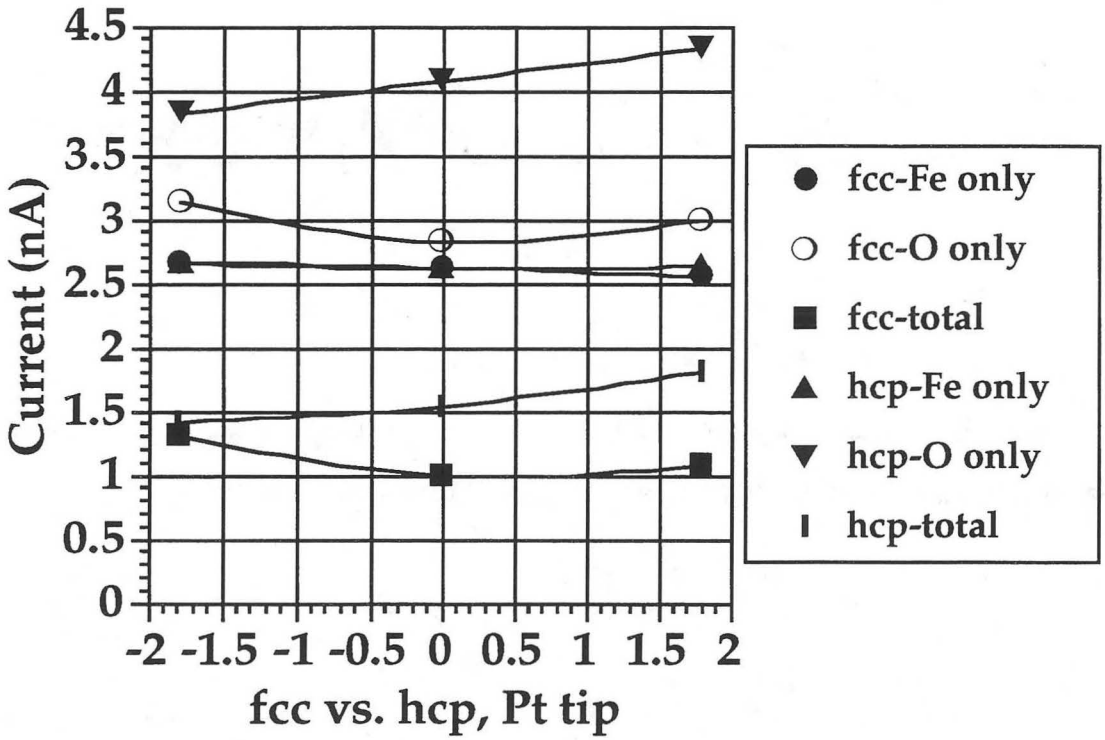

Figure 6.12 Current decomposition, fcc vs. hcp, Pt tip

Comparison of individual current contributions for the fcc and hcp configurations. The Fe contributions are almost identical but the oxygen contribution for the hcp configuration is larger as well as the total current. The tip is above an oxygen atom for the 1st point and an Fe atom for the second point for the fcc configuration and above an oxygen atom for the 3rd point and an Fe atom for the 1st point for the hcp configuration.

Table 6.1 Interference ratios - Pt tip

The interference ratios for three tip positions are shown for three different configurations and a Pt tip. The three tip positions are above an oxygen, iron, and platinum atom. The layer of the Pt atom in the surface is given in parentheses for each configuration.

Pt tip	O	Fe	Pt
top configuration	0.088	0.059	0.063 (2)
fcc configuration	0.225	0.183	0.193 (1)
hcp configuration	0.260	0.217	0.230 (3)

Another possible reason for the different oxygen current in the prismatic arrangement or hcp configuration is simply due to a direct interaction between the Pt and O atoms. The Pt-O distance for the hcp configuration is 2.77 Å while for the fcc configuration it is 3.30 Å. Although 2.77 Å is longer than a Pt-O bond, it is significantly closer than 3.30 Å. Several other results also support this hypothesis. When the Fe-Pt or Fe-O bonds are decreased, the Pt-O distance becomes even shorter for the hcp and the difference between the hcp and fcc average currents increases. Conversely, when the Fe-O bond is increased, the difference between the hcp and fcc configurations is reduced.

6.5.2.2 Fcc vs. top

As was noted earlier most of the differences between the atomic corrugations in different areas of the large Moiré cell are simply as a result of tip surface separation changes. However, the corrugation of the top configuration is still somewhat higher even when this effect is subtracted by keeping the tip-surface separation constant. In addition, the top configuration yields the lowest average current. A plot of the various atomic contributions to the current for the top configuration (Fig. 6.13, z=4.08 Å results) yields the surprising result that the Fe and O individual contributions are higher than the fcc by a

factor of nearly 3 (Fig. 6.9) but the total current is similar to the fcc when the z height of 4.08 Å is used identical to the fcc configuration. However, using the same z height does not keep the tip surface separation constant. Also in Fig. 6.13 is the same calculation for z=4.52 Å which does keep the tip surface height constant. This reduces the Fe and O contributions to similar values as observed for the fcc configuration (3-4 nA) but now the total current is lower (about one half) indicating a more destructive interference for the top as shown in Table 6.1.

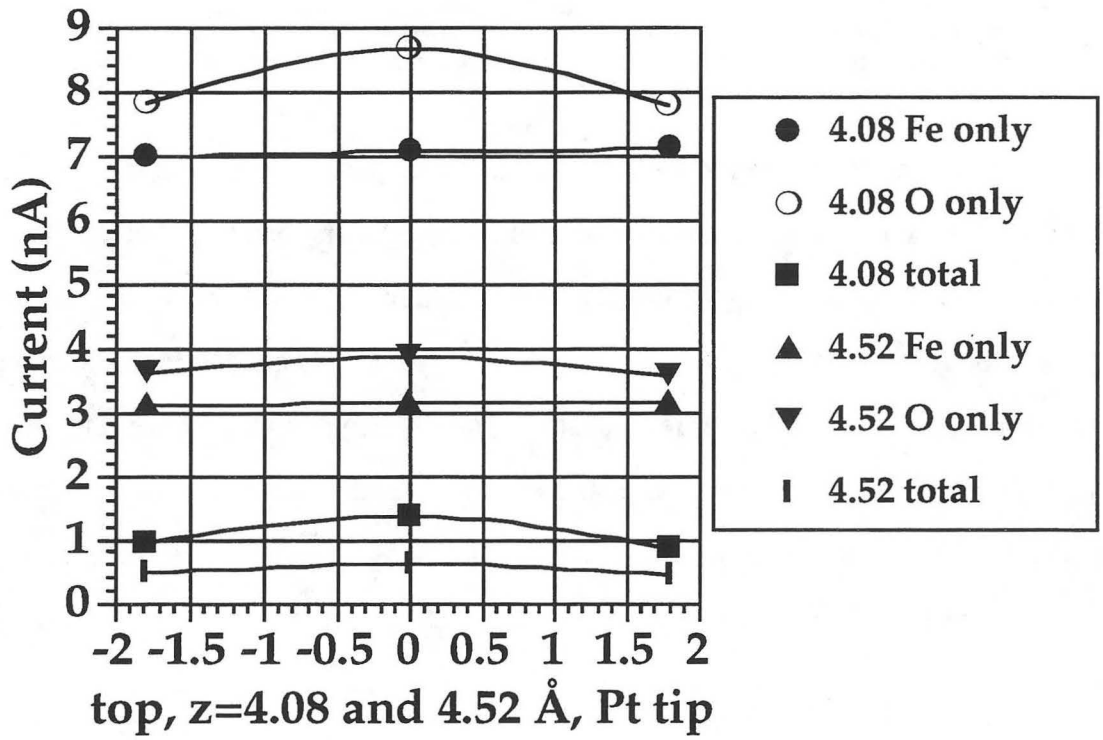

Figure 6.13 Top configuration, Pt tip, z=4.08 and 4.52 Å

For a tip at the same height used for the fcc decomposition (z=4.08 Å), the Fe and O contributions are higher but the total current is similar. However, when the tip-surface distance is kept constant (z=4.52 Å), the Fe and O contributions have very similar magnitudes but the total current is less indicating a more destructive interference in the top configuration. The tip is above an oxygen atom for the 2nd point and an Fe atom for the 3rd point.

The decomposition of the current into Fe and O components for the Pt tip clearly demonstrates how the destructive interference can lead to significant corrugation. The two contributions have similar magnitudes so the destructive interference reduces the overall current leading to a lower tip position which enhances the corrugation of the O component. The interference ratio is also dependent on the tip position across the unit cell as is seen in Table 6.1 by the different interference ratios for the three tip positions over each type of atom in the surface. This causes further corrugation enhancements. This is due to the fact that the O current is corrugated, while the Fe contribution is not and thus the difference between these two currents, which controls the interference strength, depends on tip position.

6.6 Orbital decompositions

As well as calculating the contributions from a single chemical species on the surface, the current due to an atomic orbital can also be calculated individually. Just considering the Fe and O atoms on the surface, there are 13 separate atomic orbitals. For example, the contributions from all the Fe-p_x orbitals can be calculated. Or the orbitals can be grouped by symmetry such as the O-s and O-p_z which have A1 symmetry. This type of calculation is shown for both the fcc configuration and the top configuration. Both calculations are for a Pt tip and the same tip-surface distance (Fig. 6.14).

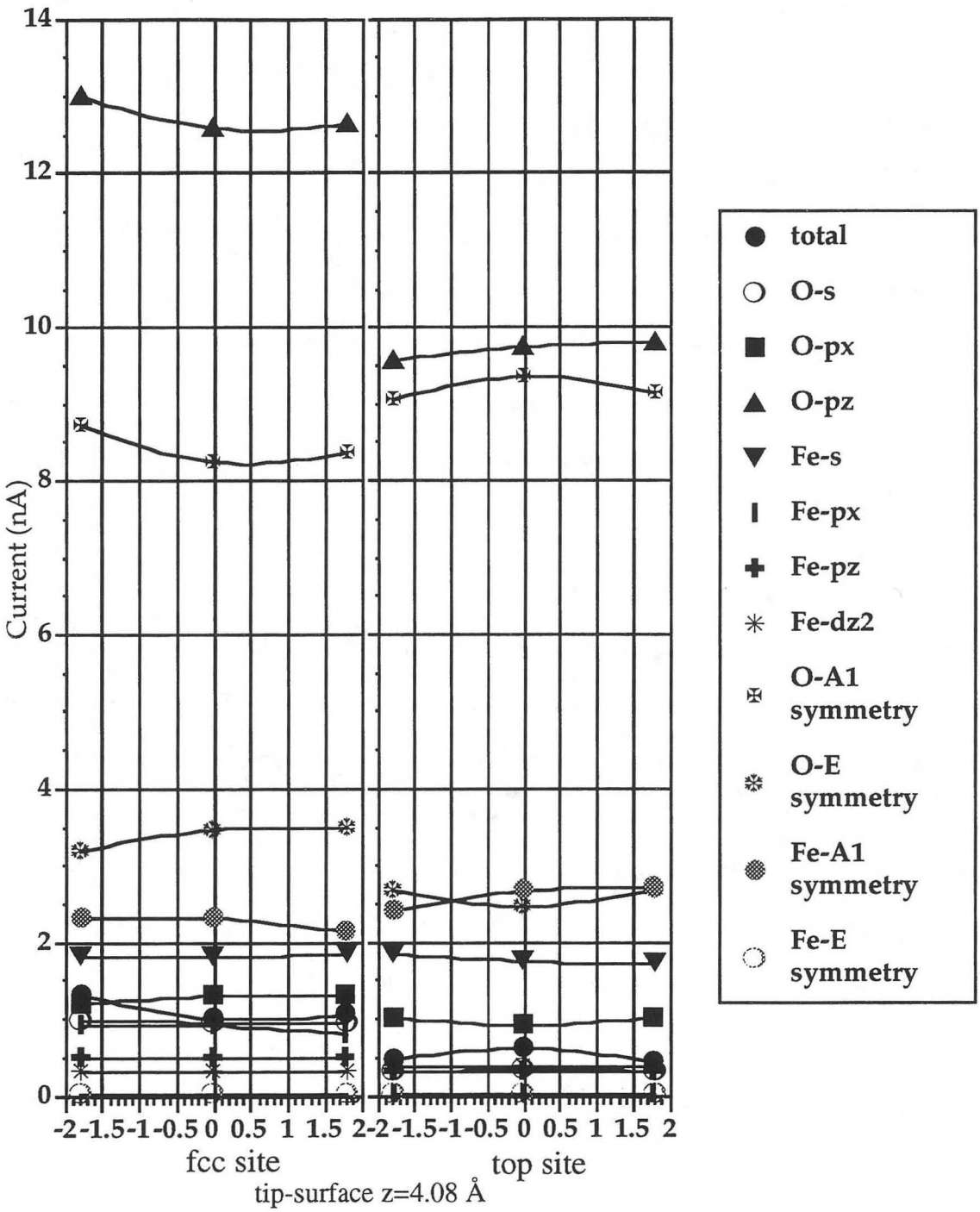

Figure 6.14 Orbital decomposition, fcc vs. top, Pt tip

The individual orbital contributions and symmetric groupings of the orbitals are shown for both the fcc and top configurations. All contributions are lower for the top except the Fe-A1 and O-A1. (Only one orbital is shown where two give very similar results, i.e. only p_x is shown and not p_y.)

Many features are the same for both configurations. For example, the O-s interferes destructively with the O-p_z reducing the current amplitude but not the corrugation as only the O-p_z is corrugated. The states of A1 symmetry contribute more strongly than those with E symmetry. (A1 symmetry is perpendicular to the surface, i.e. s, p_z, and d_{z^2} components, while E symmetry is parallel to the surface.) Only one Fe-d orbital is significant, d_{z^2}, but Fe-s and Fe-p orbitals are significant as are all the oxygen orbitals. The Fe-A1 and O-A1 components are enhanced for the top configuration. These are the combinations that occur along the Fe-Pt bond axis. However, the Fe p_x and p_y contributions are very small unlike the fcc configuration.

6.7 States decompositions

Another method of analysis to understand the origin of the current is to focus on the electronic states (calculated as eigenstates for a slab of the surface) that contribute the most to the tunneling current. These states are expressed as linear combinations of atomic orbitals and so for a Pt-Fe-O slab with 16 atoms in each layer there are 352 states. Some of the states are degenerate, i.e. correspond to the same energy, and will be grouped into blocks The selection is also restricted by considering only those states which are near the Fermi level as these states contribute most strongly to the tunneling current. For these calculations, we have checked from -10.5 eV to -7 eV, for a Fermi level of -9.9 eV. (Note: only relative energies are important.) In this energy range, four states were found to have a significant contribution and only one of them is the same order of magnitude as the total current. This corresponds to a state at an energy of -10.0 eV, or 0.1 eV below E_f as shown in Fig. 6.15. Two states that are even closer to the Fermi level only contribute weakly. Thus, calculating the states closest to the Fermi level alone would not be valid. The state at -10.0 eV also yields a corrugation similar to the total current value. The result is shown in Fig. 6.15 and the total current is plotted at the far right of the graph.

This state is 6-fold degenerate and consists basically of a linear combination of O-p_z and Fe-d_{z^2} orbitals and is pictured in Fig. 6.16. The O-p_z orbitals appear with the same phase in pairs of rows with the Fe atoms d_{z^2} having a small antibonding interaction in between these rows, as shown by the energy which is higher than both atomic orbital energies. The O p_z and the Fe d_{z^2} have an opposite sign with respect to the interaction with the tip apex atom. These pairs of rows are repeated with alternating phases. The symmetry appears lower than the surface but only because the state shown is one of a set of six degenerate states that combine to form a state with the symmetry of the surface. Identifying the state illustrates the orbital origin of the destructive interference between the Fe and O components since their orbitals combine with alternating signs. Even though the Fe is farther from the surface, the orbitals are more diffuse and extend further from the atom so the values of Fe and O contributions are similar enough that the interference is strong as explained previously. Also, the individual O orbital contributions interfere more destructively with each other than the individual Fe orbital contributions leading to O and Fe total contributions that are even closer in magnitude than is apparent from the orbital components.

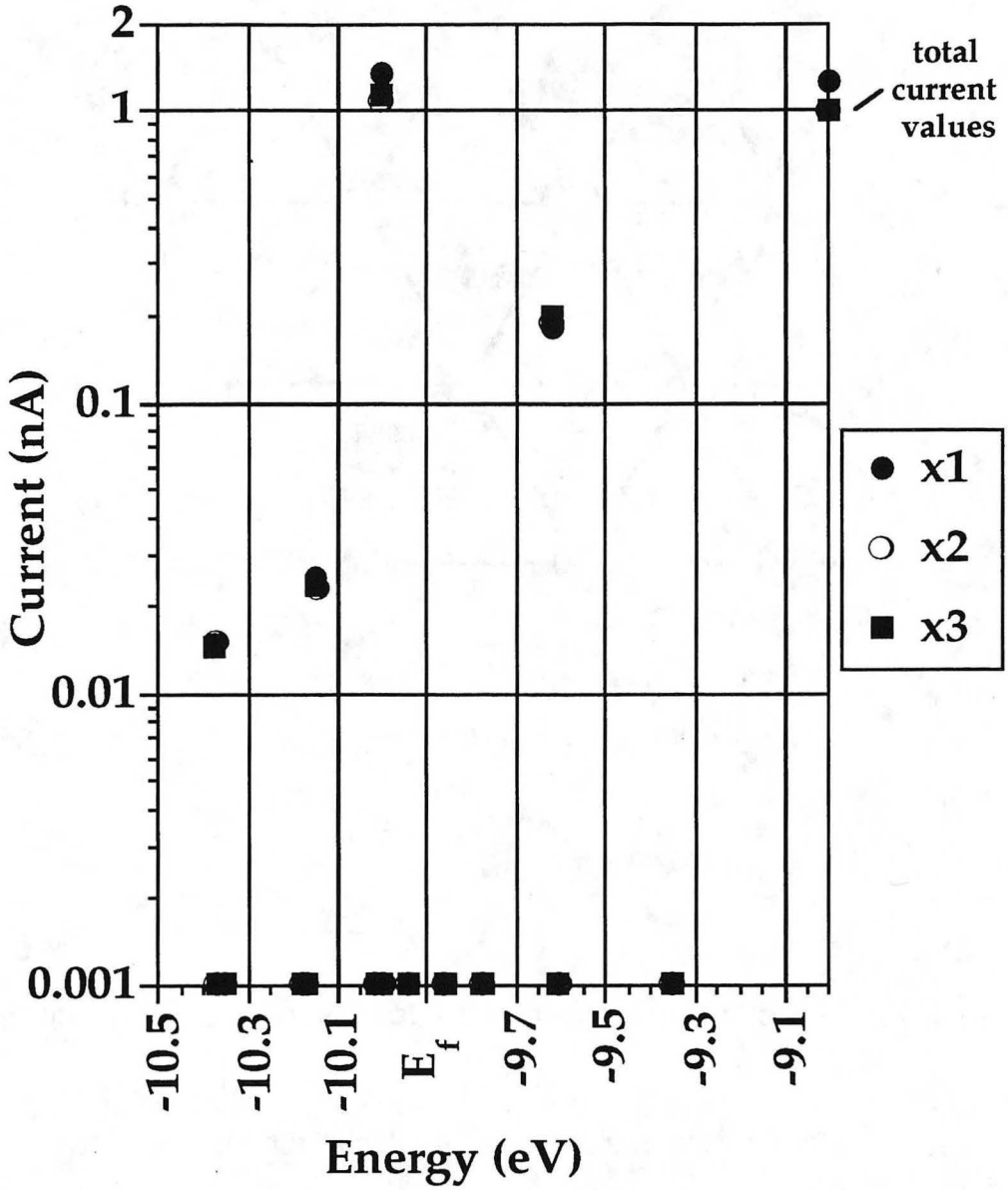

Figure 6.15 States decomposition, Fe-O bond = 1.90 Å

The amount of current contributed from several states near the Fermi level (-9.9 eV) is shown. The three points (x1, etc.) correspond to the tip position above the Fe, O and Pt atoms. The state with the highest contribution is at -10.0 eV and is not the closest state to the Fermi level. The total current is shown at the far right of the graph for comparison. The states that are shown at a value of .001 nA actually contribute even less to the tunneling current (~ 10^{-6} nA) but are shown at that value for convenience.

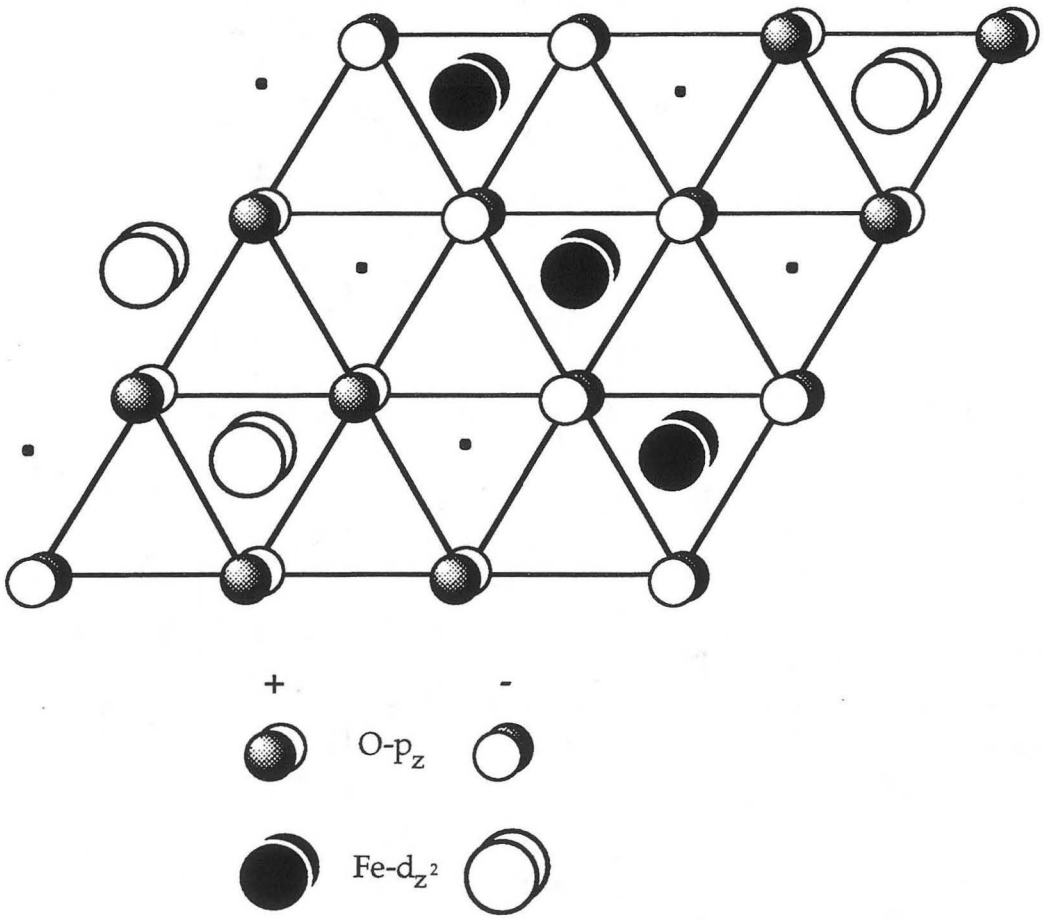

Figure 6.16 Model of important state for tunneling, Fe-O bond = 1.90 Å

The molecular state of the surface slab that contributes the most to the tunneling current is shown. The lattice is drawn on the oxygen atoms. The lower symmetry is because the state is actually only one of a set of six degenerate states that retains the surface symmetry.

Another look at the orbital decompositions for the top and fcc configurations (Fig. 6.14) reveals that the top configuration has an enhanced Fe-A1 current compared to the fcc (the Fe-d_{z^2} contribution is also slightly higher although not visible on the graph). Since the orbitals primarily responsible for the destructive interference include the Fe-

d_{z^2}, a stronger d_{z^2} contribution makes the interference more destructive for the top configuration. In addition, the O-s contribution is reduced compared to that of the O-p_z for the top configuration so they do not interfere as destructively further enhancing the destructive interference. Since the d_{z^2} are located along the Fe-Pt bond for the top configuration, it makes sense that the contribution would be enhanced for the top configuration as compared to the fcc.

The states calculation can also be repeated for an Fe-O spacing of 2.0 Å, where the atomic corrugation decreases dramatically. The general picture is shown in Fig. 6.17. The same tip surface separation is kept as the fcc configuration with a Pt tip so those values are used for the purpose of comparison. The oxygen contribution increases by a factor of 3 and the Fe contribution decreases. The increase in the oxygen contribution cannot simply be caused by a distance change as that is kept constant and equal to that used for the Fe-O bond of 1.90 Å. Also, the interference has changed from destructive to constructive suggesting that the state important for tunneling has changed also.

This is verified by calculating the new state decomposition at the longer Fe-O bond length. The results are shown in Fig. 6.18. Now the most important state has an energy of -9.83 eV or 0.07 eV above E_f and is not very corrugated. The total current is also much larger (10 nA as opposed to 1 nA) than for the Fe-O bond length of 1.9 Å even when the tip-sample spacing is kept constant. When performing the states calculation for a longer Fe-O bond, the energies of all states are shifted down. This is because as the Fe-O interaction is decreased, antibonding states become less antibonding and shift down in energy. The states in the region around the Fermi level are antibonding as compared to the energy values for Fe and O. Since the states are moving with respect to the Fermi level, the state that is most important for tunneling has changed from the situation where the Fe-O bond is 1.90 Å. The corrugation is decreased compared to the total current ($\Delta I/I$ is decreased by a factor of 2). The predicted experimental corrugation would be even smaller because the tip must move out more than an angstrom to keep the same current.

The effect is even more pronounced for the bulk Fe-O bond distance of 2.15 Å. Thus, the atomic corrugation is decreased for two related reasons. The state important for tunneling is less corrugated and yields more current so that the tip-surface distance is increased. Since the magnitude of the iron contribution is much smaller than that of the oxygen the two only interfere weakly. The interference is also weakly constructive removing the corrugation enhancement that occurred for the Fe-O bond of 1.90 Å.

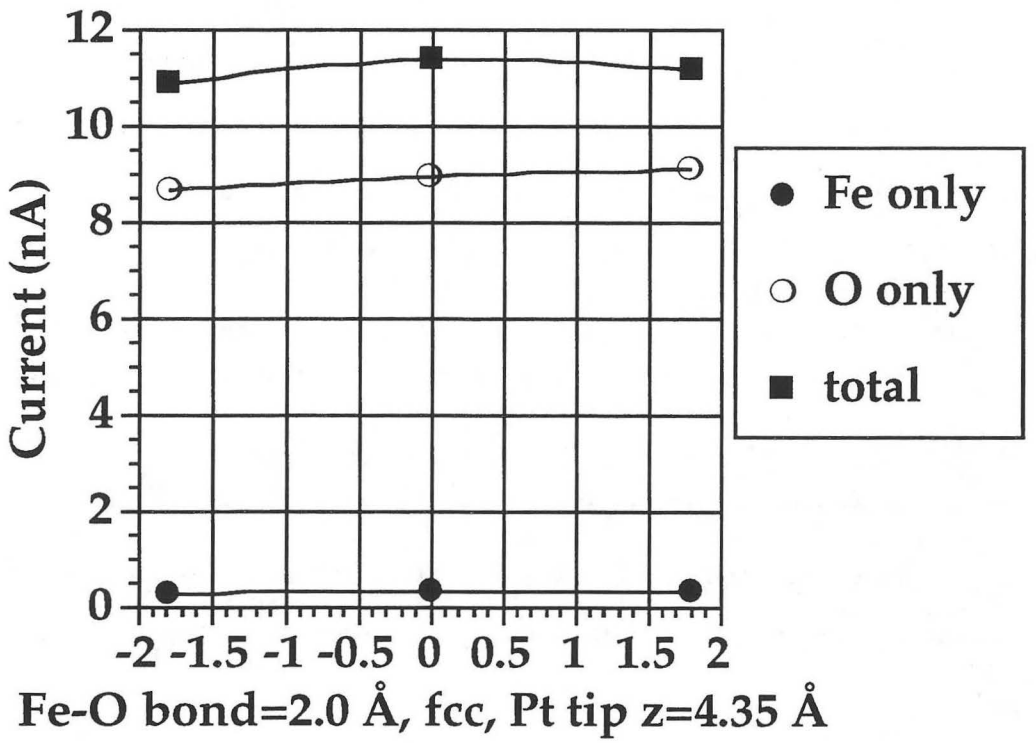

Figure 6.17 Current decomposition, fcc, Pt tip, Fe-O bond = 2.0 Å
The individual contributions to the tunneling current are shown for the same situation as in Fig. 6.9 except that the Fe-O bond is now 2.0 Å. The oxygen current corrugation is small and the interference between the iron and oxygen contributions has changed from destructive to constructive.

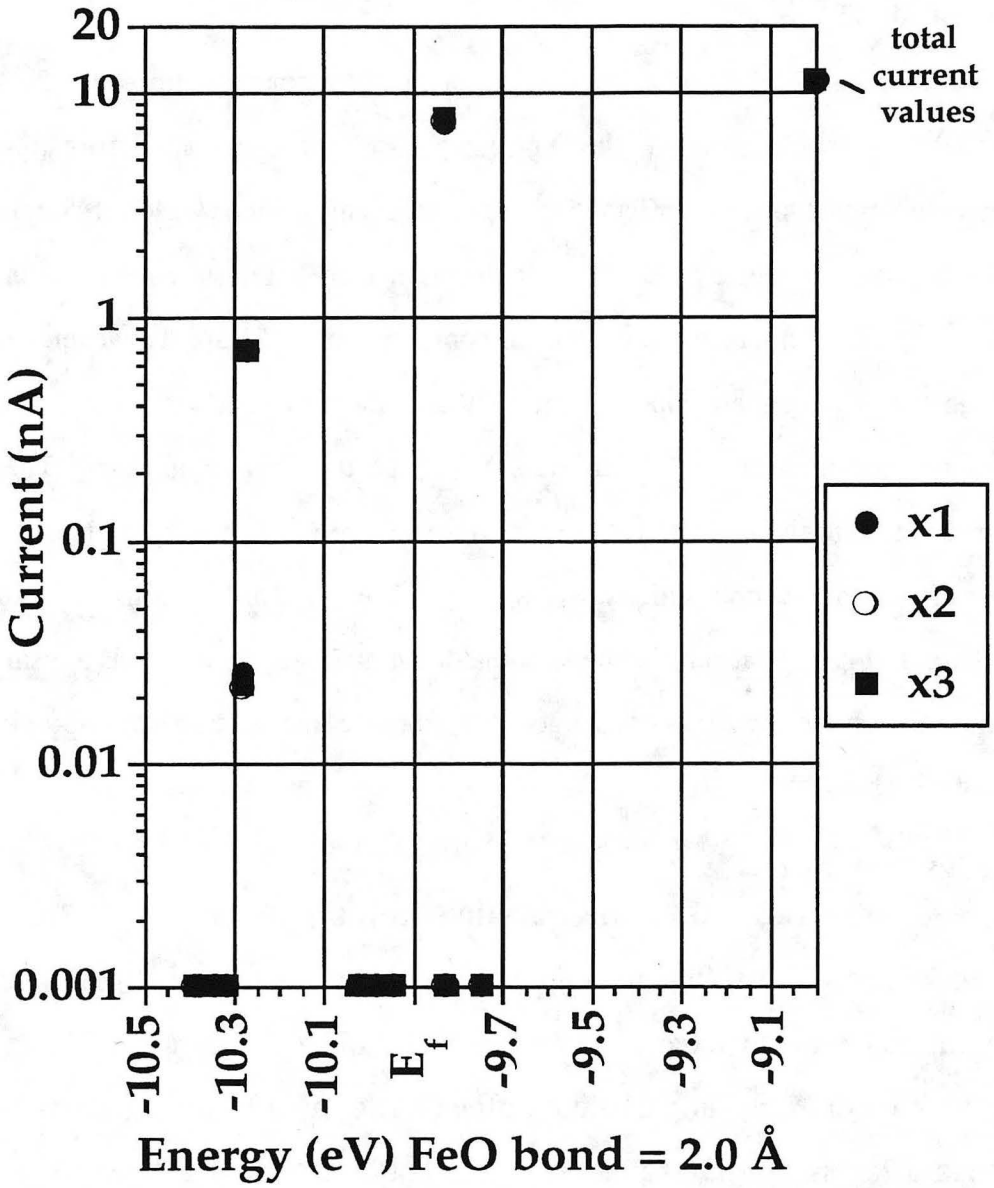

Figure 6.18 States decomposition, Fe-O bond = 2.00 Å

The amount of current contributed from several states near the Fermi level (-9.9 eV) is shown. The three points are the usual high symmetry points so that the corrugation of the current is also visible. The state with the highest contribution is now at -9.83 eV, slightly above the Fermi level. The total current is shown at the far right of the graph for comparison. The states that are shown at a value of .001 nA actually contribute even less to the tunneling current (~ 10^{-6} nA) but are shown at that value for convenience.

6.8 O and Pt3 tips

As has been shown for several cases, calculations for an O tip show the same trends as the Pt tip. For example, the O p_z current still dominates the corrugation and tunneling current and the top configuration has a higher corrugation and lower current due to a more destructive interference. A molecular states calculation shows that the surface state important for tunneling is not changed compared to the Pt tip. However, several results indicate that there are important differences in the O and Pt terminated tips due to strong perturbations of the tip electronic structure by the oxygen tip atom. The first indication is that in the hcp and fcc configurations there is a constructive interference between the Fe and O contributions as is shown in Table 6.2 although the top is again destructive. In Fig. 6.10 it can also be seen that the individual contributions are smaller. Since the state on the surface is unchanged it is probable that the tip state important for tunneling has changed.

Table 6.2 Interference ratios - O tip

The interference ratios for three tip positions are shown for three different configurations and an oxygen terminated tip. The three tip positions are above an oxygen, iron, and platinum atom. The layer of the Pt atom in the surface is given in parentheses for each configuration.

O tip	O	Fe	Pt
top configuration	0.535	0.865	0.838 (2)
fcc configuration	1.123	1.314	1.306 (1)
hcp configuration	1.166	1.339	1.331 (3)

This can also be seen in the comparison in Fig. 6.4 between the O and Pt3 tip. The majority of the current for the O is coming from the Pt3 base so these might be expected to be very similar. In fact, using the trimer of the tip as a reference point, the

bases of the tips are at very similar heights above the surface (0.1-0.2 Å higher for the O tip). Yet the Pt3 tip has significantly smaller atomic corrugations. Although the majority of the current may be coming from the Pt3 base, the O tip atom contribution is more corrugated. The case of the O tip tunneling into the oxide surface is different than that previously calculated by ESQC for metals where an O tip is significantly lower and the proximity to the surface leads to a strong enhancement of the corrugation. This does not seem to be the case here where the oxygen and platinum single atom tips have similar corrugations although probably by different mechanisms.

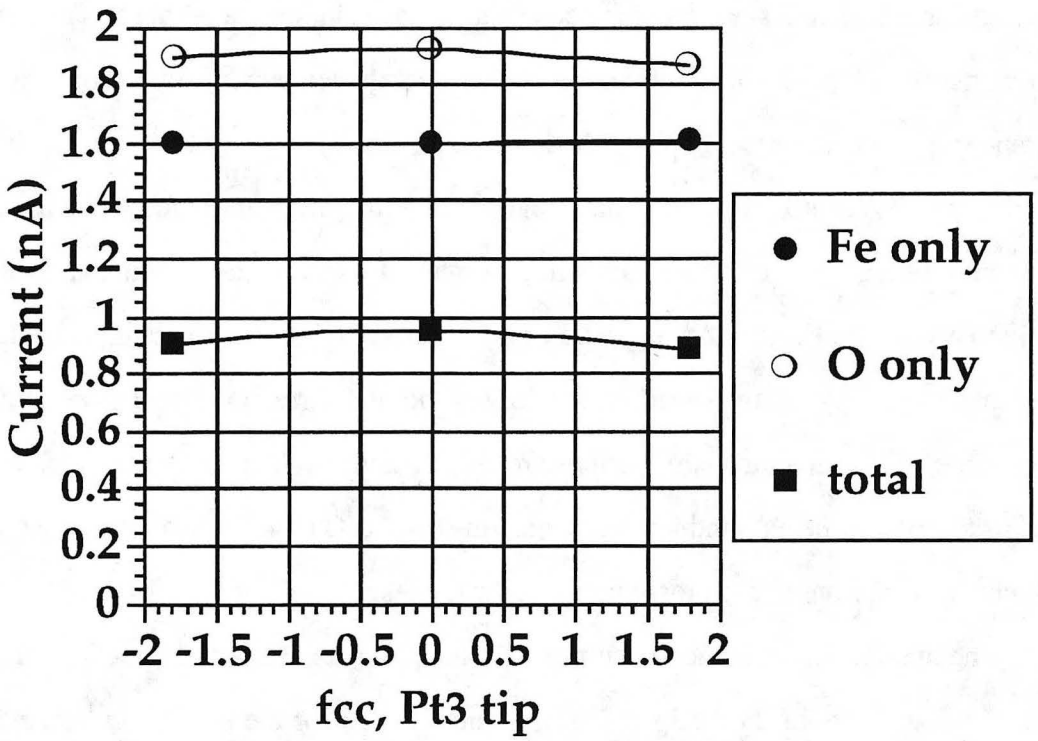

Figure 6.19 Current decomposition, fcc configuration, Pt3 tip

The oxygen current corrugation is small compared to the fcc corrugation and single Pt atom terminated tip (Fig. 6.9). The interference is also constructive, thus decreasing the corrugation further by leading to a larger tip-sample separation.

The Pt3 tip is actually more similar to the all Pt tip in terms of the current and interference trends, but when current decompositions are analyzed the individual contributions are not corrugated. Not even the O p_z has a very high corrugation. (Fig. 6.19) The interferences are also not tip position dependent. This can be understood as the larger tip 'averaging' out the corrugation by sampling more of the surface simultaneously.

6.9 Summary and conclusions

The small cell models that are used to perform ESQC calculations on the FeO/Pt(111) surface reproduce the significant features of the experimental images. The atomic corrugation and large periodicity corrugation have similar magnitudes as observed experimentally and the atomic corrugation varies across the large unit cell as shown by the differences in the small model cells. The long range periodicity is not in phase with the topography in any simple way. This is because there are electronic effects that are site dependent that change the average tunneling current. However, the atomic corrugation does increase as the tip surface separation is decreased giving rise to a simple relation with the topography of the surface that higher points correspond to larger atomic corrugations. The calculated corrugations are very sensitive to the Fe-O bond length but less sensitive to the Fe-Pt bond length. Changing the Fe-O bond length from 1.90 Å to 2.0 Å changes the state that is most important for tunneling.

The maxima in the tunneling current are always due to O atoms interacting with Pt atoms: the apex atom of the Pt tip and the platinum trimer for the Pt3 and O terminated tips. The hcp has a higher average current than the fcc configuration primarily due to a direct O-Pt interaction and the top configuration has a lower average current than the fcc configuration due to more destructive interferences. The destructive interference arises out of stronger Fe d_{z^2} and O p_z contributions and can be understood in terms of the state that is most important for tunneling.

The atomic corrugation is due to the O current corrugation, primarily from the O pz orbital and is enhanced by tip position dependent interferences. Especially for the Pt tip, destructive interferences are also important to keep the average current low so that the tip is closer to the surface and thus the atomic corrugation is higher. Constructive interferences between the iron and oxygen contributions would lead to overall higher tunneling currents, greater tip-surface distances and a reduced corrugation as is seen for the case of an Fe-O bond length of 2.0 Å.

Chapter 6 References

[1] L. Ruan, F. Besenbacher, I. Stensgaard and E. Lægsgaard, Phys. Rev. Lett. **70,** 26 (1993) 4079.

[2] F. Jensen, F. Besenbacher, E. Lægsgaard and I. Stensgaard, Surf. Sci. **259,** 3 (1991) L774.

[3] Y.J. Kim, C. Westphal, R.X. Ynzunza, H. Xiao, Z. Wang, H.C. Galloway, M. Salmeron, M.A.V. Hove and C.S. Fadley, in preparation (1995)

[4] H.C. Galloway, J.J. Benítez and M. Salmeron, Surf. Sci. **298,** 1 (1993) 127.

[5] N.D. Lang, Phys. Rev. Lett. **58,** (1987) 45.

[6] T.A. Land, T. Michely, R.J. Behm, J.C. Hemminger and G. Comsa, Surf. Sci. **264,** (1992) 261.

[7] W.E. McMahon, E.S. Hirschorn and T.-C. Chiang, Surf. Sci. **279,** 3 (1992) L231.

[8] P. Sautet and C. Joachim, Phys. Rev. B **38,** 17 (1988) 12238.

[9] E. Clementi and C. Roetti, At. Data Nucl. Data Tables **14,** (1974) 177.

[10] P. Sautet and M.-L. Bocquet, Surf. Sci. **304,** 3 (1994) L445.

[11] P. Sautet and C. Joachim, Chem. Phys. Lett. **185,** 1-2 (1991) 23.

[12] P. Sautet, J. Dunphy, D.F. Ogletree and M. Salmeron, Surf. Sci. **295,** (1993) 347.

[13] P. Sautet, J.C. Dunphy, D.F. Ogletree, C. Joachim and M. Salmeron, Surf. Sci. **315,** 1-2 (1994) 127.

[14] B.J. McIntyre, P. Sautet, J.C. Dunphy, M. Salmeron and G.A. Somorjai, J. Vac. Sci. Technol. B **12,** (1994) 1751.

[15] T. Schedel-Niedrig, W. Weiss and R. Schlögl, submitted to Physical Review B (1995)

Chapter 7 Oxygen and Sulfur on Ni(110)

7.1 Introduction

The Ni(110) surface has been the subject of numerous surface science studies aiming to elucidate the structure of the clean surface and various adsorbate induced reconstructions. This background of information has then in turn been used to understand coadsorption experiments on the surface. STM studies have been critical in understanding not only static properties but have also given insight into dynamics of processes on the surface both through dynamic measurements and through observations of islanding [1-3].

In this series of experiments, the coadsorption of oxygen and sulfur on the Ni(110) surface is studied. The two structures relevant to the work are the Ni(110)-p(2x1)O and the Ni(110)-c(2x2) S structures. Both form at room temperature and the basic structures are depicted in Fig. 7.1. The oxygen structure consists of O-Ni-O rows running perpendicular to the Ni close packed rows and has been shown to form by an added row mechanism involving mass transport of Ni. The sulfur structure forms an almost hexagonal array of sulfur atoms with only small relaxations in the Ni atoms and no actual rearrangement. While in most cases the STM does not provide atomic specificity the very different ordered structures formed by O and S on the surface makes it simple to distinguish where the two different species are located on the surface.

Ruan, et al [4] have also examined the reaction of H_2S with a precovered O surface observing that the reaction is homogenous and creates small (~30 Å) islands of remaining p(2x1)O and troughs of c(2x2)S. One eventual goal in studying this system was to provide data on oxygen imaging by STM so that calculations could be performed. While this work does not include STM calculations for these surfaces, mixtures of the c(2x2)S/p(2x1)O and p(2x1)O/p(3x1)O_f structures could provide important tests for STM calculations involving oxygen-metal systems.

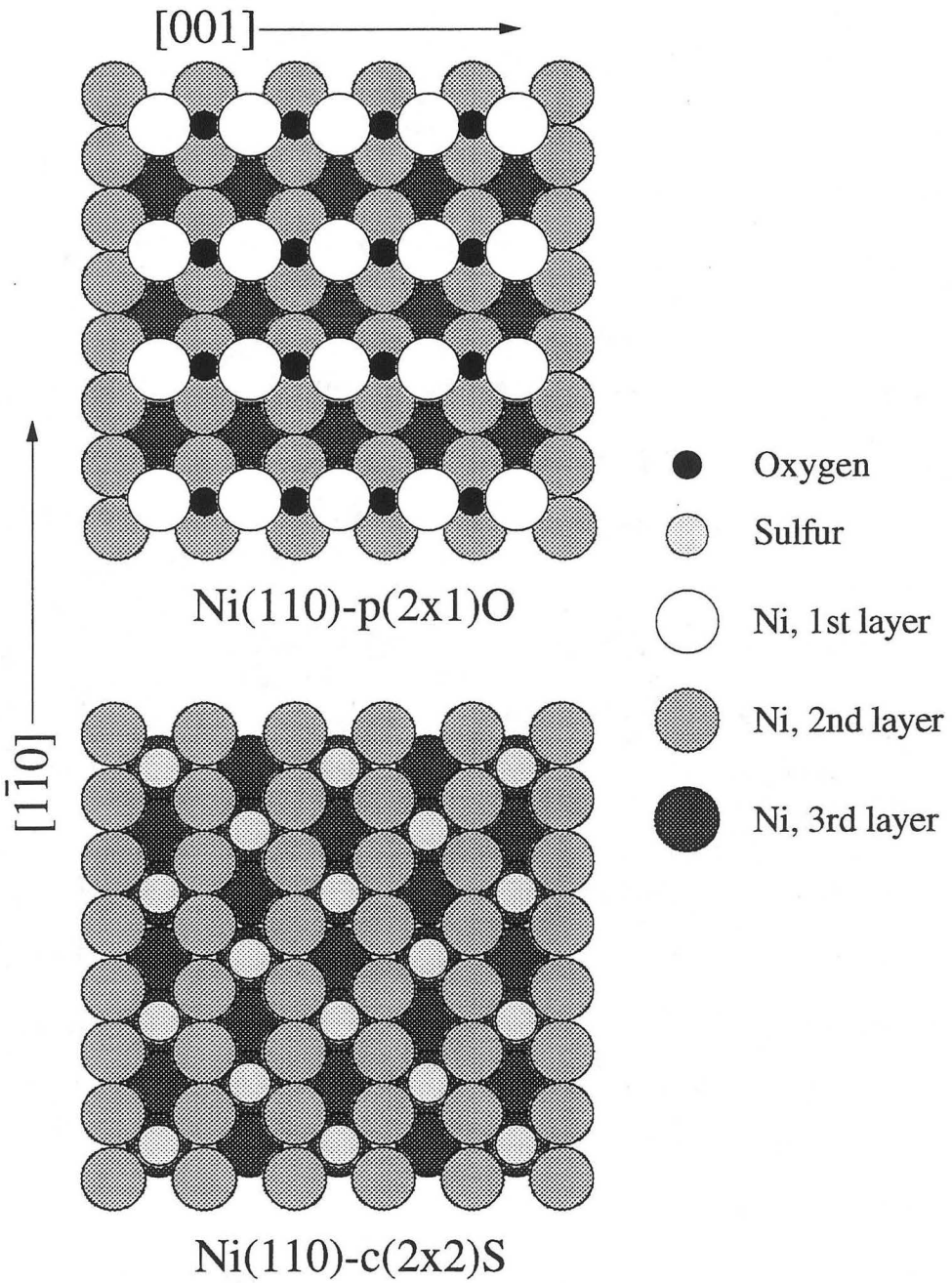

Figure 7.1 Ni(110)-p(2x1)O and Ni(110)-c(2x2)S

The oxygen structure consists of added O-Ni-O rows that form by mass transport and involves a major reconstruction of the surface. The sulfur structure has sulfur adsorbed in four fold hollow sites and does not involve a major restructuring of the surface, but only causes small relaxations.

In particular, an atomic contrast reversal has been seen in the Ni(110)-p(2x1)O system where the oxygen atoms are thought to change from imaging as maxima to minima [5] due to a change in tip termination. When two structures are imaged simultaneously, the theory must predict both of them using the same tip structure and termination. However, the focus of this chapter will be on the results of the coadsorption experiments and the surface structures that are formed when both O and S are present on the surface. In addition, the effect of sulfur on steps and a brief comment on the structures formed by only oxygen will also be included.

7.2 Oxygen and sulfur coadsorption

7.2.1 Low temperature preparation

The sample preparation consists of cleaning the Ni(110) crystal by repeated cycles of sputtering and annealing to 750 C, but for several experiments it was not possible to remove the residual S contamination and a significant amount of sulfur would segregate to the surface when the crystal was cooled. In addition, the crystal was also allowed to cool in a small pressure of oxygen ($<1x10^{-9}$ torr) producing a surface that is entirely covered with either oxygen or sulfur. A large scale image of the resulting surface is shown in Fig. 7.2.

The surface shows highly anisotropic islands (labeled A) that have a regular spacing of 150-200 Å in the [001] direction and are almost continuous in the $[1\bar{1}0]$ direction. The width of the troughs (labeled B) between the islands is also consistent but slightly decreased (~50-100 Å) from the width of the islands (100-150 Å). A few deeper pits (labeled C) are also visible. Although AES spectra identify O and S on the surface it is not clear from this type of image where they are located. However, in Fig. 7.3, an atomically resolved image at the boundary between an island and trough is shown. On the left side, the island shows the characteristic rows of the p(2x1)O surface while on the

right the almost hexagonal array of maxima obtained for the c(2x2)S structure are observed.

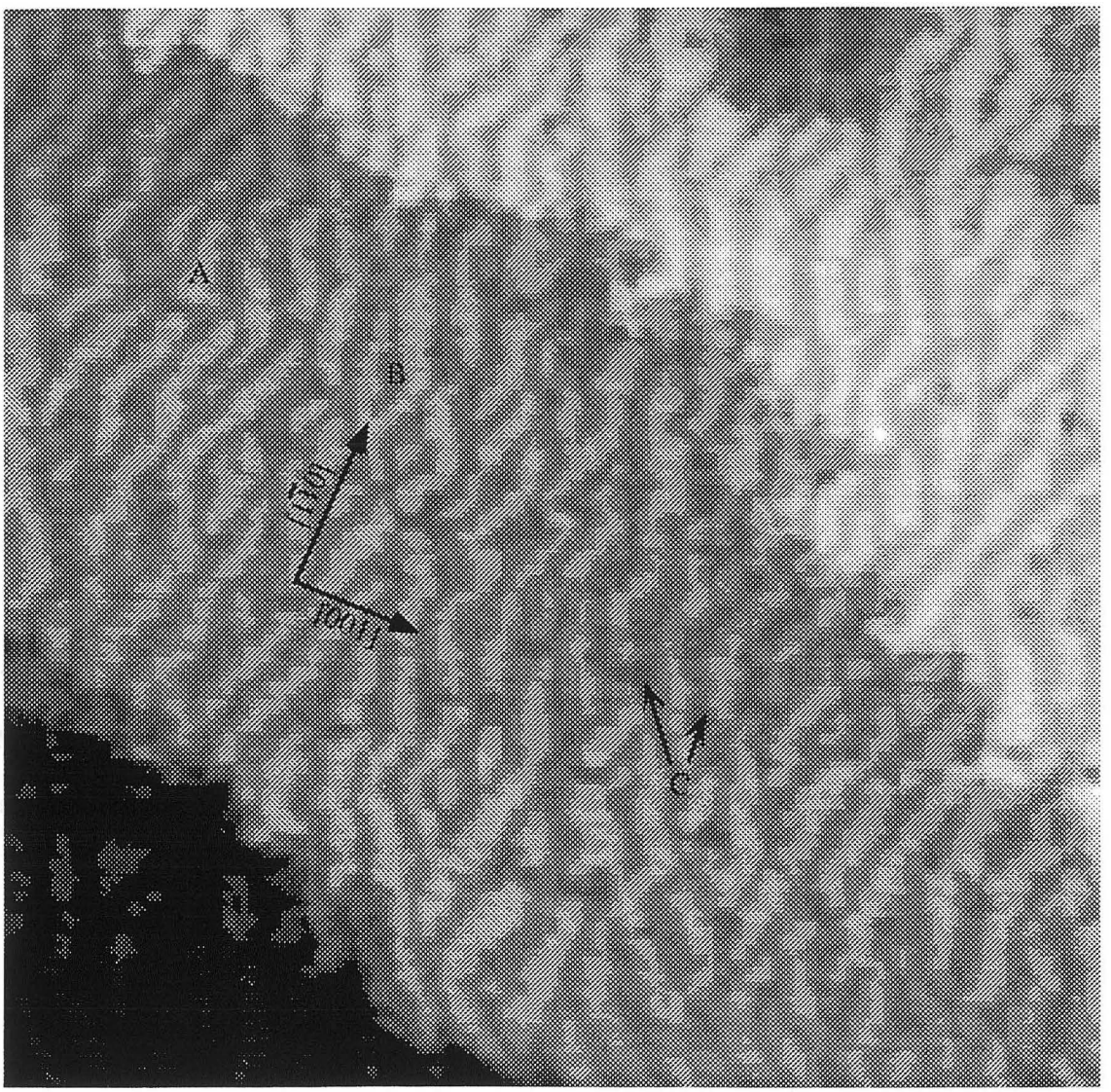

Figure 7.2 Islands - low temperature preparation

The islands predominantly run in the $[1\bar{1}0]$ direction and have a spacing of ~200 Å in the [001] direction. The island width is 100-150 Å and the trough width is 50-100 Å. (3050 Å x 3060 Å, I = 0.96 nA, Bias = -0.54 V)

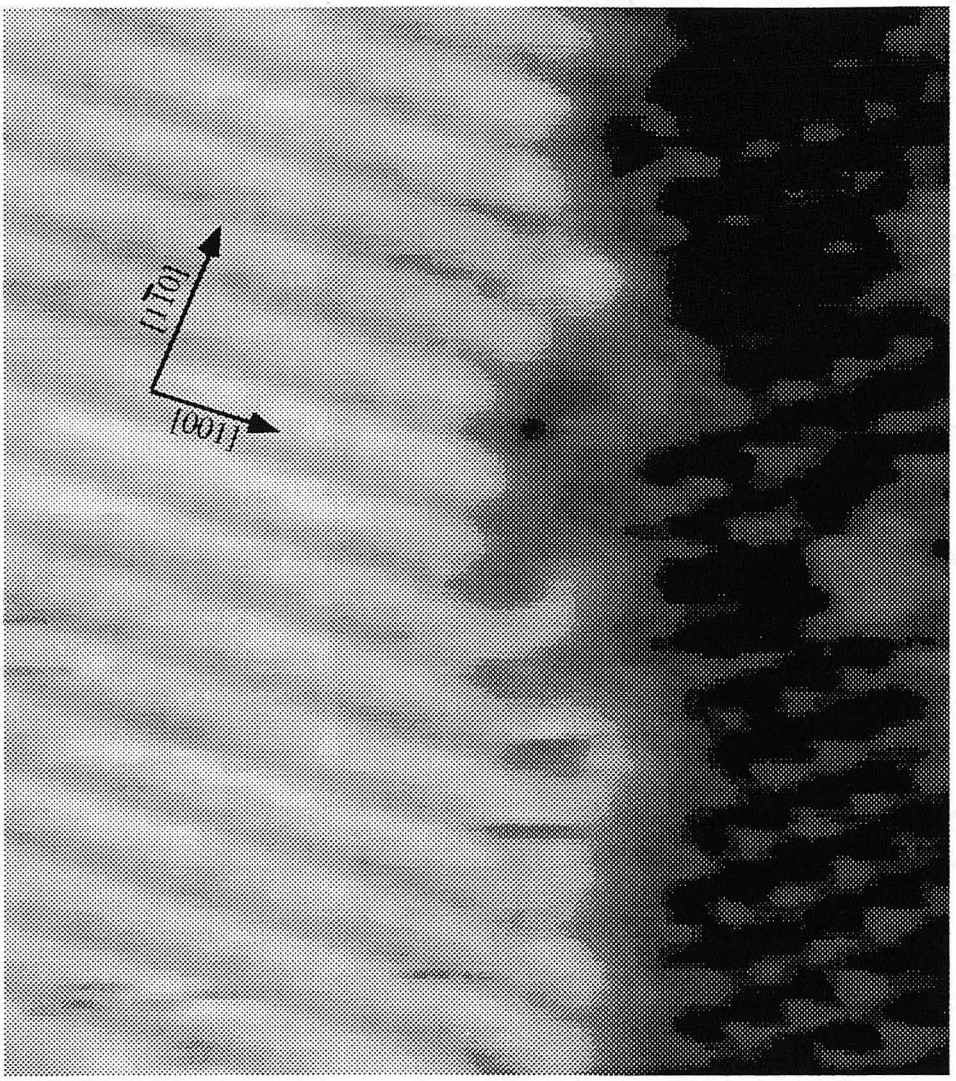

Figure 7.3 Atomic resolution - island/trough structure

On the left side island the rows of the Ni(110)-p(2x1)O structure are seen and on the right side (trough) the almost hexagonal array of maxima typically observed for the Ni(110)-c(2x2)S. (67 Å x 72 Å, I = 0.96 nA, Bias = -0.54 V)

The difference in the average height of the islands and troughs as measured by the STM is 0.6-0.8 Å. The maxima in the c(2x2)S structure and the rows of maxima in the p(2x1)O structure are aligned leading to a model of the surface such as that given in Fig. 7.4. If each structure was on different Ni terraces, the structures would shift by one half

a lattice constant in the $[1\bar{1}0]$ direction and the symmetry would be inconsistent with that observed by STM. A shift by two layers would still be consistent as would a shift by any other even number of layers. However, two layers of Ni is a change of 2.5 Å which seems inconsistent with the observed height of 0.6-0.8 Å. This conclusion is only based on assuming that points of high symmetry on the images correspond to symmetric locations of the atoms, but it is not necessary to assume that the S or O-Ni-O rows are imaged as maxima or minima. Images like this one confirm that the elongated islands consist of the p(2x1)O structure while the troughs are covered by the c(2x2)S structure. The deeper pits are one monatomic step below the islands and are also oxygen covered.

Furthermore, the short dimension of the islands is definitely along the [001] direction (the direction of the O-Ni-O rows), and the long direction of the islands is surprisingly along the $[1\bar{1}0]$ direction (perpendicular to the added rows). Although the primary direction of the islands is along $[1\bar{1}0]$, the edges of the islands are at an angle from this direction but are somewhat rough making a precise definition of the edge angle impossible from this data. The atomic directions are labeled in Fig. 7.2 and 7.3 for reference.

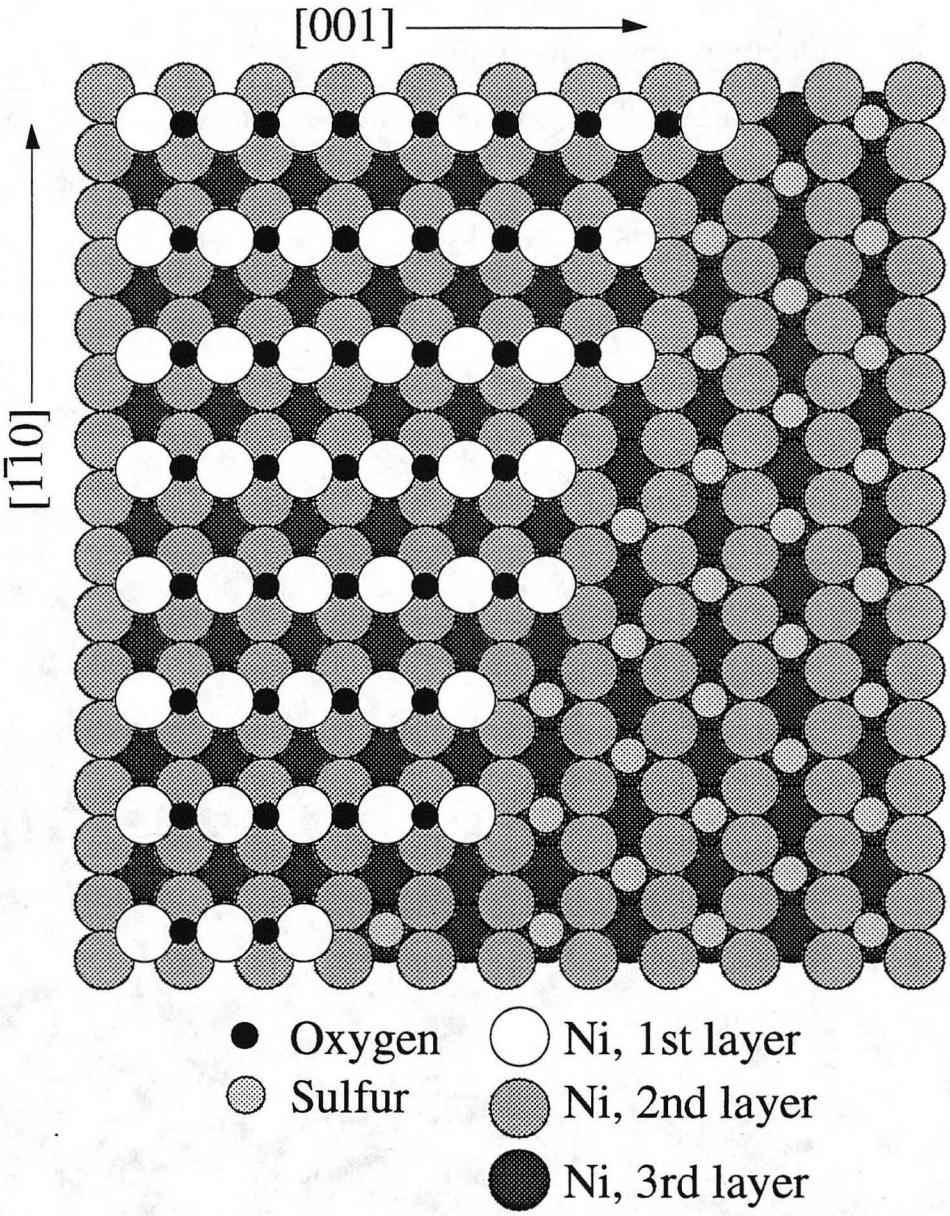

Figure 7.4 Island/trough model

Model of the boundary between an island and a trough based on the registry of the two structures and the angle of the island edges with respect to the step edges.

7.2.2 High temperature preparation

For some experiments, the residual sulfur contamination was reduced below the level detectable by AES. Thus, a different preparation method was used which consisted of dosing the sample with 0.1 L H_2S and heating to 200 C to remove the hydrogen. Then the sample was dosed with 1.5 L O_2 and heated to 500 C. The resulting surface is shown in Fig. 7.5.

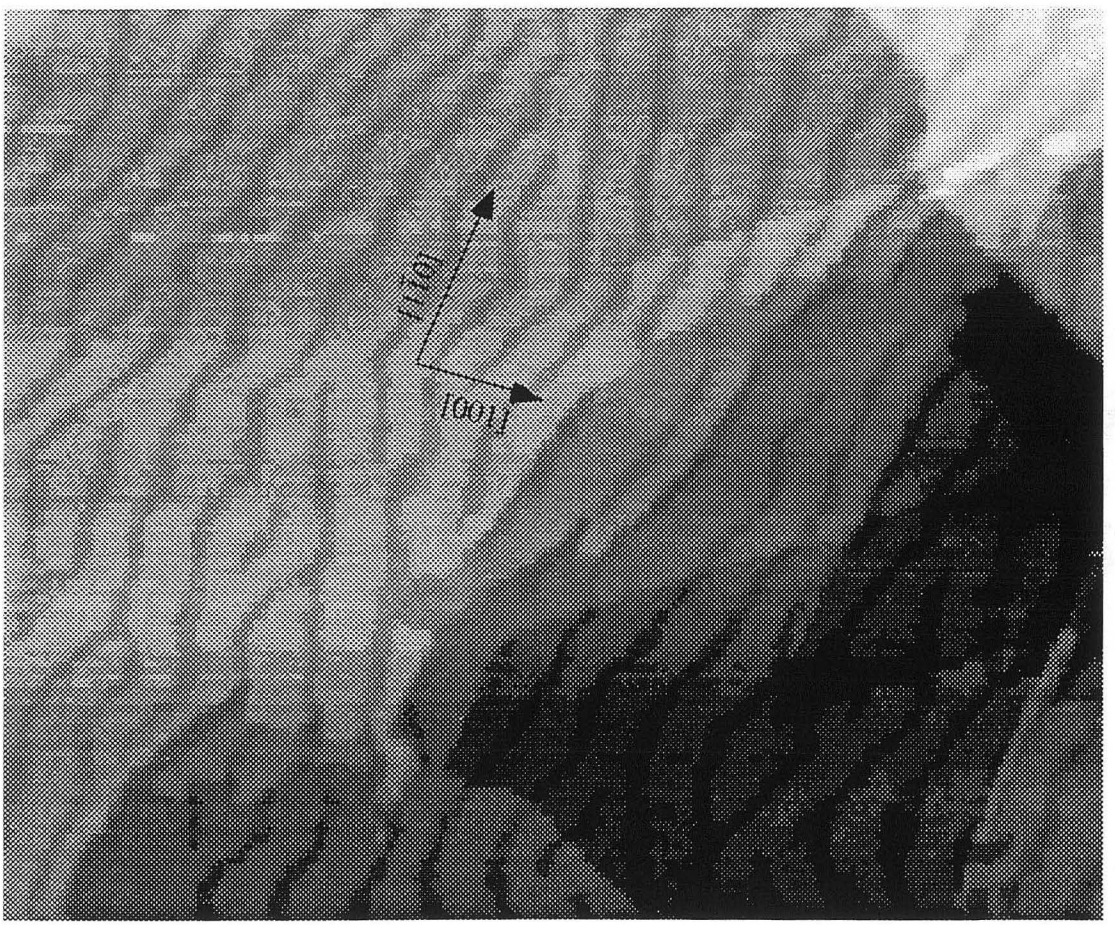

Figure 7.5 Islands - high temperature preparation

Similar to Fig. 7.2, islands running in the $[1\bar{1}0]$ direction with a ~250 Å spacing are seen. The island widths are ~200 Å and the trough widths are ~50 Å. The edges of the islands are straighter and no third level is seen. (2700 Å x 2250 Å, I = 1.25 nA, Bias = -0.59 V)

In this case, very similar structures are observed but the edges of the islands are much straighter showing that the higher temperature of formation has produced a more ordered surface.

Histograms of the pixel heights of images of the two structures created by the low and high temperature preparations (Fig. 7.2 and 7.5) are shown in Fig. 7.6. They indicate that the second preparation has more oxygen islands than sulfur troughs while the first method has about the same amount of surface covered by each structure. The change in the relative amounts of sulfur and oxygen is also seen in AES measurements. These changes in composition from the first to second preparation mostly result in the average O island width increasing from ~100 Å to ~200 Å, while the S troughs retain approximately the same width for both sets of data with a slight decrease for the second method. (Accurate measurements of trough size are limited by the influence of the tip radius as well as the considerable roughness in Fig. 7.2.)

A number of steps are observed in the images that have angles between them consistent with the [001], $[1\bar{1}0]$, $[1\,\bar{1}\,1]$, and $[\bar{1}11]$ directions. These can be used to define the angle that forms the edges of the islands. The edges form an angle of 140° between them and are at ± 20° from the $[1\bar{1}0]$ direction. This is consistent with the $[2\bar{2}1]$ and $[2\bar{2}\,\bar{1}]$ directions where the island adds/removes one Ni-O unit in the [001] direction for every four lattice spacings in the $[1\bar{1}0]$ direction as is depicted in the model in Fig. 6.4. The existence of a well defined angle is probably due to the precise configuration of S and O at the edge of the island/trough structures but the images are not clear enough at the boundary to determine the structure accurately.

In Fig. 7.5, it is also noted that the island/trough structures continue across step edges. This also occurs in Fig. 7.2 but not quite as consistently. While some of the steps might have formed by annealing out screw dislocations and thus formed after the island/trough structure, this is observed for all the steps in Fig. 7.5 and indicates an interaction that continues across the step edge.

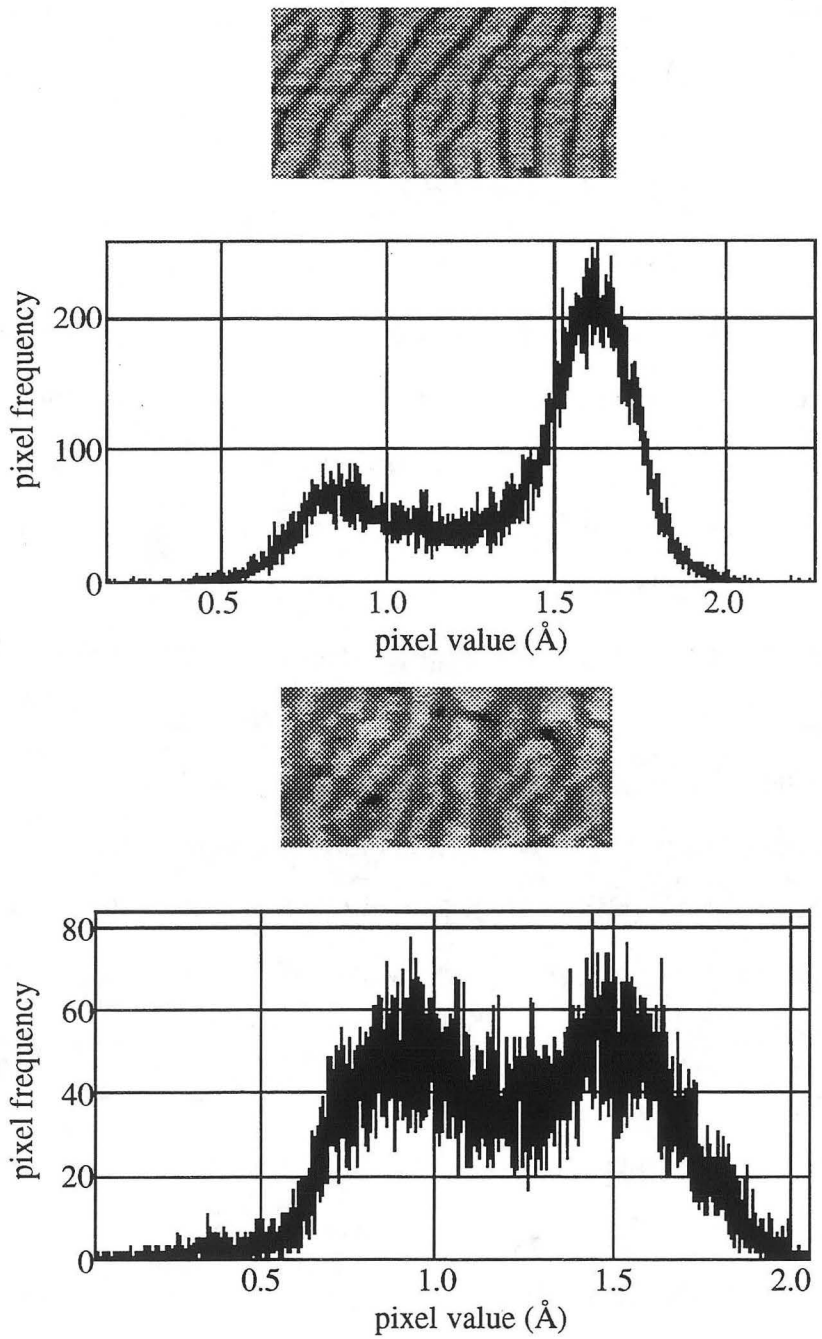

Figure 7.6 Histograms - low and high temperature preparations

Histograms of both the low (bottom) and high temperature (top) preparations show that the relative concentrations of islands and troughs are changing due to changing concentrations of oxygen and sulfur as observed by AES.

Another difference between the two sets of data is that in the low temperature preparation shown in Fig. 7.2 there are actually some deeper pits (labeled C) creating a third layer in the surface. These are one Ni step height below the oxygen structure and are also oxygen covered. These third layer holes are not observed in the high temperature preparation in Fig. 7.5 . This result is consistent with the behavior of the p(2x1)O structure without the presence of S as this structure forms by mass transport of Ni both from the step edges and by Ni atoms that are removed from the terrace leaving behind holes. Annealing causes the surface to become smooth again by increasing the mobility so the holes are filled in.

7.2.3 Removal of islands

As the oxygen exposure is increased pits form in the surface to provide the Ni atoms to form more O-Ni-O rows and the surface begins to convert to the Ni(110)-$p(3x1)_fO$ structure similar to the non-sulfur contaminated surface [6]. This structure consists of pairs of adjacent O-Ni-O rows separated by a missing row and is depicted in Fig. 7.7.

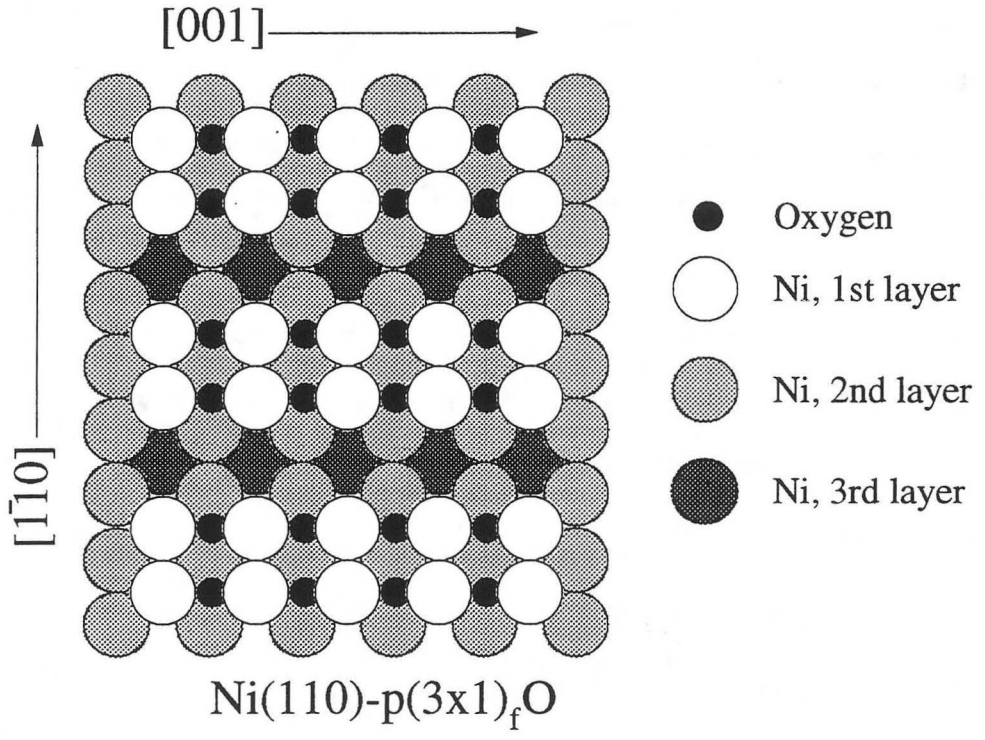

Figure 7.7 Ni(110)-p(3x1)$_f$O

Ball model of the Ni(110)-p(3x1)$_f$O consisting of two adjacent O-Ni-O rows and then a missing row.

The transformation is depicted in Fig. 7.8 where the upper image shows the pits forming in the terrace while the island/trough structure is still visible and then in the lower image the p(3x1)O_f/p(2x1)O structures have formed continuous bands in the [001] direction removing the island/trough structure. These structures are seen as alternating wide and narrow rows composed of single or double added O-Ni-O rows.

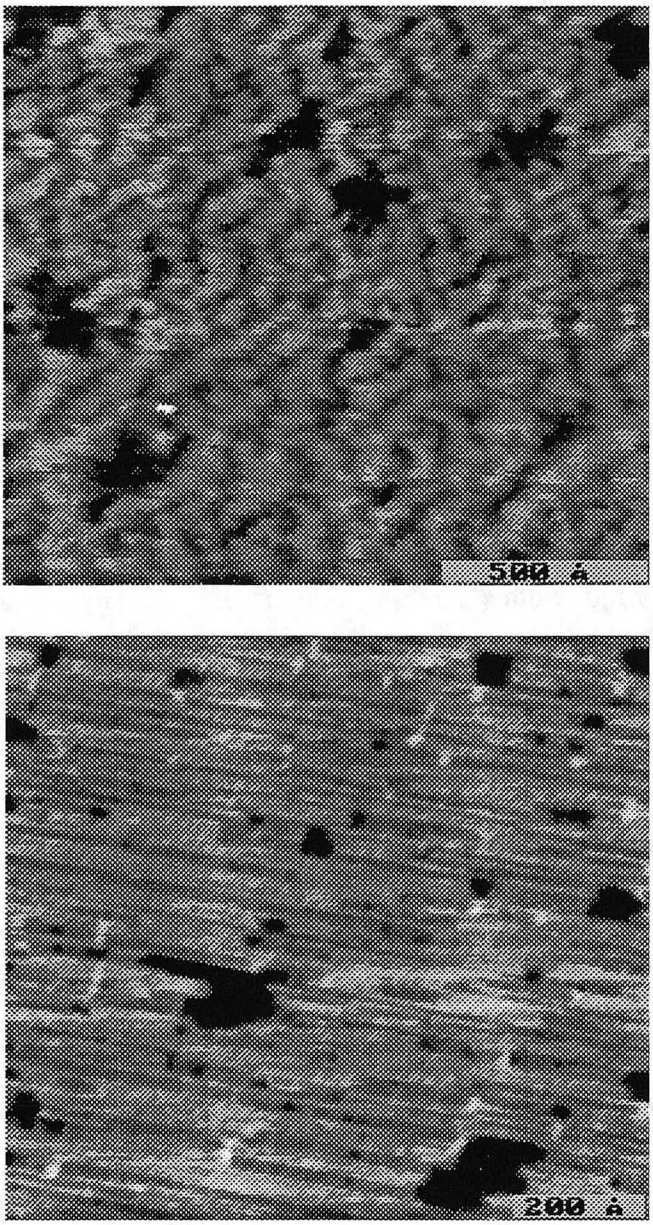

Figure 7.8 Removal of islands

In the upper image the deeper layer pits are beginning to grow and the island structure is more disordered. (1600 Å x 1600 Å, I = 0.90 nA, Bias = -369 mV) After more oxygen exposure, the surface appears as in the lower image where alternating narrow and wide bands of the p(2x1)O and p(3x1)O structures are formed and some smaller pits also begin to appear. (1000 Å x 1000 Å, I = 1.0 nA, Bias = -98 mV)

7.2.4 Discussion of island/trough structure

One possible explanation of the island structure is that the presence of the adsorbate causes a strain in the surface as is schematically depicted in Fig. 7.9. If the O-Ni or S-Ni structure causes changes in bond lengths compared to the bulk O-Ni or bulk S-Ni structures or if there are changes in the surface Ni reconstruction, a surface strain could be introduced. Either a tensile or compressive strain could be responsible for the islands and the strain could be greatest in either the sulfur or oxygen structure. It is likely that the S-Ni interaction is dominant over the O-Ni interaction, as the width of the S troughs appears approximately constant or even decreases when the surface is annealed, while the oxygen island width changes by a factor of two. Another possible cause of the elongated islands is that the S inhibits the mobility of Ni atoms anisotropically preventing the formation of the O-Ni-O rows continuously in the [001] direction. The anisotropic surface could also lead to an anisotropic S-S interaction that favors elongated islands although this has not been observed for less than saturation coverages of sulfur in the absence of oxygen.

A study by Roux, et al [7] has examined the same Ni(110)-p(2x1) O with a sulfur contamination of 1-3 atomic % in the surface region. Although the amount of sulfur is probably somewhat lower than in our results, the preparation methods are very similar to the first preparation method. Using TOF-SARS (time of flight-scattering and recoil spectrometry) which is similar to ion scattering experiments where blocking dips corresponding to the atomic directions are observed, they have measured the structure of the Ni(110)-p(2x1)O surface with and without sulfur contamination. Their results show a loss of order in the $[1\bar{1}0]$ direction with significant blocking dips corresponding to distances of d and 3d in the $[1\bar{1}0]$ direction where the expected peak would be at 2d for the p(2x1)O structure. The observed islands would explain these results as the islands can be out of phase across the sulfur troughs leading to mixtures of interatomic spacings such as d and 3d rather than solely the 2d spacing expected from continuous Ni(110)-

p(2x1)O structures. From the LEED pattern, they assessed that the domain size in the [001] direction was at least 100-200 Å in agreement with the width of the islands in the [001] direction as observed by STM. They also postulated that the sulfur inhibits diffusion reducing the ordering of the oxygen structures, but could provide no direct evidence of this possibility.

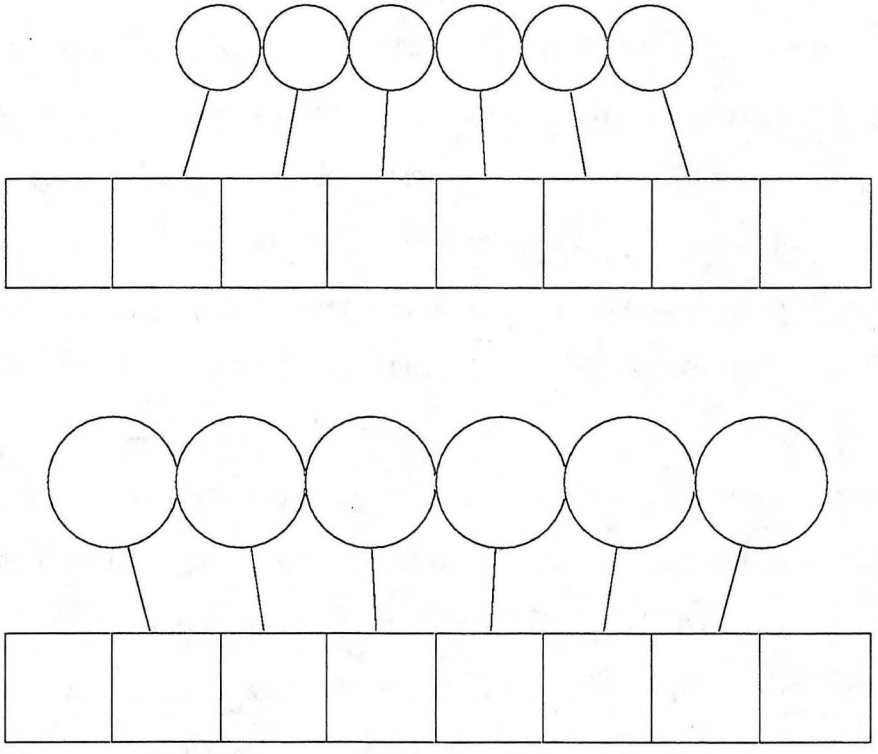

Figure 7.9 Strain model

Schematic of how the adsorption of a species can lead to a stress in the substrate.

Another result by Kern, et al [8] on the Cu(110)-(2x1)O surface is similar to this work in that an ordered array of elongated islands is observed. However, the islands form in the opposite direction and are elongated in the [001] direction and consist of eight to fourteen O-Cu-O rows. They point out that the regular spacing of the stripes suggests

a long range repulsive force and also suggest the possibility of substrate-mediated elasticity being responsible for the effect. This work points to the possibility of a strain induced effect due to the adsorbates but also adds weight to the idea that the sulfur is the major driving force as oxygen alone on the surface might be expected to show islands running in the other direction in analogy with the Cu(110) surface.

Although this surface was chosen because the surface structures were identified by the large number of studies already conducted, these STM experiments have found a previously unreported structure. For the higher oxygen exposures where the island/trough structure has been removed, most areas of the crystal surface are covered with a mixture of the single and double O-Ni-O rows that comprise the p(2x1)O and p(3x1)O_f structures. However, in some areas a new structure consisting of areas of c(2x2)S separated by rows of bright maxima in the $[1\bar{1}0]$ direction is found as shown in Fig. 7.10. The spacing of the maxima is two lattice constants in the $[1\bar{1}0]$ direction and when there is a shift in the row it is by one spacing in the [001] direction. If the maxima in the c(2x2)S structure are assumed to correspond to the sulfur atom positions then the extra maxima are located in two fold hollow sites as is depicted in Fig. 7.11. A similar structure was observed by Sprunger, et al [9] for CO and S coadsorption. It is not clear whether the extra bright maxima consist of O or S atoms or even of Ni atoms that have been ejected from the surface.

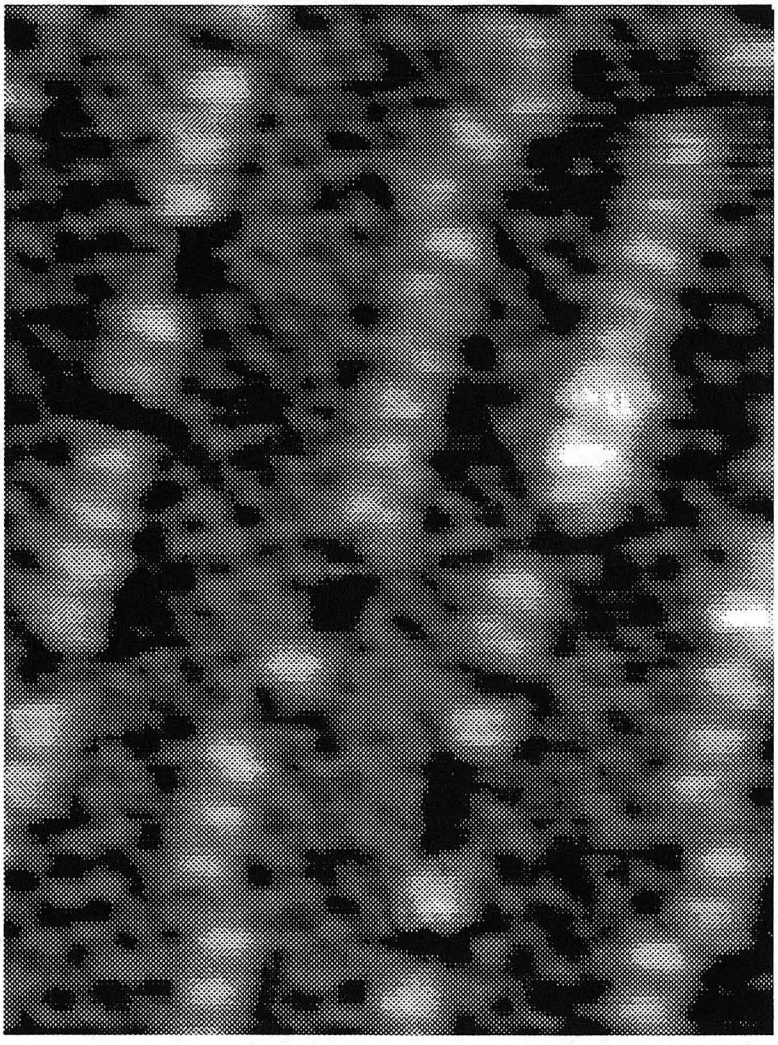

Figure 7.10 Mixed sulfur and oxygen structure

Regions of c(2x2)S are separated by partially ordered bright maxima. The spacing between maxima is two lattice constants along the $[1\bar{1}0]$ direction and the position is consistent with a two fold hollow site. (67 Å x 90 Å, I = 1.0 nA, Bias = -0.72 V)

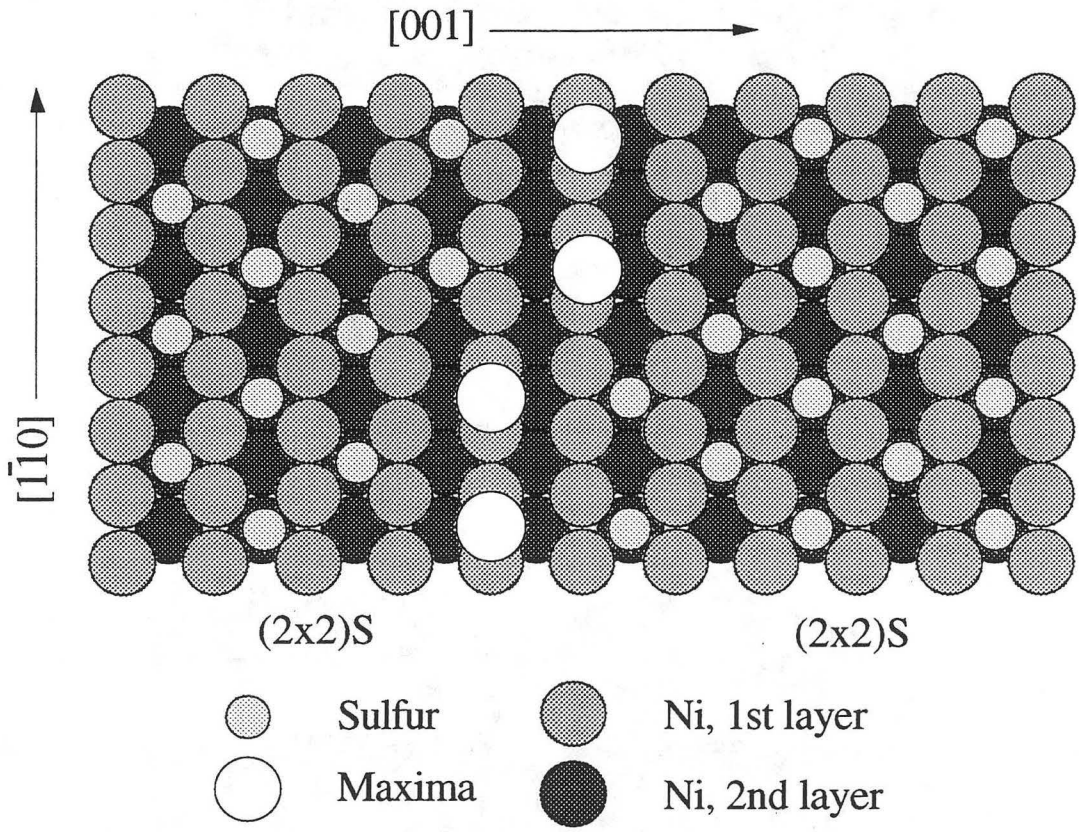

Figure 7.11 Mixed sulfur and oxygen structure - model

The Ni(110)-c(2x2)S structure is shown along with the position of the bright maxima observed in the image assuming that the maxima in the c(2x2)S structure correspond to the sulfur atoms. The maxima occur at the two fold hollow positions spaced by two lattice constants in the $[1\bar{1}0]$ direction and running in rows primarily along the $[1\bar{1}0]$ direction.

To summarize, several processes could contribute to the formation of the island/trough structure of p(2x1)O/c(2x2)S that is observed by STM. One is strain induced in the substrate by the chemisorption of one of the adsorbates creating a long range repulsion between the islands. The possibilities of S inhibited diffusion or anisotropic S-S interactions could also contribute to the formation of the islands. LEED studies on the Ni(110)-c(2x2)S structure have shown that S induces an expansion of the

first to second layer Ni spacing by 6-10% providing a mechanism for the sulfur inhibiting diffusion as well as suggesting that there is strain induced in the substrate by this expansion. At the present time, the data does not allow a distinction between the different processes.

7.3 Sulfur on Ni(110) - influence on step structures

As has been discussed in Ch. 7.2 and postulated in other studies small amounts of impurities such as sulfur can have strong effects on diffusion processes [10-12]. One possibility for the large effects of S inhibited diffusion observed even for extremely small amounts of S (0.02-0.05 ML) is that sulfur might trigger changes in the step structure [13]. By changing the density or preferred direction of the steps or by changing the barrier to diffusion at a step edge, small amounts of sulfur could have a strong effect on the diffusion.

In the hope of quantifying these effects, a comparison of step statistics for the clean, sulfur contaminated, and sulfur saturated surfaces has been made. The sulfur contaminated surfaces were prepared by annealing with S on the surface. For this study large scale images (4000 x 4000 Å) such as in Fig. 7.12 were methodically acquired over a few μm^2 of the sample before moving to another region and repeating the process. As is seen in the figure, steps along several directions are observed. Using atomically resolved images, particularly of the Ni(110)-p(2x1)O structure these directions are identified. In Fig. 7.12 steps are observed along the $[1\bar{1}0]$ and [001] directions as well as along the diagonals, the $[1\,\bar{1}\,1]$ and $[\bar{1}\,11]$ directions. In addition, steps at ~25-30° from $[1\bar{1}0]$ towards [001] are often observed (unlike the diagonals which form an angle of 54.5° with the $[1\bar{1}0]$). This direction has previously been identified as perpendicular to the miscut direction of the crystal. A summary of the step statistics is shown in Fig. 7.13.

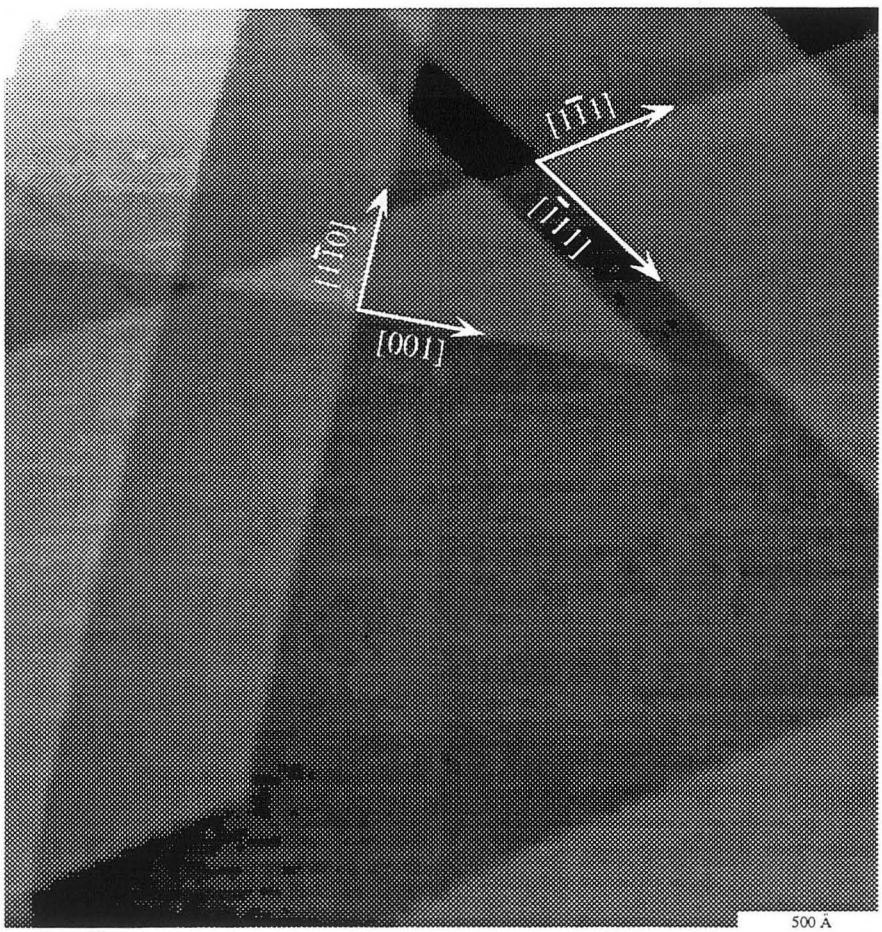

Figure 7.12 Step directions - Ni(110)

A typical large scale image (3140 Å x 3340 Å) used for extracting step statistics. The important step directions are labeled. These are identified by subsequent smaller scale images with atomic resolution. The surface was prepared by exposure to 20 L H2S and then annealing at high temperature (800 C) so this corresponds to the sulfur saturated condition for the step statistics data in Fig. 7.13.

For the clean crystal, the majority of steps are along the miscut direction, while with increasing amounts of S, the steps along the miscut direction disappear and are replaced by steps along the [001], [$\bar{1}$10] and diagonal directions. These changes can be used to quantitatively explain the effects of very small amounts of S on CO diffusion on

the Ni(110) surface as reported by Xiao, et al [13]. These results imply that chemisorption of a species even in small amounts can have a large effect on the substrate by influencing step structure. However, sulfur was not observed attached to the step edges for the sulfur contaminated structure due to an inability to obtain atomically resolved images at the step edges.

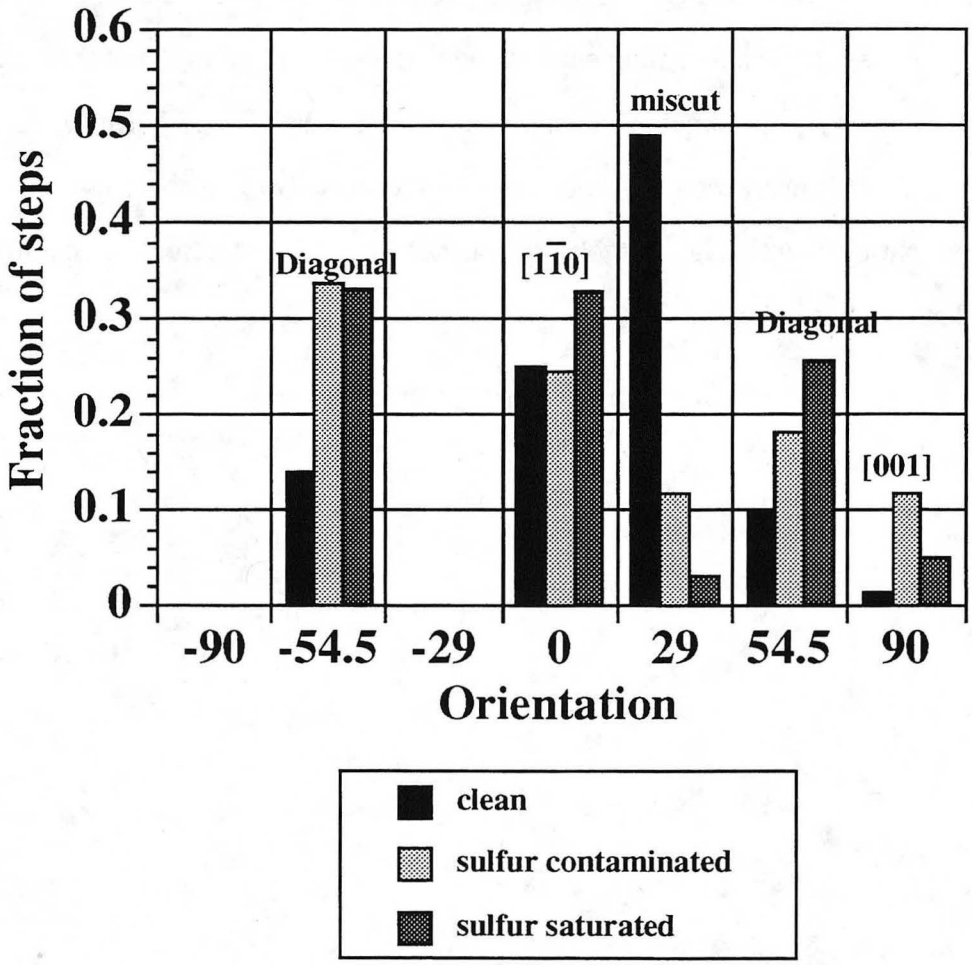

Figure 7.13 Step statistics

The fraction of steps observed at the various directions are plotted for three different surface preparations. The clean surface has a predominance of steps along the angle caused by the miscut of the crystal while with sulfur present these steps are removed and replaced by steps along the $[\bar{1}11]$, [001], and diagonal ($[1\bar{1}1]$ and $[\bar{1}11]$)directions.

7.4 Oxygen on Ni(110)

As was mentioned previously, mixed structures of the Ni(110)-p(2x1)O and $p(3x1)O_f$ structures are observed with the structural models for the p(2x1) depicted in Fig. 7.1 and the $p(3x1)_f$ in Fig. 7.7. An image is shown in Fig. 7.14 and as might be expected the surface consists of wide and narrow rows along the [001] direction due to the double and single added O-Ni-O rows respectively. However, a cursor drawn across the image shows that the tunneling current due to the two structures is not the same with the single row having a smaller corrugation and a lower average current. Although possibly due to the interaction of a blunt tip simultaneously with the two rows, it has been observed that different images are observed for densely packed adsorbates compared to isolated adsorbates [14-16].

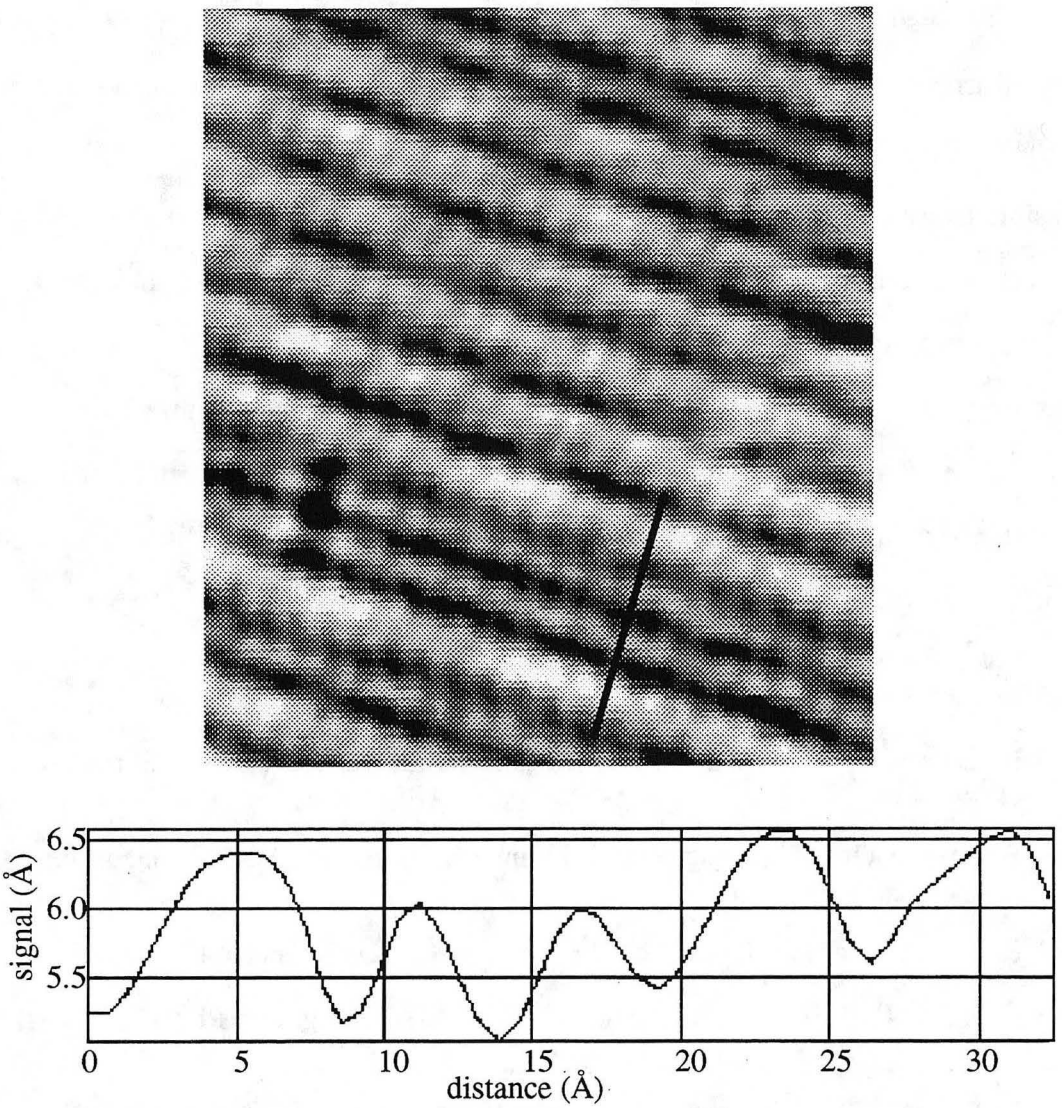

Figure 7.14 Mixture of oxygen structures

In the 70 Å x 80 Å image, the single and double added rows are imaged as narrow and wide bands. The cursor plot shows that the single rows have a deeper minima between them and have lower maxima as well, giving rise to a lower average current for the p(2x1) structure compared to the p(3x1) structure. (I = 1.7 nA, Bias = -44.8 mV)

7.5 Summary and conclusions

For a surface where oxygen is added to a previously S contaminated surface, an ordered array of elongated islands in the $[1\bar{1}0]$ direction is formed. The islands consist of the Ni(110)-p(2x1)O structure and are separated by troughs of Ni(110)-c(2x2)S. Possible causes for the structure include sulfur inhibited diffusion, an anisotropic S-S interaction and the effects of strain in the substrate due to the chemisorption. Despite the fact that the surface has been thoroughly investigated, a previously unreported structure consisting of S and O has also been observed on this surface for high exposures of oxygen. In spite of the complexities that are revealed in the coadsorption results, the coexistence of well ordered domains of structures with small unit cells will provide an important test of STM theory.

Chapter 7 References

[1] L. Eierdal, F. Besenbacher, E. Lægsgaard and I. Stensgaard, Surf. Sci. **312,** (1994) 31.

[2] F. Besenbacher, I. Stensgaard, L. Ruan, J.K. Nørskov and K.W. Jacobsen, Surf. Sci. **272,** (1992) 334.

[3] F. Besenbacher and J. Nørskov, Progress in Surface Science **44,** (1993) 5.

[4] L. Ruan, F. Besenbacher, I. Stensgaard and E. Lægsgaard, Phys. Rev. Lett. **69,** 24 (1992) 3523.

[5] L. Ruan, F. Besenbacher, I. Stensgaard and E. Lægsgaard, Phys. Rev. Lett. **70,** 26 (1993) 4079.

[6] H. Bu, C.D. Roux and J.W. Rabalais, Journal of Chemical Physics **97,** 2 (1992) 1465.

[7] C.D. Roux, H. Bu and J.W. Rabalais, Chem. Phys. Lett. **200,** 1,2 (1992) 60.

[8] K. Kern, H. Niehus, A. Schatz, P. Zeppenfeld, J. Goerge and G. Comsa, Phys. Rev. Lett. **67,** 7 (1991) 855.

[9] P. Sprunger, F. Besenbacher, I. Stensgaard and E. Lægsgaard, Surf. Sci. **320,** (1994) 271.

[10] J.L. Brand, A.A. Deckert and S.M. George, Surf. Sci. **194,** (1988) 457.

[11] S. Esch, M. Hohage, T. Michely and G. Comsa, Phys. Rev. Lett. **72,** (1994) 518.

[12] X.-D. Xiao, Y. Xie and Y.R. Shen, Surf. Sci. **271,** (1992) 295.

[13] H.C. Galloway, P. Sautet and M. Salmeron, in preparation (1995)

[14] P. Sautet, J.C. Dunphy, D.F. Ogletree, C. Joachim, and M. Salmeron, Surf. Sci. **315,** 1-2 (1994) 127.

[15] P. Sautet, J. Dunphy, D.F. Ogletree and M. Salmeron, Surf. Sci. **295,** (1993) 347.

[16] J.C. Dunphy, P. Sautet, D.F. Ogletree and M.B. Salmeron, J. Vac. Sci. Technol. A **11,** 4 (1993) 1975.

Chapter 8 Conclusions

8.1 Metal oxide overlayers

Results from studies of two systems of metal oxide overlayers have been presented. Both are transition metal oxides on the Pt(111) surface which exhibit a variety of surface structures and stoichiometries. For iron oxide on Pt(111), the first monolayer forms a stable structure with a stoichiometry of Fe:O = 1:1 in a wide range of oxygen pressures. From the STM images the structure is identified as a bilayer of Fe and O with the same structure as an FeO(111) surface. The 10% lattice mismatch between the substrate and overlayer leads to a large unit cell which is imaged as a Moiré pattern (modulation of the atomic corrugation) by STM. The symmetry of the large unit cell indicates that the FeO atomic directions are rotated by 0.6° with respect to the Pt close-packed directions and the lattice constant in the plane of the surface is expanded 3.09 ± 0.02 Å compared to the bulk value of 3.04 Å. From XPD experiments, the Fe-O bond distance is determined to be 1.90 Å strongly contracted from the bulk value of 2.15 Å and the surface is shown to be oxygen terminated.

For O_2 pressures of 10^{-5} torr, a multilayer iron oxide is observed that has a 2x2 periodicity with respect to the FeO monolayer, indicative of the $Fe_3O_4(111)$ surface. The structure contains a large number of atomic scale defects and forms terraces separated by multiple height steps. For O_2 pressures of 10^{-4} torr, a $\sqrt{3}x\sqrt{3}R30°$ structure is formed which can coexist with the FeO monolayer. The $\sqrt{3}x\sqrt{3}R30°$ symmetry with respect to the FeO layer is a clear indication of its corresponding to an α-$Fe_2O_3(0001)$ surface. Initial growth is two dimensional over the FeO monolayer. When the two dimensional islands are large enough (~100 Å) a Moiré structure with a periodicity of 43 Å is observed. This can be explained by the lattice mismatch between two oxide layers due to the growth of an α-$Fe_2O_3(0001)$ layer (2.90 Å bulk unit cell) on top of the FeO

monolayer (3.09 Å unit cell). In addition, at higher coverages multiple height crystallites with an as yet undetermined structure are also formed.

In the titanium oxide system, the first ordered structure is formed by oxidizing and then annealing in vacuum to produce a reduced form of the oxide. The unit cell is consistent with $Ti_2O_3(0001)$ and also shows a three fold symmetric Moiré pattern. For films formed at higher oxygen pressures, a complex structure with a lower symmetry Moiré pattern is observed corresponding to the $TiO_2(111)$ surface. The Moiré pattern consists of rows in one direction with a periodicity of ~5 Å in one direction and a periodicity of ~15-25 Å in the second direction. The unit cell is not as well defined as in other structures. In the submonolayer growth regime, the titania islands have a two level structure that suggests two different forms of oxide.

The common property of both oxides studied is that the strength of the metal oxygen bonds is larger than that of the bonds with the Pt substrate leading to the formation of crystalline films with their own lattice constant, close to that of bulk oxides and independent of the Pt substrate. The lattice mismatch resulting from the overlay of the oxide structure on the Pt leads to the formation of the beautiful Moiré structures. The second common characteristic is the formation of a reduced first layer at the interface with the Pt(111) surface. This stable, but reduced, form of each of the two oxides forms a continuous layer due to the strong metal-metal interaction. Slightly thicker layers reflect more strongly the bulk equilibrium thermodynamics with higher oxygen pressures leading to higher oxidation states, which is not necessarily the case for the single crystal oxide surfaces.

8.2 ESQC calculations for the FeO/Pt(111) system

While STM is not yet a routine quantitative surface structural measurement technique, many structural details of the structures can be deduced directly from the symmetry of the images. This is especially helpful for the case of oxide overlayers where

the lattice mismatch leads to large unit cells that can have very complicated diffraction patterns. However, it is desirable to develop a more precise understanding of the tunneling process on metal oxide surfaces. Toward this goal, ESQC calculations on the FeO/Pt(111) system have been conducted. To our knowledge, this is the first calculation of STM results for a metal oxide at the atomic scale as well as the first attempt to model a Moiré pattern in STM imaging.

With regards to the oxide tunneling, the O atoms and more specifically, the O pz orbitals are the dominant contribution to the tunneling current since they overlap most efficiently with the orbitals of the tip atoms. For the Moiré pattern, it is found that the topography observed by STM does not have a simple correspondence with the topography of the surface and varies with tip termination and gap conditions. However, the magnitude of the atomic corrugation does have a simple correspondence with topography, becoming larger as the tip-surface separation is decreasing. This suggests that current mode or constant height imaging will provide a better method of identifying the relationship of the STM image to the relative surface buckling.

More subtle electronic effects that differ as a function of adsorption site across the surface can also be accounted for by the theory. These include the difference between the fcc and hcp sites which is due to a direct interaction between the oxygen and first layer Pt atoms. The reduced current at the top site compared to the hollows is from enhanced Fe-A1 symmetry (s, p_z, and d_{z^2} orbitals) and O-A1 symmetry (s and p_z) contributions. These are the orbitals perpendicular to the surface and along the Fe-Pt bond for the top site, as would be expected from the geometry of the Fe-Pt interaction. As these orbitals interfere destructively and only the O contribution is corrugated, the enhancement is seen as an increase in the corrugation but the total current is decreased due to a more efficient destructive interference.

8.3 Oxygen and sulfur on Ni(110)

Oxygen and sulfur coadsorbed on Ni(110) above room temperature form an ordered array of islands and troughs where the islands consist of the Ni(110)-p(2x1)O structure and the troughs are covered by the Ni(110)-c(2x2)S structure. The islands are elongated in the $[1\bar{1}0]$ direction and are of the order of 100-200 Å in the [001] direction. The edges of the islands are not along the $[1\bar{1}0]$ direction but along the $[2\bar{2}1]$ and $[2\bar{2}\bar{1}]$ directions. Possible causes of this structure are substrate mediated long range forces due to the strain induced by the adsorbates and the role of sulfur in inhibiting diffusion of Ni atoms which is necessary for the formation of the added row oxygen structures.

8.4 Summary

While the complexity of metal oxide overlayers will continue to make research in this area quite challenging, these studies have revealed that at least some of the observed experimental results can be understood in terms of simple physical ideas. The first monolayer shows an enhanced stability and forms as a reduced layer of the oxide while the stoichiometry of thicker films can be influenced by changing the growth conditions. The experimental advantages of these systems such as the elimination of charging effects are already well known. In addition, the known structure of the substrate can provide a reference for identifying surface structures by the use of symmetry. Finally, the case of FeO/Pt(111) shows that with considerable effort, a quantitative structural analysis of a complicated metal oxide overlayer is possible and that STM calculations can provide a detailed understanding of the correspondence of STM images to the atomic structure.

Appendix I - Materials and Procedures

Materials list

Some of the specialized materials used in constructing a UHV STM are listed along with supplier information

Table AI.1 List of materials and suppliers

Description	Product name	Company
epoxy	Epotek H61	Epoxy Technology, Inc. Billerica, MA
conducting epoxy	Epotek H31	Epoxy Technology, Inc. Billerica, MA
piezoceramics	EBL PZT 3 (Lead Zirconate Titanate)	Stavely Sensors EBL Product Line East Hartford, CT
wire	Kapton coated copper wire, 0.001", 0.003", 0.007"	California Fine Wire Grover City, CA
optical table legs	air damped	Newport Fountain Valley, CA
"viton"	Compound S455-70 (actually a silicone compound that is more UHV compatible than viton)	Parker O-rings Bay Seal Co. Hayward, CA
sapphire balls	1/8" diameter	Swiss Jewel Co.
syringe needle	No. 23 standard (.012" ID)	Becton-Dickinson Rutherford, NJ
piezo coating (for etching)	MicroProducts Shield Stop-off Lacquer	Tolber Division Pyramid Plastics, Inc. Hope, AK
silver solder and flux	EutecRod 157 Eutector Flux 157	Eutectic Co. Flushing, NY

Tip etching procedure

The tip is electrochemically etched in a solution of molten salt. The mixture is 4:1 $NaNO_3$:NaCl which melts at approximately 300 C. The tip is biased 2.5 V DC with respect to a counter electrode in the solution (stainless steel or another Pt/Rh wire). The heat source must be powerful enough that the tip does not cause the salt mixture to recrystallize, and some preheating of the tip by putting it close to the solution usually helps prevent recrystallization as well. A wire diameter of .010" makes it faster to etch the tip to a sharp point and is a smaller thermal mass so less heat is required. The tip is mounted to a micrometer so that it can be moved up and down ~ 1 mm while etching. When the salt solution becomes too contaminated as evidenced by a high density of black particles floating around, it will cease to etch effectively. Precutting the wire to a rough point can also facilitate the process. In spite of the simplicity of the procedure some tips etch much more readily than others. Often the wire is pulled from a thicker diameter so it is possible that grain orientation is affecting the process.

Piezo etching procedure

The piezoceramics are bought from the manufacturer with a Ni coating to use as an electrode for applying fields. For the cylinders, the electrode must be sectored on the outside to provide x and y motions. Since solder is used to attach the piezos, a ring on the edge of the piezos must also be separated by removing a thin line of the metallic coating. The manufacturer will sector piezos but custom designs add to the cost considerably. It is possible to simply remove the coating by scratching using a lathe to guide the tool. This has the advantage of providing a highly aligned method of sectoring. However, it mechanically weakens the piezo. Another method is to remove sections of the electrode with an etching procedure.

First the entire piezo is coated with MicroProducts Shield Stop-off Lacquer (see above). This has to harden for an hour, and then sections of the coating are removed

where the electrode is to be etched. This can be done gently with an Exacto knife and does not provide as much mechanical stress as using the lathe. Then the coating is allowed to further harden for several hours. The piezo is then dipped into a mixture of equal amounts of H_2O, H_2SO4, and H_3NO_3. Strong solutions of the acids are used but the exact proportions are not critical. The etch mixture should be at room temperature or the etch is too violent and some electrode will be removed even underneath the coating. Mixing the solution will produce heat so it should be premixed and allowed to cool. The acids should be added to the water. The electrode will darken and then dissolve into the solution leaving the white of the piezoceramic visible. The piezo is then dipped briefly into water to stop the etching and then the coating is removed using acetone. While it is difficult to produce perfectly straight lines, the tolerances of the piezos are large to begin with so this is probably only a small effect. It is also possible to produce thinner lines between sectors than using the mechanical scratching method.

Appendix II - Piezo Testing

Resonance frequencies

A very simple method of determining the resonance frequencies of the microscope was first described by Stemmer and Engel [1]. This method does not require any special sample or connections and uses a typical laboratory oscillator and lock-in amplifier. The method consists of measuring the response in y to excitation in the x direction. A sinusoidal wave of ~1 V is applied to the x+ and x- sectors of a piezo and the signal between one y electrode and the inner electrode is measured while the other y electrode is grounded. (as depicted in the figure below) The frequency of the excitation applied to x is varied and the amplitude and phase of the y response are recorded.

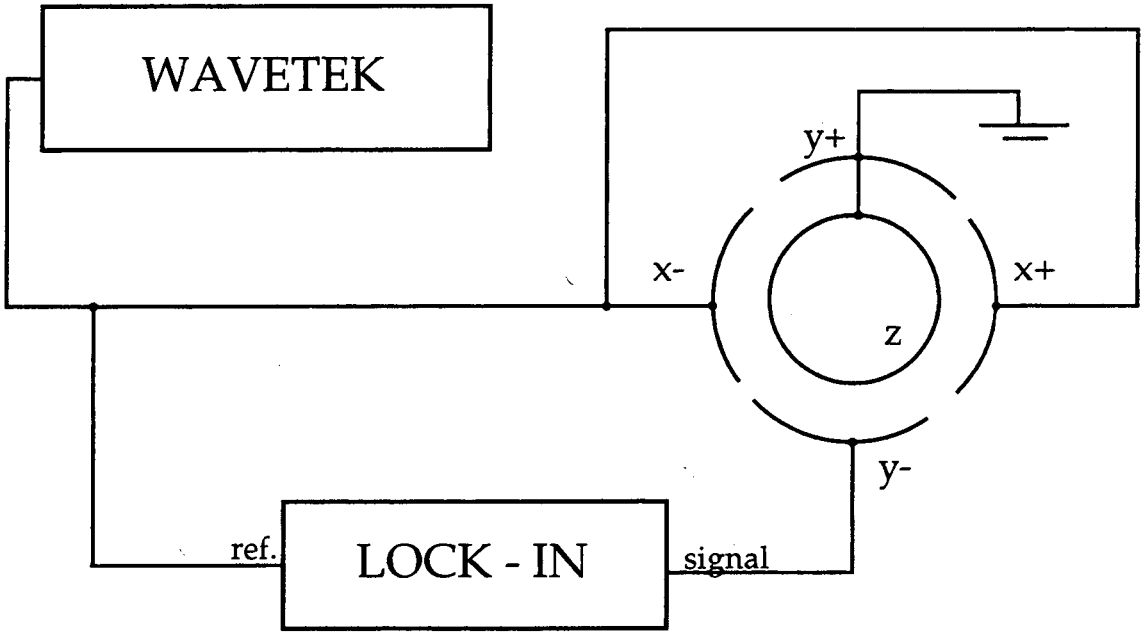

Figure AII.1 Schematic of piezo resonance testing electronics
The connections are shown for recording the y- output response.

A typical plot for a microscope of this design is shown below. The data is for an outer piezo and two pairs of resonance peaks are seen at 1.6 and 1.9 kHz and at 4.1 and 4.3 kHz. Each pair is two almost degenerate modes. Large phase changes are also recorded at these frequencies.

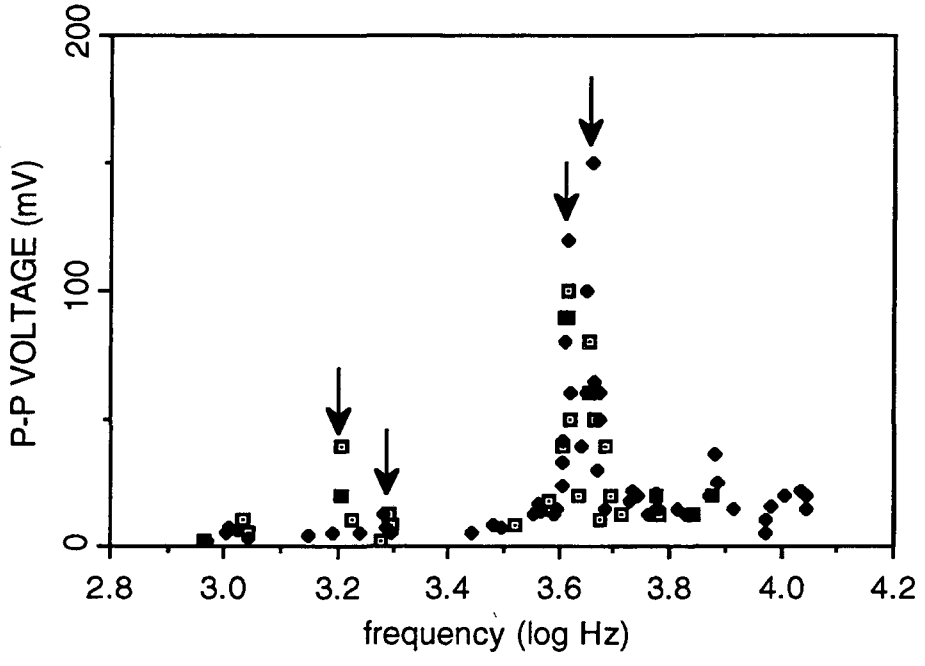

Figure AII.2 Piezo resonance testing output

The arrows mark four resonance peaks at 1.6,1.9, 4.1, and 4.3 kHz. The two sets of symbols are for the y- and y+ output response.

An even lower resonance pair is seen around 450-700 Hz when the sample is sitting on the microscope. However, this frequency is not observed in the tunneling current. The resonance frequencies seen by this method correlate very well with those seen in the tunneling current. Improvements in the rigidity of the microscope can also be measured by whether or not the frequency is shifted upwards. While it is not clear how

to turn this measurement into an expected noise criteria it can aid in improving construction techniques. This measurement indicated that to change the inner piezo from a 0.5" diameter tube to a 0.125" diameter tube would improve the performance because it increases the resonance frequency of the scanning tube and thus reduces noise as well as allowing for faster scanning. The scan speed is limited to a frequency lower than the lowest resonance frequency. It is also imperative that the voltages applied to the piezos be completely free of noise with a frequency close to the resonance frequency. Improvement has been seen by simply filtering the x, y, and z offset voltages with a low pass filter with a cut off of only a few Hz when they are not being used for approaching and a large time constant is acceptable.

Piezo capacitance measurement

The piezos have an easily measurable capacitance and this can be used to check the connections from outside the vacuum chamber. The capacitance from one outside sector to another is ~1.6 nF for the outer piezo (.5" L x 0.875" OD x 0.020" W) and ~0.5 nF for the inner piezo (5" L x 0.125" OD x 0.010" W). The wires alone would have a capacitance of a few pF easily distinguishable from the situation where the wires are connected to the piezos.

Appendix II References

[1] A. Stemmer and A. Engel, Ultramicroscopy **34,** 3 (1990) 129.

LAWRENCE BERKELEY LABORATORY
CENTER FOR ADVANCED MATERIALS
1 CYCLOTRON ROAD
BERKELEY, CALIFORNIA 94720